STUDIES ON SOME LAYER STRUCTURED SUPERCONDUCTORS: $Bi_4O_4S_3$, Bi-2212 AND MgB_2

A thesis submitted for the degree of

DOCTOR OF PHILOSOPHY

in

PHYSICS

by

MANCHINEELLU PADMAVATHI

SCHOOL OF PHYSICS
UNIVERSITY OF HYDERABAD
HYDERABAD-500046
INDIA

MARCH 2016

DECLARATION

I, ***Mrs. Manchineellu Padmavathi***, hereby declare that the thesis entitled "**Studies on Some Layer Structured Superconductors: $Bi_4O_4S_3$, Bi-2212 and MgB_2**" submitted by me under the guidance and supervision of **Prof. Rajender Singh** is a bonafide research work which is also free from plagiarism. I also declare that it has not been submitted previously in part or in full to this University or any other University or Institution for the award of any degree or diploma. I hereby agree that my thesis can be deposited in Shodganga/INFLIBNET.

A report on plagiarism statistics from the University Librarian is enclosed.

Date:

Manchineellu Padmavathi

(Reg. No. 10PHPH19)

Signature of the Supervisor

CERTIFICATE

This is to certify that the research work complied and presented in the thesis entitled "**Studies on Some Layer Structured Superconductors: $Bi_4O_4S_3$, Bi-2212 and MgB_2**" is an original work has been carried out by ***Mrs. Manchineellu Padmavathi*** at the School of Physics, University of Hyderabad**,** Hyderabad under my supervision. The thesis submitted by ***Mrs. Manchineellu Padmavathi*** for the degree of **DOCTORATE OF PHILOSOPHY** in the School of Physics has not been submitted to any other university partially or fully for the award of any degree.

Prof. Rajender Singh
(Supervisor)

Dean
School of Physics
Date:

Acknowledgements

It gives me immense pleasure and delight to express my deep sense of gratitude and indebtedness to my research guide ***Prof. Rajender Singh***, School of Physics, University of Hyderabad, for his support and inspiring guidance. His dedication to science and integrity have inspired me to reach this stage. I am grateful to him for teaching me how to think innovatively in setting up the experiments. His guidance went beyond science and helped me to grow as a strong individual.

I express my gratitude and profound thanks to Prof. R. Singh, Dean, School of Physics, and previous Deans, *Prof. C. Bansal, Prof. S. P. Tiwari* and *Prof. S. Chaturvedi*, for the provided academic facilities.

My sincere thanks to the doctoral committee members *Prof. C. S. Sunandana, Prof. Ghana shyam Krishna Dr. P. K. Suresh*, and *Dr. S. V. S. Nageswara rao* for their valuable suggestions and for evaluating my work at each stage.

I am very much thankful to coordinator Center for Nano technology (CNF) and Dean, School of engineering science and Technology (SEST) for providing XRD, TEM and PPMS facilities.

I am thankful to *Prof. V. Seshubai and Prof. James Raju* for allowing me to use Vacuum system and Microwave oven facilities in their labs.

I thank *Prof. A. P. Patak, Prof. Siva Kumar, Prof. D. Narayana Rao and Dr. Soma sanyal* for their support during PhD course work.

I convey my heartful thanks to *Mr. Mantu Kumar, Mr. Ramana, Mr. Laxmi Narayana, Mr. Durga Prasad, Mr. Pankaj, Mr. Mallesh, Mr. Ravi Shankar, Mr. Mukunda Reddy, Mr. Rajesh, Mis. Sunitha, Mrs. Arundathi Mrs. Deepthi* for their support in doing various measurements during my PhD. And iam very much thankful to Mr. Abraham, and Mrs. Sailaja for their moral support.

I am very much thankful to my labmates, *Dr. Joji Kurian, Dr. P. Sandhya Rani, Dr. D. Vijayan, Dr. M. Venkaiah, Dr. S. Sai Priya, Mr. G.Thirupathi, Mr. A. Ramesh, Mrs. Jasmeeth Kaur Gandhi, Mr. K. Ravibabu, Ms. Atiya Farheen, Ms. Nisha Gautham.*

I just fail to be a gladdened heart and remain uncomfortable with myself at this pleasantest hour of another turn in my life, though with this modest achievement of mine, if I withhold recording the names of my life time friends *Ms. K. N. Deepthi, Mrs. M. Vi,jaya Lakshmi* who, we take pride in one another's achievements. And my good friends *Mrs. M. Archana, Mrs. Ambika, Mrs. N. Sravani, Ms. B. Geetha, Ms. K. Sridevi, Mrs. Vijaya Sri, Ms. Roja Lakshmi,* and *Ms. Sandra Dias* for their moral support during my stay.

I thank all my co-scholars *Mr. Ravi Kumar, Mr.Raju Botta, Mr. Pavan Naik, Mr. Uma Shankar (late), Mr. Pavan Venu Prakash, Mr. Suman Kalyan, Mr. C. Bheem Lingam, Mr. Devaraju, Mr. P. D. Shankar Dr. Sri Ramulu, Dr. Swaroop Raju, Dr. Ramudu, Dr. Devendra, Mr. I. V. Shankar Mr. Sanjeev, Mr. A. Iyyappan, Mr. S.V. Nagi reddy, Mr. Bashayya, Mr. Senthil Kumar, Mr. Lakshun Naidu, Mr. Anil Kumar, Mr. Ravikanth, Mr. Andrews Joseph, Mr. Vinay, Mr. Joshi, and Mr. K. Phaneendra (IUAC, Delhi).*

All these loving souls credited to my account apart, what I am today is nothing but dream of my parents, *Mr. & Mrs. M. Subbarayudu and M. Veeramma,* who have always wanted to see me growing towards success. I would like to thank, my sister *Mrs. S. Subadra,* my Brothers *Mr. M. Vekata Ramana, Mr. M. Naga Raju* and *Mr. M. Srinivasulu,* my sister-in laws *Mrs. M. Sujatha* and *Mrs. M. Laxmi Devi*, my parent-in-laws *Mr.& Mrs. P. Chalapathi & Bhagyamma,* and my son-in-laws *Mr. M. V. S. Ramu* and *Mr. M. Mahesh* for their motivation, support and love.

Finally I thank my soul-mate and my strength, my husband, Dr. P. Kishore for being with me in each and every moment.

I gratefully acknowledge everyone who have invariably contributed for my success.

Manchineellu Padmavathi

Dedicated to

My Lovely Family

Abstract

The studies on layered superconducting materials are important in understanding the basic phenomena of superconductivity and their subsequent applications. The recent trend in order to improve the physical and magnetic properties of superconductors is the preparation of composite and hetero structures of superconductors. The thesis includes the effect of composition and doping in layered $Bi_4O_4S_3$ superconductor, studies on composite superconducting system and Hetero structure of Bi-2212 and MgB_2 layered high T_c superconductors.

We have prepared $Bi_4O_4S_3$ superconductor with 5% and 10% of excess Bi_2O_3, and 10% of excess Bi, Sulfur. Excess Bi_2O_3 acted as flux for the phase formation, whereas excess Bi and sulfur causes suppression of the superconducting phase. $Bi_4O_4S_3$ synthesized with 5% of excess Bi_2O_3 ensured highest grain size, critical current density and pinning force among the synthesized samples. J_c varies according to collective pinning model. The dominating pinning mechanism changes from surface to point pinning with increase in Bi_2O_3. The studies on the effect of Ca doping at Bi site in $Bi_4O_4S_3$ were carried out. $Bi_{4-x}Ca_xO_4S_3$ sample with x=0.25 exhibits increase in T_c, J_c, and F_p values. With Ca doping in the range $1>x>0.25$, deterioration of superconducting phase with increase in Ca doping is observed.

The composite system of Bi-2212 glass ceramic and MgB2 superconductor were prepared with Bi-2212 as matrix and MgB_2 as reinforcing material (2:1), and with Bi-2212 as reinforcing material and MgB_2 as matrix (1:2). Composite samples show increase in critical current density. Nano particles of reinforcing superconducting material in the matrix superconductor act as flux pinning centers causing enhancement in J_c in the composite samples. Pinning mechanism in composite samples is same as in the matrix phase of the composites.

Hetero structures of Bi-2212 and MgB_2 superconductors were prepared in the form of bulk multilayers. Bi-2212 and MgB_2 were arranged in the form of bi-layer and tri-layers. Critical current density is enhanced in the hetero samples due to increase in the superconducting volume fraction. Tri-layer sample showed highest J_c and inverted J_c anisotropy due to enhancement in the ab-plane properties. Fast decay in J_c at high fields in these samples is observed due to different Pinning mechanism and micro structural variations.

Contents

CHAPTER 1

Introduction

1.1 Superconductivity

One of the most historical achievements of condensed matter physics is the liquefaction of Helium gas in 1908 by H. K. Onnes [1]. This lead to step into a new history in the solid state physics. In general, the resistance of a metal decreases with decrease in temperature. With this idea H. K. Onnes tried to check the lowest point of the resistance of metal at low temperature. He succeeded by observing zero resistance in Hg at 4.2K. This resistanceless state of metal is named as "supraconductivity" by H. K. Onnes in 1911 [2]. Later, it became popular with the name "superconductivity". The materials which can show resistanceless current flow below a particular temperature are called superconductors. The most interesting and important property of superconductors is its behaviour in magnetic field. In 1933, W. Meissner observed the expulsion of magnetic field by superconducting materials [3]. When magnetic field is applied on superconductors, field will induce surface currents in superconductors. The field generated due to these surface currents will be equal in quantity and opposite in direction of the applied field so that this induced field completely repels the applied field. Thus, superconducting material shows perfect diamagnetism in the applied magnetic field. This diamagnetic effect with applied field on superconductors is called Meissner effect. The critical parameters of superconductors are defined as the transition temperature (T_c) – the temperature where resistance becomes zero, critical filed (H_c) - the field below which superconductor shows diamagnetic effect and the critical current density (J_c) - maximum induced screening currents flowing without any resistance in the superconductor. Superconductors depend on internal parameters like penetration depth-defined as the maximum length till the applied field can penetrate through surface of the superconductor, coherence length-defined as the maximum length till the coherent cooper pair wave can exist and external parameters like temperature, pressure, and magnetic field [4].

1.2 Types of Superconductors

According to their magnetic properties, superconductors are divided into type-I superconductors and type-II superconductors. Type-I superconductors include all superconducting elements except niobium. Niobium, superconducting alloys and chemical compounds make up the second group, type-II superconductors. The so-called high-T_c superconductors also belong to this group. The chief difference between the two groups lies in their different response to an external magnetic field.

1.2.1 Type I Superconductor

Let us consider that the magnetization curve of a superconductor specimen, here it is a long cylinder in a longitudinal external magnetic field H_0. As the field H_O increases, the induction inside the specimen does not change at first; it remains B=0. As soon as H_0 reaches the value of H_{cm}, the superconductivity is destroyed, the field penetrates into the superconductor, and $B=H_0$. Therefore, the magnetization curve $B=B(H_0)$ appears as shown in figure 1(a). The magnetic induction *B* and the magnetic field *Ho* are related to each other by the well-known expression $B=H_0 + 4\pi M$, where *M* is the magnetic moment per unit volume. The magnetization curve is often plotted as $-4\pi M$ versus H_0, as illustrated in figure 1(b).

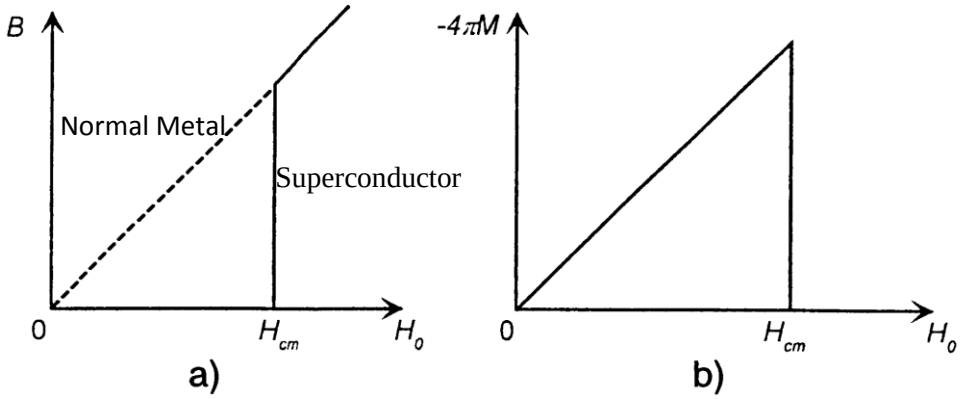

Figure 1.1 *(a) Magnetization curve of a Superconductor (b) magnetic moment per unit volume, M, versus H_0*

The long cylinder superconductor is placed in a uniform magnetic field parallel to its surface, the superconductivity is destroyed when the field reaches to the critical value H_{cm}. It is much harder to destroy the superconductivity of the same cylinder if it is placed in a transverse magnetic field. The same is true for other shapes like an ellipsoid, a sphere, or other bodies of more complicated geometries [5].

1.2.2 Type II Superconductor

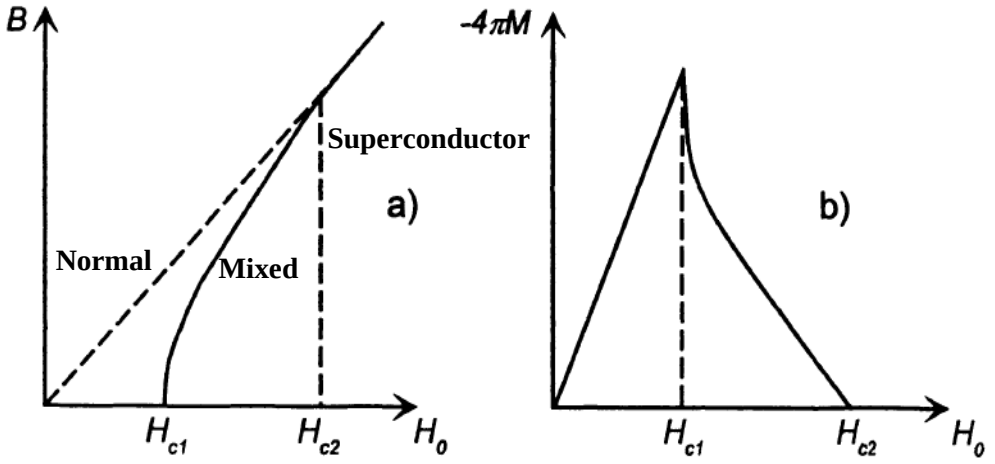

Figure 1.2 *(a) Magnetization curves of a type-II superconductor: (a) magnetic induction B as a function of an external field H_o; (b) magnetic moment per unit volume, M, as a function of H_o.*

The magnetic field penetrates into type-II materials is in a quite extraordinary way. Suppose type-II superconductor of a long cylinder shape placed in a longitudinal magnetic field. The field is increased from zero, at first the cylinder pushes all the field out, that is the magnetic induction in the interior of the cylinder is zero. It means that initially observe the Meissner effect. As long as the external field is $H_0<H_{c1}$, the average field in the interior of the specimen is B=O. However, beginning from a certain value of the field it start to register a finite induction in the cylinder, this field is called the lower critical field and denoted by H_{c1} [5]. Thus, at $H_{c1}<H_0<H_{c2}$ a steadily increasing field B penetrates the superconductor. This field always remains below the external field H_a and the specimen's superconductivity is not destroyed. For further increase of the external magnetic field H_0, the induction of magnetic field build up until the average field in the cylinder becomes equal to the external field H_0 and the cylinder goes to the normal state, it is happen at the so-called upper critical field H_{c2}. That is at a certain field $H_0=H_{c2}$ the average field in the interior B, becomes equal to H_a and the bulk superconductivity disappears Penetration of vortices into the interior of a superconductor becomes thermodynamically favourable at $H_0>H_{c1}$. A partial penetration of the magnetic field in the interior of the specimen is at fields from H_{c1} (the lower critical field) to H_{c2} (the upper critical field) is known as the mixed state.

In other words, Abrikosov and Zavaritzkii discussed the possibility, that the length difference could also become negative, if the coherence length (ξ) is smaller than the

magnetic penetration depth (λ_m). Based on the Ginsburg-Landau theory, Abrikosov calculated the critical magnetic field for the case, where the difference $\xi - \lambda_m$ is negative, and demonstrate, that only in this case can have the good agreement with Zavaritzkii's experimental data, obtained with particularly carefully prepared thin films. Hence, they were apparently dealing with an unknown, new kind of superconductor called as the "second group". Eventually, which are referred to as type-II superconductors (with $\xi - \lambda_m$ is negative), whereas the superconductors with positive wall energy are called type-I superconductors (with $\xi - \lambda_m$ is positive). In a magnetic field, they can assume a new state, in which the superconductor is intersected by a regular lattice consisting of individual "magnetic flux quanta". The famous Abrikosov flux-line lattice had been discovered. The state of the superconductor containing the flux-line lattice is referred to as the mixed state [6].

1.3 Material Introduction

In this thesis, we have worked mainly on three different layered superconductors and their composite and Hetero structures.

1. CuO based Bi-2212 layered superconductor
2. AlB_2 type MgB_2 layered superconductor and
3. BiS_2 based $Bi_4O_4S_3$ layered superconductor.

1.3.1 Cuprate Superconductors

The first High Temperature Superconductor (HTS) with CuO based layered superconductor was discovered by Bednorz and Müller in 1986 [7]. The high superconducting transition temperature, T_C=92K of CuO based HTS materials made easy of the employment of a more economical cryogen. Between 1987 and 2016, T_c was raised from 92K as discovered in $YBa_2Cu_3O_x$ (YBCO) [8] over 133K as demonstrated in $Hg_2Ba_2Ca_2Cu_3O_y$ [9]. In copper based HTS the common structural elements is copper-oxide planes, which acts as the superconducting layers, and insulating layers that can separate the copper-oxide planes. The microstructure of polycrystalline highly anisotropic ceramic HTS materials strongly influences the properties. HTS materials increase the possibility of preparing electrical devices with higher efficiency and higher power density with low losses. HTS also used to build novel devices, such as Superconducting Magnetic Energy Storage (SMES), magnetic bearings, fault current limiters and switches along with

environmental advantages like oil free transformers and devices with low magnetic field leakage [10]. Bi-2212 based bulk conductor is potentially low cost and thermally high stable but its application is limited due to the mechanical inflexibility [11-13]. HTS materials synthesis through glass precursors was introduced in 1988, and extensively studied by several groups [14-18]. Glass ceramic synthesis of HTS have great importance in view of practical applications, as glasses can be mould in desired shapes like wires/tapes, fibers, and films. Glass ceramic BSCCO superconductors preparation was studied with excessive copper compositions at different annealing temperatures and for different durations concluded that Bi-4334 composition is the optimum best composition to get single phase with T_c=85K and proper orientation [18]. The low J_c values for bulk CuO-based HTS materials is due to the Josephson weak link effects. In bulk sintered High T_c superconductors the grains are loosely connected with each other due to porosity. This point contacts act as weak links restricting the current carrying capacity. The exponential decay of J_c in CuO HTS materials with applied field is due to micro structural defects such as oxygen vacancies, twin-boundaries, and dislocations. At low fields J_c is governed by Josephson weak links whereas at high fields J_c is governed by grains [19].

1.3.2 Bi-2212 Superconductor

Among the layer structured high Transition temperature (T_c) superconductors $Bi_2Sr_2Ca_{n-1}Cu_nO_{6+\delta}$ composition gives three different phases based on the number of CuO layers. The T_c varies as 20K, 85K, and 110K with increase in n=1, 2 and 3 respectively [20, 21]. Bi-2212 phase formation through glass ceramic route especially with Bi-4334 composition leads to high dense and pore free high T_c superconductivity, thus enhancing the chances of practical applications of superconducting Bi-2212 [13]. The preparation of BSCCO ceramics through conventional solid-state method produces poorly sintered materials with low density [22, 23]. Whereas, the preparation of BSCCO via the glass ceramic route offers more advantages over solid state reaction route, such as possible improvement in gross homogeneity, reduced phase segregation, extended solid solubility, shorter process times, and the flexibility to be moulded into various shapes [23, 13]. The fabrication of glassy precursors can be done by oxide and carbonate calcined mixtures. Through melting and followed by quenching step, an amorphous solid can be homogenized on atomic scale [24, 25]. Bi-2201 is the first crystalline phase formed during the bulk crystallization of Bi-4334 glass. The transformation of Bi-2201 to Bi-2212 superconducting phase is a slow process accompanied by the uptake of Oxygen from the

atmosphere. The Bi-2212 phase transformation from Bi-2201 to Bi-2212 involves the diffusion of Ca, Cu and O ions such that the elongation of *c*-axis takes place by adding $CaCuO_2$ units into Bi-2201 structure. Hence, we can say that the Bi-2212 phase formation starts above 650^0C by a diffusion reaction between Bi-2201 phase and Ca, Cu, and O at the surface [18]. The composition in the Bi_2O_3-SrO-CaO-CuO system has a strong tendency to form a glass and the addition of Bi_2O_3 is particularly effective in facilitating glass formation. The ratio and co-existence of SrO and CaO is necessary for glass formation [26]. Figure 1.3 shows the general crystallographic structures of the three superconductive phases in the BSCCO system.

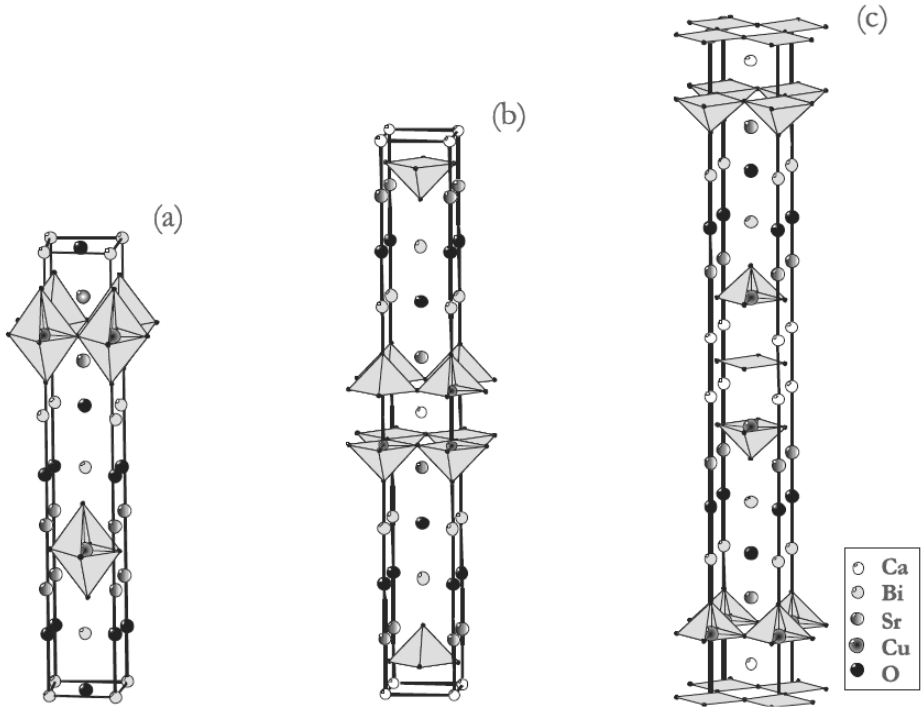

Figure 1.3 *Layer structure of BSCCO superconductors system.*

The compounds have layered structures parallel to the crystallographic a-b plane, consisting of rock-saltlike BiO bilayers that alternate with perovskite-like $[Sr_2Ca_{n-1}CunO_{1+2n}]$ units. The n=2 and n=3 members of the homologous series may be described as double BiO layers that alternate with $[Sr_2CaCu_2O_5]$ and $[Sr_2Ca_2Cu_3O_7]$ units respectively. The $[Sr_2Ca_{n-1}CunO_{1+2n}]$ units contain CuO_2 sheets, formed by corner-sharing $[CuO_4]$ units, which are oriented parallel to the *a-b* plane. The 2201 phase is characterized by one CuO_2 sheet (n=1), and the 2212 and 2223 phases by two and three CuO_2 sheets (n=2 and n=3) respectively. Thus, the general structure of all members of the series consists of CuO_2 sheets that are separated by calcium (for $n > 1$) and covered in the c direction by SrO

sheets. Due to the significantly different parameters of the *a*, *b* and *c* axis, the crystallization rate in the direction of the *a*-*b* plane is about 1000 times faster than in the c direction [27-36]. Thus, the crystals have a mica-like leafy shape, exhibiting a pronounced cleavability parallel to the *a*-*b* plane due to the weak bonding between the neighboring BiO layers. This structure also implies a pronounced anisotropy of the properties, causing the so-called "two dimensional superconductivity" parallel to the *a*-*b* plane. For example, the critical current density of the compounds is about 1000 times greater parallel to the *a*-*b* plane than parallel to the c axis. This phenomenon is due to the transportation of the super current by the Cu–O planes [37].

The *d.c.* electrical conductance of the Bi-4334 glasses is due to small polaron hopping mechanism [38]. By annealing these Glass samples at 820^0C for 24hrs showed insulator to metal transition at room temperature resistivity change from $7.3x10^8$ Ohm.cm to 0.4 Ohm.cm [13]. The maximum J_c observed in bulk Bi-2212 superconductor is 10^3 A/cm^{2}at 77K, and 0T, in case of Bi-2212 thick films it increases to 10^4A/cm^2, and in case of Bi-2212 thin films J_c enhanced to 10^5A/cm^2. The coherence length in Bi-2212 along *ab* axis is $42A^0$ and along *c* axis is $1A^0$. The penetration depth in Bi-2212 is $2000A^0$ and H_{irr} is 1T at 77K. These critical values resulted in finding the high anisotropy ratio of 150 to 900 in Bi-2212 superconductor [39]. The Pinning mechanism in BSCCO system is extensively studied by several groups [40-43]. In case of HTS superconductors the dominant microscopic pinning mechanism is determined in magnetic method. The method is involved in measuring the magnetization curves in the range of second anomalous peak, identified by the field B_{ss} which signifies the vortex solid-solid transition. B_{ss} is constant for BSCCO system, but in case of oxygen doped and irradiated BSCCO samples B_{ss} initially increases with temperature, suggesting a δl-pinning mechanism at low temperatures due to spatial fluctuations of the charge carrier mean free path [40]. In case of BSCCO samples synthesized with excess copper and calcium, resulted in high critical current density due to enhance in pinning effects resulting from the increased precipitation [41]. Pinning mechanism in Bi-2223 and pinning in Bi-2212 was dominated by mechanisms with vortex core pinning by normal, equi-axed defects. A conventional analysis of F_p, which tends to emphasis the lower temperature regime suggest pinning by point like defects, with dimensions $L<\xi$, such as oxygen vacancies, site and anti-sited effects, and interstitials. Analysis of the irreversibility line, which emphasizes the regime of higher temperatures, suggest pinning by larger defects with $L>\xi$, like precipitates [42].

Fast reduction of J_c in HTS at high field and close to the transition temperature is due to weak flux pinning strength and large thermal activated flux motion. Flux pinning strength and dimensionality of the material are very important to determine the flux pinning properties in HTS at high fields. In melt processed bulk Bi-2212 superconductor flux pinning is observed due to fine particles of Bi-free phases. Flux pinning strength of Bi-2212 is smaller compared to Y-123 due to worse flux pinning efficiency of larger non superconducting precipitates in smaller concentration. Normalized pinning force density of Bi-2212 superconductor followed scaling law of the form $F_p = AB_i^m(T)\, f(h)$ with reduced field. Here A is constant B_i is irreversible field h is reduced field. Temperature dependent parameter 'm' has obtained two values 1.15 and1.47 at lower and higher temperature regions suggesting that the dominant pinning centers are different in lower and higher temperature regions [43].

1.3.3 AlB2 type layered Superconductors

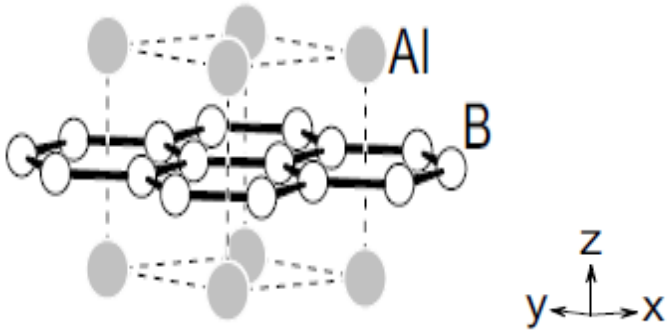

Figure 1.4 *Crystal structure of AlB_2*

From the simple aristotype AlB_2, nearly 46 structure types of binary and ternary intermetallic compounds were derived. AlB_2 corresponds to a simple hexagonal unit cell of aluminium atoms and two boron atoms occupying at trigonal prismatic sites in space group *P6/m2/m2/m* (No.191) as shown in figure 1.4. The boron atoms form a two dimensional infinite network, in which each boron atom has three other boron neighbours at a distance of 174pm. These graphite like layers (honey-comb) are well separated from each other by the lattice parameter *c*=326pm. For the binary compounds *RT2* and *RX2* and the ternary compounds *RTX*, *R2TX3*, and *R3T2X4* (*R*=alkaline earth, rare earth, or actinoid metal; *T*=transition metal; *X*=main group element) it is possible to get AlB_2 related structure, where *R* type element replace Al while *T* and *X* atoms form hexagon (boron position) [44]. Different borides with AlB_2structure were inter-compared in the ref. 45 [45].

By replacing Al with Mg, electron doping takes place due to change in valance states of $Mg^{+2}$and Al^{+3}. The stretched *c* lattice parameter affects the Boron plane. This turns the electro type (mainly π-band conduction) non-superconducting AlB_2 to hole type (mainly σ-band conduction) MgB_2 superconductor.

1.3.4 MgB2 Superconductor

MgB_2 is new generation high T_c superconductor with transition temperature of 39 K [46]. MgB_2 has significantly high T_c compared to the conventional LTS and high J_c compared to HTS. Magnesium di boride (MgB_2) is a binary inter metallic compound with a simple hexagonal crystal structure (AlB_2 type structure). MgB_2 structure composed of stacking of Mg and B layers as shown in figure 1.5. The boron atoms form graphite like honeycomb network and the Mg atoms are located at the cores of these hexagons. In the unit cell the atomic positions are (0, 0, 0) for Mg (Weizkoff symbol 1a) and (13, 23, 12) and (23, 13, 12) for B (Weizkoff symbol 2d) atoms [47, 48]. The coordination polyhedra are ($B_{12}Mg_8$) for Mg and (Mg_6B_3) for *B*. The lattice parameters are *a*=3.084Å and *c*=3.524Å. The inter-atomic distances are: B-B intra-layer 1.780Å, Mg-Mg intra-layer 3.084Å, Mg-Mg inter layer 3.524Å and Mg-B 2.5Å. The in-plane B-B distance is almost half that of the inter-plane B-B distance [48, 49].

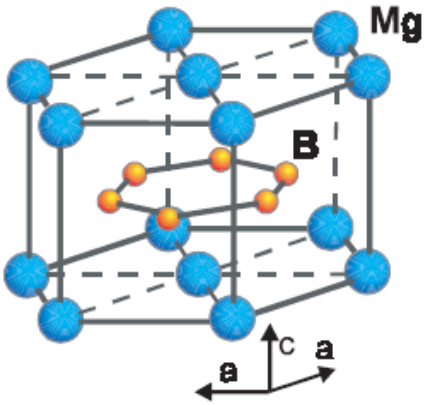

Figure 1.5 *Layer structure of MgB2.*

The MgB_2 is a brittle material just like the HTS materials. [50-52]. The low anisotropy (1.5-5) of MgB_2 compared to the highly anisotropic HTS means there is no need of texturing for making wires with high J_c [52-54]. The coherence length of MgB_2 is ξ~5-12 nm and the penetration depth is λ=100-140 nm with a GL factor of *K*~26 [53] at absolute zero temperature. Due to the large coherence length, higher than the inter-atomic spacing, the weak link problem is not severe in MgB_2. MgB_2 has two superconducting gaps in the

superconducting state, Δ_1~5-7meV and Δ_2 ~1.5-2.0meV [54, 55]. The normal state of MgB_2 is metallic and the normal state resistivity is much lower than that of other superconductors. For clean MgB_2 sample a very low normal state resistivity $\rho(T_c)$ of 0.4μΩcm and a high Residual Resistivity Ratio (RRR) of ~20 are observed [56].

The MgB_2 is a type II superconductor and is well within the clean limit of superconductivity. The depairing current density is J_c=10^7A/cm2 [57], one order of magnitude lower than that of the HTS materials. The observed transport critical current densities are of the order of 10^6A/cm2 at 4.2K in self-field, 3.8×10^4A/cm2 in 6T and 10^4A/cm^2 in 8T [58]. The transport J_c is of the order of 10^4A/cm^2 at 30K in 1T field [59]. The inter-granular J_c of MgB_2 is also high compared to HTS materials. Pure MgB_2 has very low critical field of $H_{c1}(0)$, which is less than 50mT [60, 61], upper critical field H_{c2} is between 15-20 T and irreversibility field in the range of 6-12T [56, 60, 62, 63] at 4.2K. Doped conductors have high H_{c2} and the maximum H_{c2} observed for SiC added MgB_2 wires is 33T [64]. Though MgB_2 has high self-field J_c at low temperatures, the rapid decay in J_c with field and temperature represents its poor vortex pinning, and low irreversibility field. Since MgB_2 has a rigid lattice with two simple elements in the structure. The lack of sufficient flux pinning at higher fields is due to the low density of defects produced during synthesis. MgB_2 has weak link free grain boundaries and the grain boundaries act as strong flux pinners. Only grain boundaries are effective pinning centers in pure MgB_2, thus MgB_2 samples with fine grains are needed for better properties. The irreversibility field of MgB_2 is only half of its upper critical field (H_{irr}=0.5×H_{c2}). The low irreversibility field and poor flux pinning cause rapid decrease in J_c at high fields. In order to compete with the Nb_3Sn for liquid helium temperature applications, the $J_c(H)$ of MgB_2 must be improved. This can be achieved by improving the flux pinning at high fields, increasing the H_{irr} and decreasing the electromagnetic anisotropy etc. [65–67].

The introduction of secondary phases or normal impurities to the superconducting matrix improves the flux pinning property of HTS materials [68]. Grain boundary pinning, like in Nb_3Sn is the dominating pinning mechanism in MgB_2 [69–72] and the pinning improves with reduced grain size [73]. It is found that in MgB_2 the aperiodic semi crystalline defects trapped in the crystalline phase act as intense vortex pinning centers and significantly enhance the high field performance of MgB_2 [74]. Inclusions and doping can improve the flux pinning of MgB_2 strongly. Doped MgB_2 wires have already reached H_{C2} values as high as 33 T, higher than that of Nb_3Sn and a record high value of 55T in coated

fibers. Primitive Powder-In-Tube conductors of MgB_2 could attain critical current densities nearly $10^6 A/cm^2$ in self-field at 4.2K. The high J_c values for wires or tapes with smaller grain size, full density, and perhaps with suitable additives can be in MgB_2 thin films [75].

Critical current density falls rapidly at high temperatures and magnetic fields due to weak flux pinning in this material. Pinning mechanism in pure and doped MgB_2 in various forms was extensively by several groups over last 15 years [76-81]. J_c in MgB_2 is mainly due to strongly connected unhindered grain boundaries. Intra grain current density in powder MgB_2 sample is higher than in bulk MgB_2 at low fields but at high field almost both equals. In both cases J_c decreases rapidly with applied field at high fields. The flux pinning force in powder MgB_2 and bulk MgB_2 first reported ref. 76 and 77. In Pure MgB_2 normalized pinning force density showed good scaling behaviour and showed h_{max} at 0.2 suggesting dominating pinning mechanism as surface pinning due to grain boundaries. In bulk MgB_2 bulk pinning due to grain boundaries is observed but in case of grinded powder MgB_2 sample bulk pinning is weak and surface barriers play important role in determining the first field of flux penetration as well as the irreversibility line. Flux penetration through the surface by creation of a critical nucleus consisting of one or several vortex loops. In powder sample, the crystallites do not have imperfections or disorder capable to pin the flux lines. The Ginzburg Landau coherence length for MgB_2 is ξ=40A^0 meaning that only defects of such size can pin the flux lines. Defects of such size are difficult to be found inside the volume of a crystallites. On the other hand as prepared bulk samples show an enhanced J_c, indicating substantial bulk pinning due to crystalline boundaries, which can pin the vortices and cause for strong coupling between grains. In order to increase J_c and H_{irr} in MgB_2 the only route is to incorporate artificial pinning centers by doping. The studies on pinning mechanism in doped MgB_2 revealed interesting and significant improvement in understanding the critical current density variation with fields. Ag and Cu doping does not change the pinning mechanism but Zn doping in MgB_2 resulted in increase in J_c and pining force at high fields due to point pinning centers [76]. C doping in various forms in MgB_2 resulted in increase in J_c and H_{irr} due to different pinning mechanisms [78, 79]. In case of CNT doped MgB_2 surface pinning mechanism due to grain boundaries observed but reduced field maxima is observed at lower field (h_{max}=0.17) than un doped MgB_2 (h_{max}=0.2). Shift in h_{max} is due to enhancement in H_{irr} by CNT doping in MgB_2. In case of diamond form C doped MgB_2 pinning is due to point pinning centers. In this case h_{max} is observed at high fields (0.33) suggesting point pinning due to Nano particles of diamond

in MgB_2 [78]. In case of SiC doped MgB_2 a combination of substitution-induced defects and highly dispersed additives are responsible for increased flux pinning [79]. In case of metal oxide doped MgB_2 increase in grain connectivity, decrease in grain size and impurity Nano-particles contribute for the strong flux pinning resulting increase in J_c and H_{irr} over undoped MgB_2 [80, 81].

1.3.5 BiS_2 based layered superconductors

In search for new superconductors, Y. Mizuguchi in 2012 succeeded in discovering one more layered superconductor in which superconductivity is confined in BiS_2 planes [82]. In BiS_2 based superconductors crystal structure consists of stacking of BiS_2 superconducting bilayers separated by spacer layers. There are three major blocking or spacer layer groups which exist in BiS_2 based superconductors. They are *a)* $ReOBiS_2$, (RE=La, Ce, Pr, Nd, Yb) *b)* SrFBiS2 and *c)* $Bi_4O_4(SO_4)Bi_2S_4$. Common crystal structure for all BiS_2 based superconductors is tetragonal with space group I4/mmm [83-92]. The BiS_2 superconducting bilayers are categorized into a rock-salt structure. The crystal structure of major members of BiS_2 based superconductors family are shown in figure 1.6.

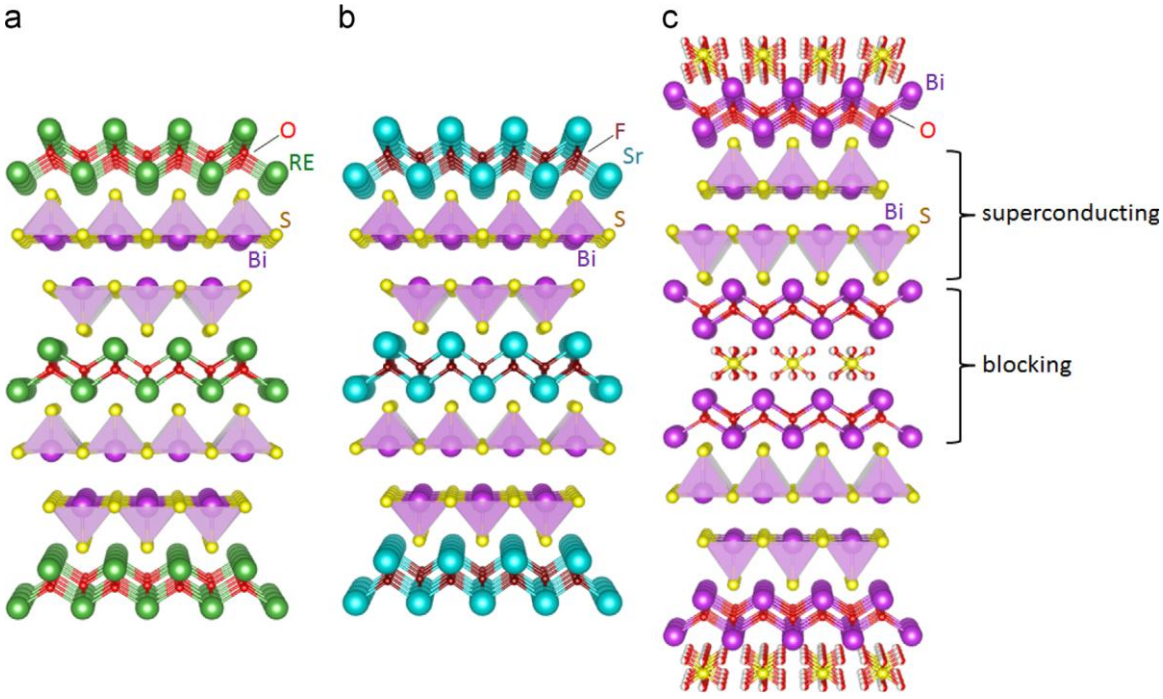

Figure 1.6 *Schematic images for crystal structure of various BiS2 based superconductors. (a)$REOBiS_2$ (b) $SrFBiS_2$ (c) $Bi_4O_4(SO_4)Bi_2S_4$.*

The basic composition of all these compounds show insulating behaviour but by introducing electrons in these compounds can turn to be superconductors. In $REOBiS_2$

group electron doping can be carried out by partial substitution of 'O' site in spacer layer by 'F', due to difference between the valance states of O^{2-} and F^{-} [85]. In this group maximum superconducting transition at 7.8K was observed in $LaO_{0.5}F_{0.5}BiS_2$ polycrystalline samples synthesized in solid state reaction method followed by annealing under 2GPa at 600^0C for 1hour in a cubic-anvil-type High Pressure (HP) synthesis apparatus [83]. In case of La replaced by Ce, the as grown polycrystalline samples of $CeO_{1-x}F_xBiS_2$ showed T_c at 3K with x>0.3. T_c enhanced to 6K after HP annealing. The important advantage of this superconductor is co-existence of ferromagnetic order, due to Ce moment, and superconducting nature [86-87]. The as grown $PrO_{0.5}F_{0.5}BiS_2$ superconductor showed T_c at 3.6K, which is increased to 5.5K by HP annealing [88, 92]. The promising material in $REOBiS_2$ group is $NdO_{1-x}F_xBiS_2$, which showed T_c at 5.5K synthesized at ambient conditions [90]. $YbO_{0.5}F_{0.5}BiS_2$ showed T_c at 5.3K but bulk superconducting property is not observed in this material [92]. The variation in T_c with RE element in $REO_{1-x}F_xBiS_2$ superconductors is due to the structural variation according to the radius of replacing element. $SrFBiS_2$ is an insulator with band gap, electron doping is achieved by replacing Sr by La. $Sr_{1-x}La_xBiS_2$, with x=0.5 showed T_c below 3K due to low carrier states [93, 94].

1.3.6 $Bi_4O_4S_3$ Superconductor

The first discovered BiS_2 based superconductor is $Bi_4O_4S_3$ with transition at 4.5K [82]. Electron doping in the insulting parent composition of $Bi_4O_4(SO_4)Bi_2S_4$, can be done with 50% SO_4 deficiency. With x=0.5 in $Bi_4O_4(SO_4)_{1-x}Bi_2S_4$, the superconducting phase can be obtained. $Bi_4O_4S_3$ is a type-2 superconductor with H_{c1}=7 to 15Oe and H_{c2}=31KOe. The coherence length ξ=100A^0 and the Hall coefficient is negative and field dependent. In-spite of its low T_c the hoping advantage of this superconductor is its layer structure. Extensive studies on its structure and bulk nature of superconductivity reveals that $Bi_4O_4S_3$ structure was composed of two spacer layers of Bi_2O_2, SO_4 and with one superconducting BiS_2 layer. $Bi_4O_4S_3$ is a polycrystalline material with tetragonal unit cell and lattice parameters a=3.9705A^0, c=41.3649A^0. $Bi_4O_4S_3$ is a strongly coupled conventional s-wave type superconductor with fully developed energy gap of Δ=1.54mev [95].

1.4 Composite Superconductors

A composite is a mixture of two or more distinct constituents or phases. The constituent's phases should have different properties and hence the composite properties are noticeably different from the properties of the constituents. The constituent that is

continuous often not always and present in the greater quantity in the composite is termed as matrix. The second constituent is referred to as the rein-forcing face as it enhances the mechanical properties of the matrix. Mechanical properties of the composites are function of the shape and dimensions of reinforcing phase. Super conducting composites are designed to exploit an improvement in the physical properties. Composite superconductors of high T_c superconductors with MgB_2 were studied recently by several groups. Composite system of MgO Nano-rod with BSCCO high T_c superconductor resulted in increase in J_c at close to liquid nitrogen temperatures [96]. Chemical doping and Nano particles addition/subtraction are the most useful ways to improve the structural, mechanical and superconducting properties of high T_c superconductors, making them suitable for high temperature and magnetic field applications. Addition and doping have different mechanisms in effecting the medium, for example in case of Ce doping at Ca site in Bi-2212, the hole density varies rapid in Cu-O plane because of differences in valances of Ca^{+2} and Ce^{+3} or Ce^{+4} [97, 98]. In case of Ce addition to Bi-2212, T_c and J_c decreased. In this case, Ce enters into crystal structure of Bi-2212 by replacing Cu atoms leading to decrease in *a* and *c* lattice parameters. This structural deformation resulted in T_c. Consequently grain size and connectivity is also decreased. The weak links, impurities between superconducting grains cause for the decrease in J_c [99]. From these studies we can understand clearly the different impact of doping and addition of an element to a superconductor. Addition of non-superconducting materials to high T_c superconductor resulted in significant improvement in J_c is observed by addition of Nano Al_2O_3 particles to YBCO superconductor [100]. In case of superconducting particles addition to another superconducting material is studied by several groups in order to improve J_c [101-104]. Composite system of BSCCO with MgB_2 resulted in significant improvement in superconducting and micro structural properties [102-103]. Whereas in case of composite system of YBCO and MgB_2 critical current density is decreased [104]. The difference in YBCO+MgB_2 and BISCCO+MgB_2 composite systems is due to different synthesis process of HTSC material. The more detailed study of composite systems is given in chapter 5.

As mentioned in previous sections the main disadvantages of MgB_2 is its fast flux creep at fields and temperatures. The disadvantage of Bi-2212 is its high anisotropic nature. The main advantage of Bi-2212 is its high thermal phase stability at high fields and temperatures. So in order to improve the phase stability of MgB_2 we have synthesized and studied the composite system of Bi-2212 as reinforcing phase and MgB_2 as matrix. In order

to improve anisotropy properties of Bi-2212, composite system of Bi-2212 as matrix and MgB_2 as reinforcing material has been studied in this thesis work.

1.5 Hetero Structures of Superconductors

The formation of layer over layer (vertical layer growth) or layer side by layer (Horizontal layer growth) with two or more different materials called Hetero structure. Hetero structures with layered superconducting materials are important in highly sophisticated applications. The Hetero structure of superconductors paves way not only for better understanding the superconductivity but also for potential use in high fields and electronic devices. The analysis of interfacial effects leads the research community to discover new High T_c superconductors. Best example for the advantages of Hetero structures in superconductivity field is Josephson junctions. A Josephson junction is made by sandwich of a thin non-superconducting layer in between two superconducting layers. Cooper pairs tunnel through insulating barrier from one superconducting layer to another superconducting layer [105]. The proximity effect plays an important role in analysing the Hetero structures of superconductors. The origin of the proximity phenomena at the interface of superconducting layer and normal layer is in the large spatial extension of the wave function of cooper pairs, which penetrates from superconducting layer to the normal layer at the distances comparable with the coherence length. As a result the layered superconducting to normal (S-N) structure, on the whole exhibits superconductivity with T_c smaller than the superconductor. The proximity effect is not exclusive for S-N systems, it can be applicable for a system with two different superconductors. Here the essential condition is T_c of one superconductor (S1) should be greater than the other superconductor (S2) ($T_{c1}>T_{c2}$). In the temperature range $T_{c2}<T<T_{c1}$, the proximity effect induce a finite local order parameter in low T_c superconductor (S2), leading to a nonzero attractive pairing interaction, which is called proximity-induced interface superconductivity [106]. Vortex lattice dynamics in a Hereto structures of two type-2 superconductors, Nb and V with T_{c1}=9K, T_{c2}=5.4K respectively, were studied by S. J. Carreira et al [107]. In this report they have made *V* pillars on Si substrate, on top of *V* pillars Nb layer was coated. Superconducting V pillars repel vortices and acts as anti-pinning centers below crossover field (H^*) above which they become normal and act as normal attractive flux pinning centers. These normal pinning centers causes for the depression of superconducting parameter in Nb film due to proximity effect. The pinning by depression of superconducting parameter induced by proximity effect of normal V pillars is less effective

than the pinning by vortex repulsion by superconducting pillars. Hetero structures in the form of multi layers of ferromagnetic and superconducting materials are studied extensively by several groups [108-110]. By adjusting the thickness of Ni/Nb multilayers were studied to observe the coexistence of superconductivity and ferromagnetism as observed in case of YBCO Nano particles [111]. Superconductivity in multilayer samples observed until t_{Ni}<14A^0, in this region Ni shows paramagnetic nature, ferromagnetic transformation from paramagnetic nature is observed in samples with t_{Ni}>14A^0, but superconducting nature of Nb suppressed due to proximity effect between superconducting Nb layer and ferromagnetic Ni layer. Coherence length is decreased but ferromagnetic order parameter dominates over coherence length leading suppression of superconductivity [108]. Thick films of Bi-2212 through melt quenching method resulted in synthesis of high quality superconducting phase [112-113]. Thick films of MgB_2 by HPCVD method resulted in increase in self-field J_c comparatively with single crystalline like MgB_2 films. Grain boundaries between columnar grains in thick films of MgB2 acts strong flux pinning centers [114].

We have prepared bulk Multilayers of Bi-2212 (T_{c1}=80K) and MgB_2 (T_{c2}=39K) superconductors in order to study the interfacial effects and to increase the critical current density.

1.6 Applications of Superconductors

Practical applications of superconductivity are steadily improving every year. The unusual physical properties of superconductors makes them more suitable for applications in specific areas. The conventional materials can be replaced by superconducting materials in many applications. The advanced technical and economic aspects of superconductive materials over conventional materials makes them more interesting. The main limiting factor of superconductors in practical applications is its high cost. However, in many fields to get the required performance the better way is to use superconducting technology. The size and weight of instruments and devices can be reduced by using superconducting components, compared to conventional techniques. Today superconductors have a wide range of commercial and industrial applications in energy generation, storage, and its transportation, in the fabrication of sensor materials, in microwave communication systems and most importantly in high field magnets. Some of the main application sectors of superconducting materials are tabulated in table 1.1 [115].

Table.1.1 *Applications of HTS superconductors in various fields.*

Area/Field	Applications
Energy/Power: Generation & Storage	Superconducting bearings for flywheel storage Cables, Generators, SMES,
Energy/Power: Distribution Magnets	Transformers, Current leads, False Current Limiters, Motors. NMR, MRI instruments, Magnetic confinement of plasma in Fusion reactors, Particle accelerators, High field magnets.
Electronics	In microwave filters, Digital logic circuits as RSFQ, Sensor applications
Biomedical	Detection of extremely small Neuro magnetic fields, Magneto encephalano graphy (MEG), Magneto cardio graphy (MCG).
Industrial	Magnets for shielding and separation, sensors R & D Superconducting RF cavities in particle accelerators, Synchrotrons and High field magnets
Other applications	Magnetic levitation, Magneto hydrodynamics, Space applications

1.7 Motivation

In this work we have carried out studies on three different layered superconductors with the objective of understanding *(1)* the effect of composition and doping on the superconducting properties of Bismuth oxy sulphide, *(2)* to study the composite and hetero structures of Bi-2212 and MgB_2 superconductors with the motto of enhancement in critical current density and *(3)* to understand the vortex pinning mechanisms in these superconducting materials.

In specific,

- To synthesis $Bi_4O_4S_3$ with 5 and 10% excess Bi_2O_3 and study the effect on critical current density and pinning mechanism.
- To study the effect of Ca doping at Bi site in $Bi_4O_4S_3$.

- To prepare and characterize the composite samples of Bi-2212 and MgB_2 superconductors.
- To prepare and characterize the Hetero structures of Bi-2212 and MgB_2 superconductors.

1.8 Organization of thesis

The thesis consists of six chapters with the contents described below.

Chapter 1:

Chapter-1 contains the basics of superconductors along with their importance in various applications, followed by a brief introduction to layered superconductors like Bismuth Oxy Sulphide, Bi-2212 and MgB_2. Later, we have discussed the advantages of composite and Hetero structures of high T_c superconductors and MgB_2.

Chapter 2:

In this chapter, we have discussed about the synthesis of superconducting materials and the techniques used to characterize the prepared superconductors.

Chapter 3:

In this chapter we have discussed about the critical current density and pinning mechanism in superconducting Bismuth Oxy Sulphide samples synthesized with 5% and 10% of excess Bi_2O_3 over and above the required quantity as per stoichiometric composition of $Bi_4O_4S_3$ phase.

Chapter 4:

In this chapter we have discussed about the effect of Ca doping at Bi site on the structure and superconducting properties of $Bi_4O_4S_3$.

Chapter 5:

In this chapter we have presented the studies on composite system of Bi-2212 and MgB_2 superconductors.

Chapter 6:

In this chapter we have discussed about the properties of Hetero structure of Bi-2212 and MgB_2 superconductors in the form of bulk multilayer.

Summary and conclusions are given at the end of thesis.

References

[1]. H. K. Onnes, *KNAW proceedings*, **10**, 200, (1908).

[2]. H. K. Onnes, *Leiden Commun*. **124**, 1226 (1911).

[3]. W. Meissner, R. Oschenfeld, Naturwiss **21**, 787 (1933).

[4]. J. R. Schrieffer, M. Tinkham, *Rev. Mod. Phys.*, **71**, S313 (1999).

[5]. V.V. Schmidt, 1st edition, *Springer-Verlag Berlin Heidelberg New York* (1997).

[6]. Rudolf P. Huebener, *Springer International Publishing Switzerland*, 105-117 (2015).

[7]. G. Bednorz, K.A. Muller, *Zeitschrift für Physik B*, **64**, 189 (1986).

[8]. M.K. Wu, J.R. Ashburn, C. J. Torng, P. H. Hor, R. L. Meng, L. Gao, Q. Huang, C. W. Chu, *Physical Review Letter*, **58**, 908 (1987).

[9]. A. Schilling, M. Cartoni, J. Guo, H. R. Ott, *Nature*, **363**, 56 (1993).

[10]. B. Seeber, *OIP Publishing*, Bristol (1998).

[11]. L.M. Rubin, T.P. Orlando, J.B. Vander Sande, G. Gorman, R. Savoy, R. Swope, R. Beyers, *Applied Physics Letters*, **61**, 1977 (1992).

[12]. P. Majewski, *Superconductor Science & Technology*, **10**, 453 (1997).

[13]. E. Zacharias, and R. Singh, *Physica C*, **247**, 221-230 (1995).

[14]. Hink D.G, L. Soderholm, D.W. Capone, B. Dabrowski, A. W. Mitchell, and D. Shi, *Appl. Phys. Lett*, **53**, 423 (1988).

[15]. F.H. Garzon, J. G.Berry, and I. D. Raistrick, *Appl. Phys. Lett*., **53**, 805 (1988).

[16]. A. Inoue, H. Kimura, K. Matsuzaki, A. Tsai, and T. Masumoto, *Japan. J. Appl. Phys*., **27**, L941 (1988).

[17]. H. Zheng and J. D. Mackenzie, *Phys. Rev. B*., **38**, 7166 (1988).

[18]. R. Singh and E. Zacharias, *J. Phys. D. Appl. Phys*., **23**, 199-204,(1990).

[19]. R .Singh, *J. Phys. D: Appl. Phys*., **22**, 1523-1527, (1989).

[20]. H. Maeda, Y. Tanaka, M. Fukutomi, T. Asano, *Jpn. J. Appl. Phys*., **27**, L209-L210 (1988).

[21]. J. M. Tarascon, W. R. McKinnon, P. Barboux, D. M. Hwang, B. G. Bagley, L. H. Greene, G. W. Hull, Y. LePage, N. Stoffel, and M. Giroud, *Phy. Rev. B*, **38**, 13 (1988).

[22]. H. Maeda, Y. Tanaka, M. Fukutomi, T. Asano, *Japanese Journal of Applied Physics*, **27**, L209 (1988).

[23]. W. Wong-Ng and S.W. Freiman, *Applied Superconductivity*, **2**, 163 (1994).

[24]. T. Komatsu, R. Sato, K. Imai, K. Matusita, T. Yamashita, *Japanese Journal of Applied Physics*, **27**, L550 (1988).

[25]. T. Komatsu, R. Sato, K. Imai, K. Matusita, T. Yamashita, *Japanese Journal of Applied Physics*, **27**, L533 (1988).

[26]. T. Komatsu, R. Sato, K. Imai, K. Matusita, T. Yamashita, *Japanese Journal of Applied Physics*, **27**, L1839 (1988).

[27]. J. E. Fischer, P. A. Heiney, P.K. Davies, D. Vaknin, *Physical Review B*, **39**, 2752 (1989).

[28]. R. M. Hazen, C. T. Prewitt, R. J. Angel, *Physical Review Letter*, **60**, 1174 (1988).

[29]. J. O. Li, C. Chen, D. Y. Yang, F.H. Li, Y.S. Yao, Z.Y. Ran, *Physica B*, **74**, 165 (1988).

[30]. Y. Matsui, H. Maeda, Y. Tanaka, S. Horiuchi, *Japanese Journal of Applied Physics*, **27**, L361 (1988).

[31]. C. Namgung, J.T.S. Irvine, E. E. Lachowski, A.R. West, *Superconductor Science & Technology*, **2**, 140 (1989).

[32]. C. Patterson, P.D. Hatton, R. J. Nelmes, X. Chu, *Superconductor Science & Technology*, **3,** 197 (1990).

[33]. E. Zacharias and R. Singh, *Solid state communications*, **93**, No.2, 135-138, (1995).

[34]. V. Petricek, Y. Gao, P. Lee, P. Coopers, *Physical Review B*, **42**, 387 (1990).

[35]. S. A. Sunshine, T. Siegrist, L. F. Schneemeyer, D. W. Murphy, *Physical Review B*, **38**, 893 (1988).

[36]. A. Yamamoto, M. Onada, E. Takayama, Muromachi, *Physical Review B*, **42**, 4228 (1990).

[37]. E. A. Hewat, P. Bordet, J. J. Capponi, *Physica C*, **619**, 153-155 (1988).

[38]. P. Majewski, *Journal of Materials Research*, **15**, 854 (2000).

[39]. Lang, Thomas, *PhD diss., homas Lang, Techn. Wiss*. ETH Zürich (1997).

[40]. D. Giller, A. Shaulov and Y. Yeshurun, *Physics B*, **284-288**, 687-688 (2000).

[41]. Donglu Shi, Mark Boley, J. Chen, U. Welp and K. Vander Voort, *Physica C*, **162-164**, 927-928 (1989).

[42]. P. Fabbricator, C. Priano, A. sciutti, G. Gemme, R. Musenich and R. Parodi, *Physical Review B*, **54**, 17, 12543-12550 (1996).

[43]. T. Matsushita, N. Ihara and M. Kiuchi, In*4th International Conference and Exhibition: World Congress on Superconductivity*, **1**, 337-346 (1995).

[44]. R. D. Hoffmann and R. Pottgen, *Z. Kristallogr*, **216,** 127-145 (2001).

[45]. Monika Mudgal, V. P. S Awana and H. Kishan, *arXiv preprint arXiv:0811.4224* (2008).

[46]. J. Nagamastu, N. Nakagawa, T. Muranaka, Y. Zenitani, and J. Akimitsu, *Nature*, **410**, 63, (2001).

[47]. D. Tzeli, A. Mavridis, *J. Phys. Chem. A*, **109**, 10663 (2005).

[48]. L. Ivanovskiĭ, *Physics of the Solid State*, *45*, 1829 (2003).

[49]. C. Buzea, T. Yamashita, *Supercond. Sci. Technol.*, **14**, R115 (2001).

[50]. Y. Eltsev, S. Lee, K. Nakao, N. Chikumoto, S. Tajima, N. Koshizuka, M. Murakami, *Phys. Rev. B*, **65**, 140501 (2002).

[51]. M. Eisterer, M. Zehetmayer, H. W. Weber, *Phys. Rev. Lett*., **90**, 247002 (2003).

[52]. O. F. de Lima, R. A. Ribeiro, M. A. Avila, C. A. Cardoso, A. A. Coelho, *Phys. Rev. Lett.*, **86**, 5974 (2001).

[53]. D. K. Finnemore, J. E. Ostenson, S. L. Bud'ko, G. Lapertot, P. C. Canfield, *Phys. Rev. Lett.*, **86**, 2420 (2001).

[54]. M. Iavarone, G. Karapetrov, A. E. Koshelev,W. K. Kwok, G.W. Crabtree,W. N. Kang, E. M. Choi, H. J. Kim, S. I. Lee, *Supercond. Sci. Technol*,. **17**, S106 (2004).

[55]. H. J. Choi, D. Roundy, H. Sun, M. L. Cohen, S. G. Louie, *Nature*, **418**, 758 (2002).

[56]. P. C. Canfield, D. K. Finnemore, S. L. Bud'ko, J. E. Ostenson, G. Lapertot, C. E. Cunningham, C. Petrovic, *Phys. Rev. Lett*., **86**, 2423 (2001).

[57]. M. N. Kunchur, S. I. Lee, W. N. Kang, *Phys. Rev. B*, **68**, 064516 (2003).

[58]. W. Goldacker, S. I. Schlachter, B. Obst, B. Liu, J. Reiner, S. Zimmer, *Supercond. Sci. Technol*., **17**, S363 (2004).

[59]. S. Soltanian, X. L. Wang, I. Kusevic, E. Babic, A. H. Li, M. J. Qin, J. Horvat, H. K. Liu, E. W. Collings, E. Lee, M. D. Sumption, S. X. Dou, *Physica C*, **361**, 84 (2001).

[60]. Y. Takano, H. Takeya, H. Fujii, H. Kumakura, T. Hatano, K. Togano, H. Kito, H. Ihara, *Appl. Phys. Lett*., **78**, 2914 (2001).

[61]. S. L. Li, H. H. Wen, Z. W. Zhao, Y. M. Ni, Z. A. Ren, G. C. Che, H. P. Yang, Z. Y. Liu, Z. X. Zhao, *Phys. Rev. B*, **64**, 094522 (2001).

[62]. D. K. Finnemore, J. E. Ostenson, S. L. Bud'ko, G. Lapertot, P. C. Canfield, *Phys. Rev. Lett.*, **86**, 2420 (2001).

[63]. S. L. Bud'ko, C. Petrovic, G. Lapertot, C. E. Cunningham, P. C. Canfield, M. H. Jung, A. H. Lacerda, *Phys. Rev. B*, **63**, 220503 (2001).

[64]. M. D. Sumption, M. Bhatia, M. Rindfleisch, M. Tomsic, S. Soltanian, S. X. Dou, E. W. Collings, *Appl. Phys. Lett*., **86**, 092507 (2005).

[65]. E. W. Collings, M. D. Sumption, M. Bhatia, M. A. Susner, S. D. Bohnenstiehl, *Supercond. Sci. Technol.,* **21**, 103001 (2008).

[66]. M. Eisterer, Supercond. *Sci. Technol*., **20,** R47 (2007).

[67]. T. Matsushita, M. Kiuchi, A. Yamamoto, J. Shimoyama, K. Kishio, *Supercond. Sci. Technol*., **21**, 015008 (2008).

[68]. Y. P. Sun, W. H. Song, B. Zhao, J. J. Du, H. H. Wen, Z. X. Zhao, H. C. Ku, *Appl. Phys. Lett.,* **76**, 3795 (2000).

[69]. D. C. Larblestier, L. D. Cooley, M. O. Rikel, A. A. Polyanskii, J. Jiang, S. Patnaik, X. Y. Cai, D. M. Feldmann, A. Gurevich, A. A. Squitieri, M. T. Naus, C. B. Eom, E. E. Hellstrom, R. J. Cava, K. A.Regan, N. Rogado, M. A. Hayward, T. He, J. S. Slusky, P. Khalifah, K. Inumaru, M. Haas, *Nature*, **410**, 186 (2001).

[70]. E. Martínez, P. Mikheenko, M. Martínez-López, A. Millán, A. Bevan, J. S. Abell, *Phys. Rev. B*, **75**, 134515 (2007).

[71]. H. Kitaguchi, A. Matsumoto, H. Kumakura, T. Doi, H. Yamamoto, K. Saitoh, H. Sosiati, S. Hata, *Appl. Phys. Lett.*, **85**, 2842 (2004).

[72]. X. Y. Song, S. E. Babcock, C. B. Eom, D. C. Larbalestier, R. Ka, R. J. Cava, S. L. Bud'ko, P. C.Canfield, D. K. Finnemore, *Supercond. Sci. Technol*., **15**, 511 (2002).

[73]. A. Yamamoto, J. Shimoyama, S. Ueda, Y. Kastura, I. Iwayama, S. Horii, K. Kishio, *Appl. Phys. Lett.*, **86**, 212505 (2005).

[74]. S. Li, T.White, K. Laursen, T. T. Tan, C. Q. Sun, Z. L. Dong, Y. Li, S. H. Zho, J. Horvat, S. X. Dou, *Appl. Phys. Lett*., **83**, 314 (2005).

[75]. V. Ferrando, P. Orgiani, A. V. Pogrebnyakov, J. Chen, Q. Li, J.M. Redwing, X. X. Xi, J. E. Giencke, C. B. Eom, Q. R. Feng, J. B. Betts, C. H. Mielke, *Appl. Phys. Lett*., **87**, 252509 (2005).

[76]. D. A. Cardwell, N. Hari Babu, M. Kambara and A. M. Campbell, *Physica C*, **373-376**, 1262-1265 (2002).

[77]. M. Pissas, E. Moraitakis, D. Stamopoulos, G. Papavassilion, V. Psycharis and S. Koutandos, *Journal of Superconductivity*, 1-5 (2001).

[78]. C. H. Cheng, Y. Yang, P. Munroe and Y. Zhao, *Supercond.Sci. Tech*., **20**, 296-301 (2007).

[79]. S.X. Dou, S. Soltanian, J. Horvat, X. L. Wang, S.H. Zhou, M. Lonescu and H.K.Liu, *Appl. Phys. Lett*, **81**, 18, (2002).

[80]. Y. Feng, Y. Zhao, A. K. Pradhan, C. H. Cheng, J. K. F. You, L. Zhou, N. Koshizuka and M. Murakami, *J. Appl. Phys.*, **92**, 5, (2002).

[81]. C. Cheng and Y. Zhao, *Physica C*, **463-465**, 220-224 (2007).

[82]. Y. Mizuguchi, H. Fujihisa, Y. Gotoh, K. Suzuki, H. Usui, K. Kuroki, S. Demura, Y. Takano, H. Izawa, O. Miura, *Phys. Rev. B*, **86**, 220510 (2012).

[83]. Y. Mizuguchi, S. Demura, K. Deguchi, Y. Takano, H. Fujihisa, Y. Gotoh, H. Izawa, O. Miura, *J. Phys. Soc. Jpn.*, **81**,114725 (2012).

[84]. Y. Mizuguchi, T. Hiroi, J.Kajitani, H. Takatsu, H. Kadowaki, O. Miura, *J. Phys. Soc. Jpn.*, **83**, 053704 (2014).

[85]. Y. Kamihara, T. Watanabe, M. Hirano, H. Hosono, *J. Am. Chem. Soc.*, **130**, 3296 (2008).

[86]. J. Xing, S. Li, X. Ding, H. Yang, H. H. Wen, *Phys. Rev. B*, **86**, 214518 (2012).

[87]. S. Demura, K. Deguchi, Y. Mizuguchi, K. Sato, R. Honjyo, A. Yamashita, T. Yamaki, H. Hara, T. Watanabe, S. J. Denholme, M. Fujioka, H. Okazaki, T. Ozaki, O.Miura, T.Yamaguchi, H.Takeya, Y.Takano, *arXiv*:**1311**, 4267 (2013).

[88]. R. Jha, A. Kumar, S. K. Singh, V. P. S. Awana, *J. Supercond. Novel Magn. 26*, **26**, 499 (2013).

[89]. J. Kajitani, K. Deguchi, T. Hiroi, A. Omachi, S. Demura, Y. Takano, O. Miura, Y. Mizuguchi, *J. Phys. Soc. Jpn*., **83**, 065002 (2014).

[90]. S. Demura, Y. Mizuguchi, K. Deguchi, H. Okazaki, H. Hara, T. Watanabe, S. J. Denholme, M. Fujioka, T. Ozaki, H. Fujihisa, Y. Gotoh, O. Miura, T. Yamaguchi, H. Takeya, Y. Takano, *J. Phys. Soc. Jpn*., **82**, 033708 (2013).

[91]. R. Jha, A. Kumar, S. K. Singh, V. P. S. Awana, *J. Appl. Phys*., **113**, 056102113 (2013).

[92]. D. Yazici, K. Huang, B. D. White, A. H. Chang, A. J. Friedman, M. B. Maple, *Philos. Mag.*, **93**, 673 (2012).

[93]. H. Lei, K. Wang, M. Abeykoon, E. S. Bozin, C. Petrovic, *Inorg. Chem*., **52**, 10685 (2013).

[94]. X. Lin, X. Ni, B. Chen, X. Xu, X. Yang, J. Dai, Y. Li, X. Yang, Y. Luo, Q. Tao, G. Cao, Z. Xu, *Phys. Rev. B*, **87**, 020504 (2013).

[95]. S. K. Singh, A. Kumar, B. Gahtori, Shruti, G. Sharma, S. Patnaik, and V. P. S. Awana, *J. Am. Chem. Soc*., **134**, 16504-16507 (2012).

[96]. W. Wei, J. Schwartz, K.C. Goretta, U. Balachandran and A. Bhargava, *Physica C*, **298**, 279-288 (1998).

[97]. D. Rama sita and R. Singh, *Solid state communication*, **94**, 12, 969-972, (1995).

[98]. F. Jordan, O. Pefia, R. Horyn, *Physica C*, **235-240**, 945-946 (1994).

[99]. S. Bal, M. Dorgruer, G. Yidirim, A. Varilci, C. Terzioglu, Y. Zalaoglu., *J. Supercond. Nov. Magn.*, **25**, 847-856 (2012).

[100]. A. Mellekh, M. Zouaoui, F. Ben Azzouz, M. Annabi, and M. Ben Salem, *Solid State Commun.*, **140**, 318-323 (2006).

[101]. Y. Y. Xu, J. Ren, S. H. Han, and H. Zhang, *International Journal of Modern Physics B*, **21**, 18&19, 3352-3354 (2007).

[102]. M. Dogruer et.al, *Journal of alloys and compounds*, **556**, 143-152 (2013).

[103]. D. Tripathi, T. K. Dey J. *Supercond. Nov. Magn*., **28,** 2025-2032 (2015).

[104]. X. F .Rui, X. F. Sun, X. Xu, L. Zhang, and H. Zhang, *International Journal of Modern Physics B*, **99**, 1-3, 375-377 (2005).

[105]. S. Lee, C. Tarantini, P. Gao, J. Jiang, J. D. Weiss, F. Kametani, C. M. Folkman, Y. Zhang, X. Q. Pan, E. E. Hellstrom, D. C. Larbalestier, and C. B. Eom, *Nature Materials*, **12**, 392-396 (2013).

[106]. V. Cherkez, J.C. Cuevas, C. Brun, T. Cren, G. Menard, F. Debontridder, V. S. Stolyarov, and D. Roditchev, *Phy. Rev. X*, **4**, 011033 (2014).

[107]. S. J. Carreira, C. Chiliotte, V. Bekeris, Y. J. Rosen, C. Monton, and Ivan K. Schuller, *Supercond. Sci. Technol*., **27**, 085007 (2014).

[108]. J. E. Mattson, R. M. Osgood, C. D. Potter, C. H. Sowers, and S. D. Bader, *J. Vac. Sci. Technol. A*, **15**, 3 (1997).

[109]. C. Z. Antoine, S. Berry, M. Aurino, J. F. Jacquot, J. C. Villegier, G. Lamura, and A. Andreone, *IEEE Trans. on Appl. Supercon.*, **21**, 3, 2601-2604, (2011).

[110]. J. E. Mattson, C. D. Potter, M. J. Conover, C. H. Sowers and S. D. Bader, *Phy. Rev. B*, **55**, 1, (1997).

[111]. Z. Zhu, D. Gao, C. Dong, G. Yang, Jing. Zhang, J. Zhang, Z. Shi, H. Gao, and D. Xue, *Phys. Chem. Chem. Phys*., **14**, 3859-3863 (2012).

[112]. B. K. Bahaduria, K. Som, and S. P. Sen Gupta, *J.Materials Sci. L*., **8**, 520-522 (1989).

[113]. D. Bhul, T. Lang, and L. J. Gauckler, *Supercond. Sci. Tech*., **10**, 32-40 (1997).

[114]. Mahipal Ranot, P. V. Duong, A. Bharadwaj, and W. N. Kang, *Progress in superconductivity and cryogenics*, **17**, 2 (2015).

[115]. H. W. Weijers, U. P. Trociewitz, K. Marken, M. Meinesz, H. Miao, J. Schwartz, *Supercond. Sci. Technol*., **17**, 636 (2004).

CHAPTER 2

Experimental Techniques

This chapter covers the synthesis methods of various superconducting samples and their characterization techniques such as XRD, FESEM, TEM, VSM and Four Probe methods.

2.1 Synthesis Methods

2.1.1 Solid state Reaction Route

The solid state reaction is widely used method for the preparation of materials with correct molar ratio. This method is often defined as reactions between two solids. The method consists of weighing, grinding, pressing and sintering of the sample.

2.1.1.1 Sintering Mechanism

Sintering may be considered as the process by which an assembly of particles, compacted under pressure or simply confined in a container, chemically bond themselves into a coherent body by diffusion under the influence of an elevated temperature. The temperature is usually below the melting point of the major constituent. Much of the difficulty in defining and analysing sintering is based on the many changes within the material that may take place simultaneously or consecutively. The driving force of sintering process is reduction of surface energy of the particles caused by decreasing their vapour-solid interfaces. During the diffusion process, the pores occurring in the "green compact" (or raw material), diminish or even close up, resulting in densification of the part and improvement of its mechanical properties as shown in figure 2.1. Decrease of the porosity, caused by the sintering process, is determined by the level of initial porosity of the 'green' compact, sintering temperature and time. Sintering is enhanced if a liquid phase takes part in the process (liquid phase sintering).

Sintering (firing) of pure oxide ceramics require relatively long time and high temperature because the diffusion proceeds in solid state. Applying pressure decreases sintering time and the resulted porosity decreases. Tunnel kilns and periodic kilns are

commonly used for ceramics sintering (firing). In periodic kilns heating and cooling sintering stages are conducted according to a prescribed procedure. In tunnel kilns the sintered parts are conveyed through different temperature zones.

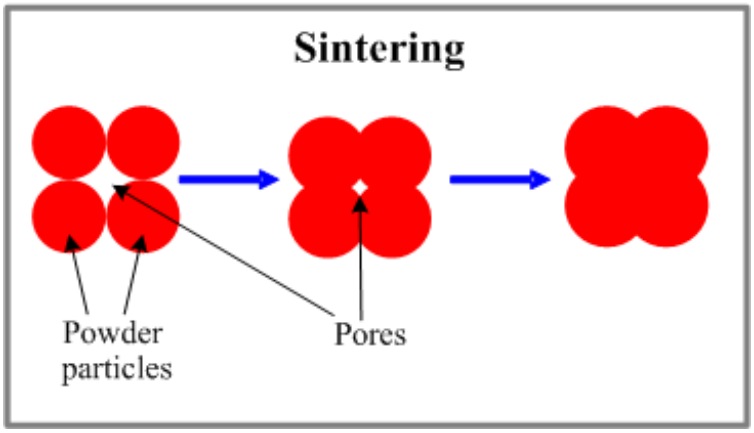

Figure 2.1 *Schematic of the sintering mechanism*

Typical tunnel kiln has three zones:

1. Preheat zone for removing lubricant and other organic materials.
2. Sintering zone where the diffusion occurs.
3. Cooling zone where the sintered parts cool down.

Sintering process may be conducted in air or in inert atmosphere [1].

The polycrystalline $Bi_4O_4S_3$ samples were prepared using conventional solid state reaction method. In this method pure Bi_2O_3 powder, Bismuth metal granules and Sulphur flakes (all from sigma Aldrich with purity>99.99%) were mixed in stoichiometric ratio and ground for 1 hour using an agate mortar. The mixture was used to make pellets using a hydraulic press at ambient conditions. The pellet samples were sealed in a quartz tube under the vacuum of $5x10^{-4}$Torr and sintered at 510^0C for 18hrs followed by furnace cooling. The same procedure was repeated twice to get better homogeneity.

2.1.2 Glass ceramic route

Synthesis of Superconductors through glass ceramic route consists two processing steps. Step 1 consists glass preparation and step 2 consists devitrification of the glassy precursors by proper heat treatment.

In the first step the glasses can be prepared through melt quenching method. In this method raw materials will be mixed according to the stoichiometric ratio, grinded thoroughly, and keep inside a preheated furnace then raise the temperature close to melting

temperature of constituent compound (not very close). Keep the molten liquid at this temperature for 10-15 minutes for thorough mixing then quench this liquid to room temperature in a very short period of time as much as possible (with possible cooling rate~10^3K/S). This random cooling from high temperature to room temperature makes the liquid to solidify in random orientation due to short period. This amorphous solid with high viscosity is called Glass. In the second step, superconducting phase can be obtained with these glass precursors by allowing them to go through proper heat treatment. The heat treatment temperature and duration are important parameters to be taken care while preparation. This heat treatment process followed by slow cooling (generally furnace cooling) gives well crystallized phase with proper orientation [2].

We have prepared Bi-2212 glasses through melt quenching method with initial composition of $Bi_4Sr_3Ca_3Cu_4O_x$, (simply Bi-4334) which is optimum composition to get single Bi-2212 high T_c phase with proper orientation along C axis normal to the sample surface [3]. The high purity (99.99%) powders of Bi_2O_3, $SrCO_3$, $CaCO_3$, CuO were weighed as per Bi-4334 composition, grinded thoroughly for 2hours using agate mortar and then calcined at 800^{o}C for 24hours. The reacted black powder was melted at 1000^{0}C in a platinum crucible and held at that temperature for 10 minutes to ensure thorough mixing and then quenched quickly between two copper blocks. The obtained shiny glasses of 0.5-1mm thickness were annealed in air at 820^{o}C for various duration.

2.2 X-ray Diffractometer

X-ray diffraction (XRD) is a well-known technique used for the identification of material phases and crystal structure of the samples (lattice constant, crystallite size etc.). It is a noncontact and non-destructive technique which makes it ideal for in situ studies. Chemical composition and physical properties like strain also can be characterized with the help of XRD patterns of the samples.

X-ray Diffractometer works based on Brag's diffraction principle. When x-rays strike the any material, a part of it gets transmitted, some get scattered and a part of it gives rise to fluorescence. If the material is crystalline, they get scattered from different sets of planes containing atoms arranged in certain order (figure 2.2). The scattered beam undergoes both constructive as well as destructive interference depending upon the path difference of the interfering waves. If θ is the angle of incidence of the X-rays with respect to the plane of the crystal, then constructive interference occurs when

$$2dsin\theta = n\lambda \quad (2.1)$$

where d is inter-planar distance and λ is wavelength of X-rays employed (λ for Cu target is 1.5406A^o). Thus for each set of planes, there is a particular value of diffraction angle θ for which the scattered beams interfere constructively to give a strong reflected beam.

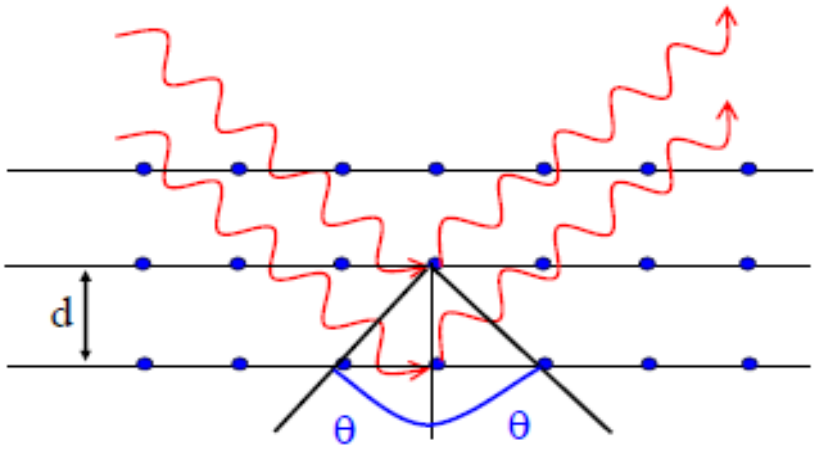

Figure 2.2 *Set of atomic planes reflecting X-rays.*

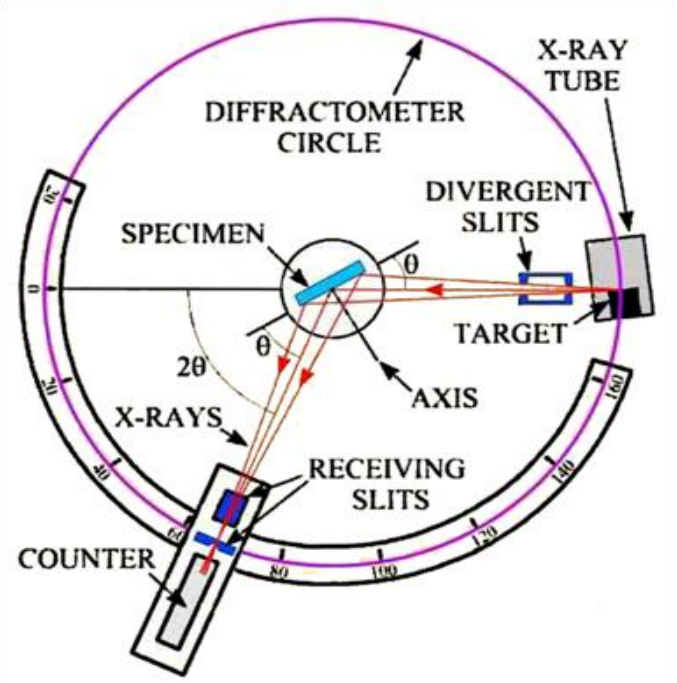

Figure 2.3 *Schematic of an X-ray diffractometer.*

The schematic of an X-ray diffractometer is shown in figure 2.3. The X-ray diffractometer consists of three basic units, an X-ray tube, sample holder and an X-ray detector. The electrons generated by heating the filament are accelerated towards the target by applying voltage and are made to incident on the target material. Thus, electrons having

sufficient energy knock out electrons from the target material resulting in characteristic X-ray emission spectra. The characteristic spectra consists of several components, the most being used for X-ray diffraction were K_α and K_β. The monochromatic X-rays were obtained after passing the characteristic X-rays through the crystal monochromator. The monochromatic X-rays thus are collimated and made to incident on the sample. The X-rays which are satisfying the Bragg's law for constructive interference will be collected by a detector. The detected x rays generate electron-hole pairs in the detector. The electronic attached to the detector converts the charge into voltage pulses which is directly proportional to the intensity of the diffracted beam. Each peak in the XRD pattern corresponds to one set of parallel planes and their corresponding miller indices are indicated above the peak. The peak position, peak width and peak height are the three important parameters for the determination of structural properties [4-6]. The possible parameters can be obtained from the XRD are given in detail as shown in figure 2.4.

XRD pattern is characteristic of a material. XRD pattern gives us information about the crystal structure, lattice parameter, lattice plane spacing, stress etc. the size and stress related broadening have different angle dependence. Diffraction peaks consists of both Bragg components like size and strain broadening and non-Bragg components like background and instrumental broadening. It can be separated out using Rietveld refinement technique.

The Rietveld refinement is performed using FullProf suite program with multi-phase tetragonal structure having space group I4/mmm for Bi4O4S3 [7]. The profile used for the fitting is Thompson-Cox-Hastings pseudo-Voigt convoluted with axial divergence asymmetry function. The FullProf program has been mainly developed for Rietveld analysis (structure profile refinement) of neutron (constant wavelength, time of flight, nuclear and magnetic scattering) or X-ray powder diffraction data collected at constant or variable step in scattering angle 2θ. The program can be also used as a Profile Matching (or pattern decomposition using Le Bail method) tool, without the knowledge of the structure. Single crystal refinement can also be performed alone or in combination with powder data. Energy dispersive X-ray data can also be treated but only for profile matching. The PCR file is the input parameters file for the FullProf diffraction profile.

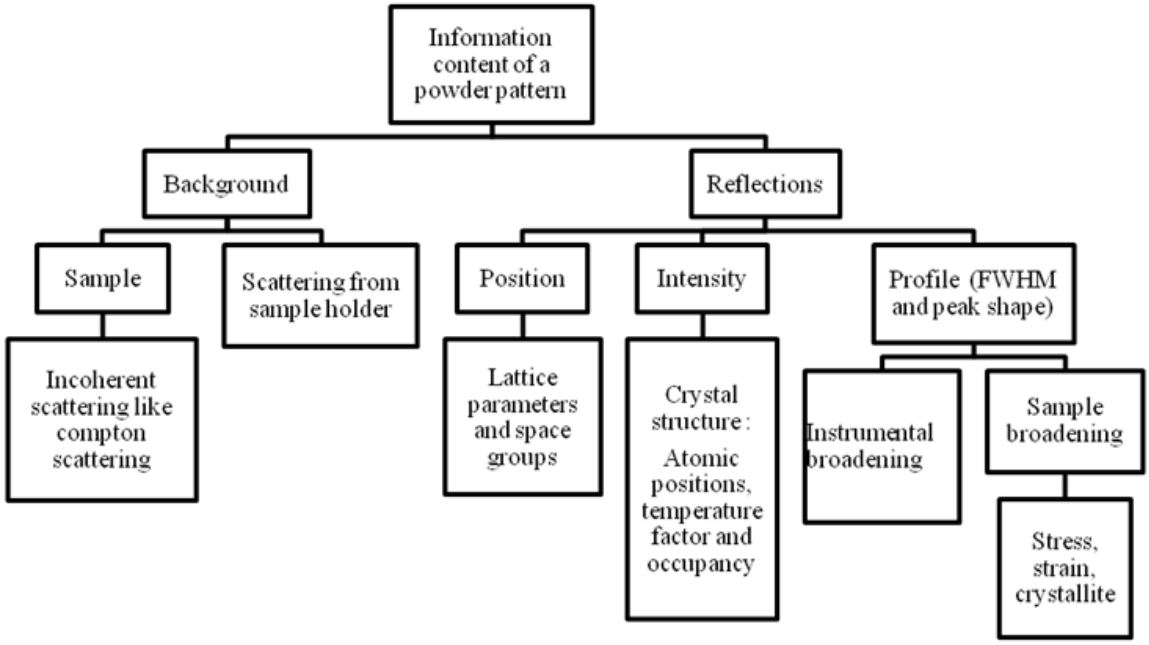

Figure 2.4 *Information contains from the XRD pattern regarding a material.*

2.3 Field Emission Scanning Electron Microscopy

Field emission scanning electron microscope (FESEM) is one type of microscope capable of producing high-resolution images of a sample surface. The principle of electron microscope is same as that of light microscope but instead of using visible light it uses high energetic electrons as a source. The resolution of optical microscope is limited by its wavelength whereas in electron microscope wavelength of the electrons can be varied with the applied voltage.

$$\lambda = \frac{1.5}{\sqrt{V}} \text{ nm} \tag{2.2}$$

Smaller wavelength electrons generated from the field emission gun provides an opportunity to see the atomic structures of the samples. The resolution of any microscope, is determined by the spot size on the surface of the sample, quality of lenses used for focussing and on the performance of the electron gun i.e. brightness. In field emission electron microscope the spot size is in the range of 5 to 25 nm [8].

The sharpness and visibility of an image depends on electron probe size (d_p), electron probe current (i_p), electron probe convergence angle (α_p) and electron beam accelerating voltage (V_o).Brightness (β) also depends on the above four parameters and is

defined as the beam current per unit area per unit solid angle [Joseph Goldstein].The small is the spot size the more is the brightness.

$$\beta = \frac{Current}{area * solid\ angle} = \frac{i_p}{\left(\frac{\pi d_p^2}{4}\right) * \pi \alpha_p^2} \tag{2.3}$$

Electrons emitted from a field emission source are accelerated with an accelerating voltage of V_o. The electrons in the high vacuum column are known as primary electrons are focussed and deflected by electronic lenses to produce a narrow scan beam that bombards the object. As a result, secondary electrons are emitted from each spot on the object. The angle and velocity of these secondary electrons relates to the surface structure of the object. A detector catches the secondary electrons and produces an electronic signal. This signal is amplified and transformed to a video scan-image that can be seen on a monitor or to a digital image that can be saved and processed further.

FESEM employs a beam of electrons to produce magnified and high resolution images of the samples. Electrons have wavelength 10^5 times smaller than that of visible light resulting in higher resolution and magnification compared to confocal microscope. The electrons falling on the sample interact with the atoms of the sample results in emission of secondary electrons (SE), back scattered electrons (BSE), X-rays, light, specimen current and transmitted electrons. Resolution of a scanning electron microscope depends on factors like probe diameter at the sample surface, probe and depth of penetration of the primary electron beam into the specimen. Also the SEM columns were prone to beam crossover along the beam path degrading the image resolution. Each cross-over requires a lens to control it, making it very long. Hence a design devoid cross-over was of a great need.

In order to meet the above requirements the FESEM was equipped with a lens column (Gemini) consisting of an Electron source (Tungsten), Electromagnetic lenses and In-lens detector (figure 2.5). The tungsten filament is covered by a layer of ZrO2 as it reduces the work function of tungsten and helps in enhanced emission. The anode present below the filament helps in accelerating the emitted electrons. The beam is accelerated to a high potential in the full length of the column. The emitted electrons pass through electromagnetic lenses. A beam booster incorporated in the column to maintain beam energy in the 10 kV range throughout the full length of the column, even if much lower probe energies are selected. The column is coated with Mu metal to ensure the environment in the column is magnetically clean. The conical geometry of the lens facilitates tilting of

the sample even at small working distance. At the end of the column, the energy of the electron beam is reduced to desired values.

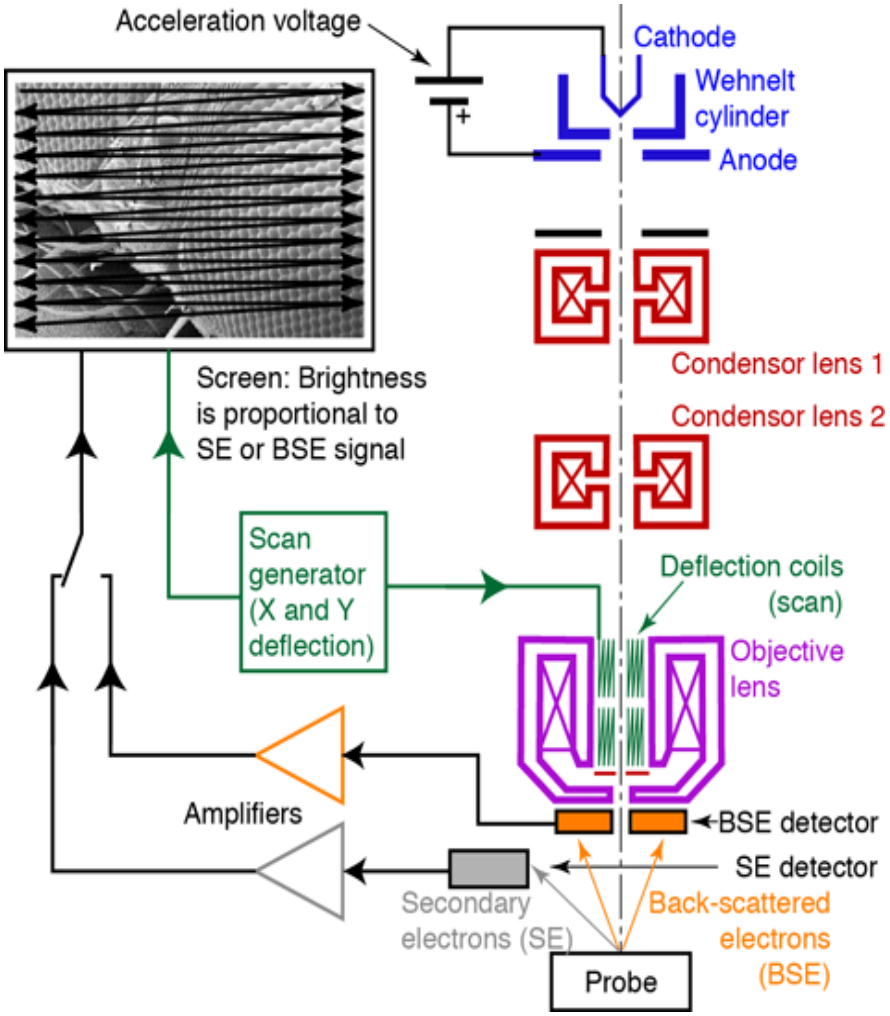

Figure 2.5 *Cross section of GEMINI column employed in the FESEM.*

The detectors are specifically designed to specialize in and detect one or more types of signals. The FE-SEM is equipped with two Everhart-Thorley type detectors. The lower detector is positioned horizontally near the specimen and collects all types of SE signals and some BSE signals providing a good view of topography. The upper detector is positioned above the specimen within the objective lens, offering through the lens collection. It also has the ability to detect signals at all working distances. The specimen itself is surrounded by a field causing the electrons to spiral upwards. Additionally, the objective lens is an inverted snorkel lens, creating an immersion lens field which also attracts the signal electrons. Either detector can be selected for imaging or both can be used in synchronously. The ion (or ion-getter) pumps are used to evacuate the gun area of the column.

The grain size, morphology and distribution of grains can be estimated through the FESEM microstructure. Any secondary phase segregation can also be detected through micro-structural analysis. It has the advantages over SEM are Small spot size, High emission current density, Long life time of the tip and High resolution. The micro-structural analysis was carried on the disc shaped samples coated with palladium and gold. These samples were mounted on to the stub via carbon tape to study their surface features, morphology and texture using the FESEM. The grain size of the samples was determined using Image J-software.

X-ray signals may be collected using either a crystal-based detector known as the Wavelength Dispersive Spectrometer (WDS) or a semi-conductor based detector known as an Energy Dispersive Spectrometer (EDS) or Energy Dispersive X-ray Analysis (EDAX). The EDS detector has a shaft that penetrates the SEM chamber wall to place the sensor very close to the sample. EDAX provides both quantitatively and qualitatively elemental analysis of a given sample. In this process, high energy electron beam is allowed to incident on the specimen which emits X-rays having energies specific to the elements present in the sample. These X-rays are made to impinge on detector crystal (Li (Si)) which generates the electric pluses depending on the energy of the X-rays incident on the crystal. Liquid nitrogen is used to reduce electronic noise in the detected X-ray signal. It senses the entire spectrum of X-ray signals of varying energy from the sample at once. But EDS is not sensitive enough to detect trace amounts of elements in the sample. Another disadvantage of EDS systems is that they cannot separate closely spaced emission lines which overlap on the X-ray EDS spectrum. Using WDS the data is collected sequentially for the full wavelength range and it is very sensitive and can take large count rates [9-10].

2.4 Transmission Electron Microscope

Transmission Electron Microscope (TEM) is an instrument used to do structural analysis of thin specimens. In TEM a thin specimen be illuminated by a broad beam of e^- having uniform intensity of light over the area of illumination on the sample. The electrons are one type of ionizing radiation, it produces a wide range of secondary signals from the specimen. It will often refer to incident and scattered electrons as beam of electrons, because hereafter dealing with a bunch of electrons not an individual electron. These electrons which are confined to well-defined paths in the microscope. So that the electrons are called incident beam and those scattered by sample are called scattered beam.

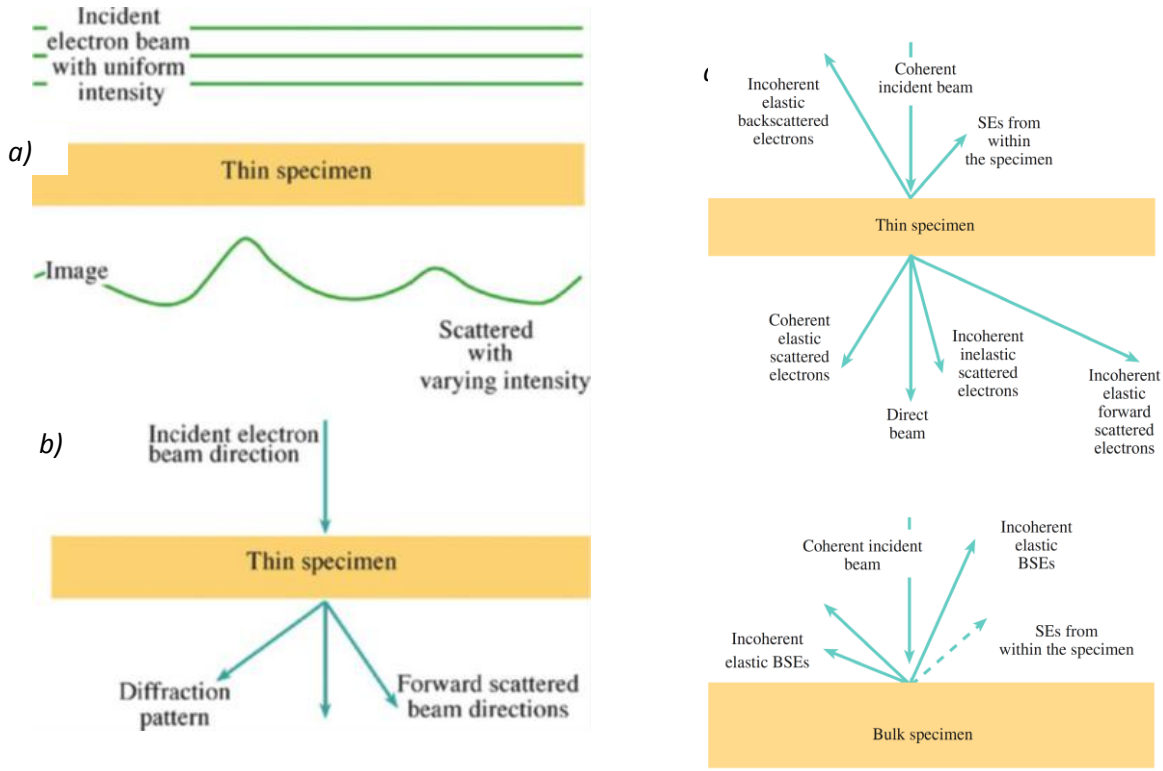

Figure 2.6 *a) Scattering of uniform intensity electrons with the specimen changes both the spatial and angular distributions, b) The change in angular distribution, Electron Scattering from c) a thin specimen and d) a bulk specimen.*

The e^- beam passing through a specimen without any angular deviation is called the direct beam. As the electrons travel through the specimen they are either scattered by a variety of processes or they may remain unaffected. The non-uniform distribution of electrons emerges from the exit surface of the specimen, as shown in figure 2.6. This non-uniform distribution of e^- contains all the structural and chemical information of the specimen. So everything learn about the specimen through TEM can be attributed to a form of electron scattering. This non-uniform distribution of electrons will be displayed in TEM in two ways. First one is the spatial distribution of scattering as shown in figure 2.6(*a*) can be observed as contrast in images of the specimen, and the second one is angular distribution of electron scattering as shown in figure 2.6(*b*) can be viewed in the form of scattering pattern called diffraction pattern. A simple operational step in the TEM is to use a restricting aperture or electron detector of a size such that it only selects electrons that have suffered more or less than a certain angular deviation.

The electron-scattering phenomenon can be classified in different ways. The scattering due to no loss of energy called elastic scattering also called coherently scattered electrons, if there is a loss of energy is called inelastic scattering also called incoherently

scattered electrons. The nature of the scattering can result in different angular distributions. Scattering can be either forward or backward scattering refer to the angle of scattering with respect to the incident beam and a specimen normal to that beam. If an electron is scattered through less than 90^o is called forward scattering and greater than 90^o is called backward scattering. These various types of electron scattering by the general principles is summarized in figure 2.6.

Diffraction is a very special form of elastic scattering defines as a deviation in the direction of a wave at the edge of an obstacle in its path, whereas scattering is defined as the process in which particles, atoms are defected as a result of collision. So scattering might best apply to particles and diffraction to waves.

The objective lens and stage combination is the heart of the TEM. The stage is used to clamp the sample holder in the correct position so the objective lens can form images and diffraction patterns in a reproducible manner as shown in figure 2.7. The TEM can be operated in two modes which are diffraction mode (DP) and image mode. In the diffraction mode adjust the imaging system lenses so that the back-focal plane of the objective lens acts as the object plane for the intermediate lens. Then it is projected onto the viewing screen or CCD as shown in figure 2.7(*a*). In the image mode adjust the intermediate lens so that its object plane is the image plane of the objective lens. Then as image is projected onto the screen/CCD as shown in figure 2.7(*b*). The DP contains electrons form the whole area of the specimen that illuminate with the beam. Such pattern is not very useful because specimen will often be buckled. Furthermore, the direct beam is often so intense that it will damage the direct the viewing screen or saturate CCD camera. So, a basic TEM operation which both selects a specific area of the specimen and reduce the intensity of the direct beam.

The first option involves using *C2* and/or *C1* to converge the beam at the specimen. This approach is used to form convergent beam electron diffraction (CBED) patterns. Converging the beam destroys any parallelism, and spots in the pattern are not sharply defined but spread into disks. To obtain a DP with a parallel beam of electrons, the standard way is to use the selected area aperture. It is not possible to insert an aperture at the specimen plane, so an aperture is inserted in a plane conjugate with the specimen, then it creates a virtual aperture at the plane of the specimen is called selected area diffraction or SAD is shown in figure 2.7(a).

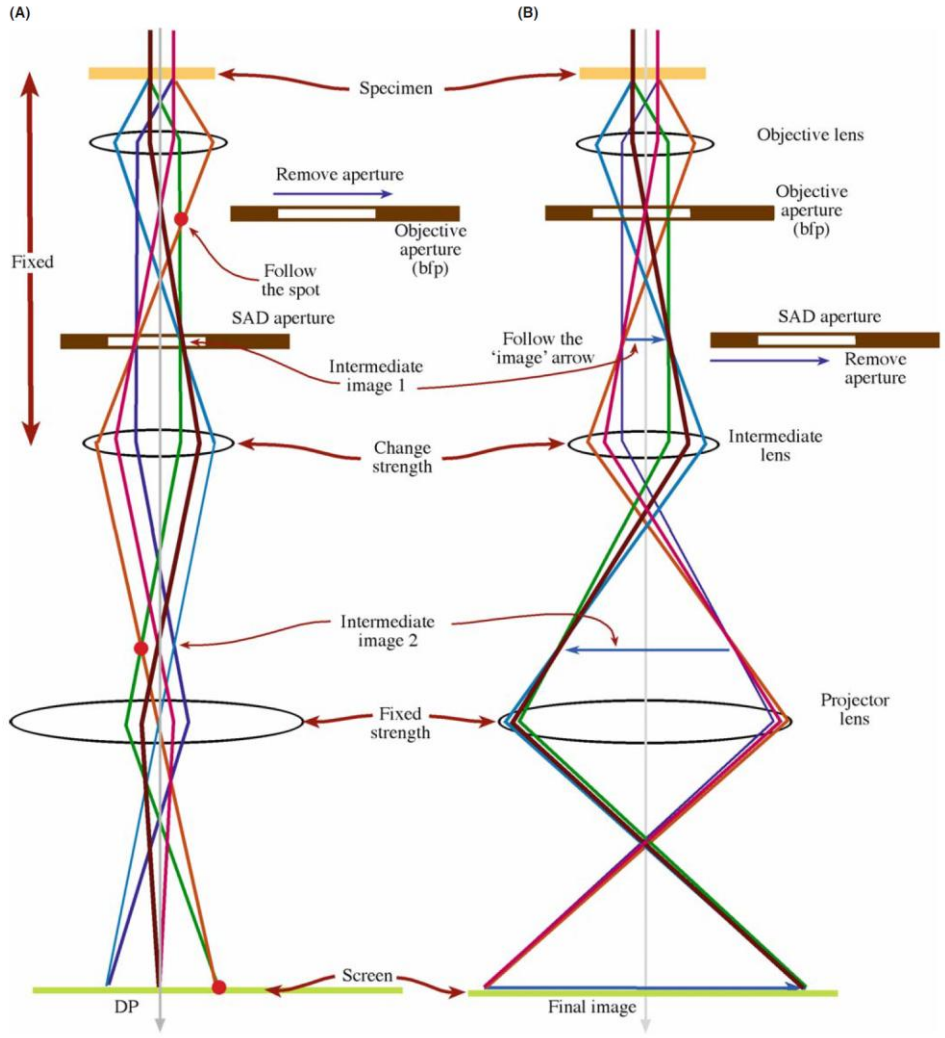

Figure 2.7 *The two basic operations of the TEM imaging system a) Diffraction mode, b) Image mode*

The TEM should be calibrated when it is first installed and then periodically throughout its life, especially to carry out accurate measurements from the images and diffraction patterns. Thus, TEM have the ability to obtain diffraction pattern from specimen under observations. This diffraction pattern provides structural details related to the specimen orientation, poly type, phase, defects morphology and so on [11-13].

2.5 Vibrating sample magnetometer

Vibrating sample magnetometer (VSM) is an instrument used to measure the magnetization of materials, the schematic of the VSM is shown in figure 2.8. It works on the principle of Faradays laws of induction- a change in magnetic field produces an electric field and this electric field is used to measure the magnetization of the sample. The magnetic properties of SnO_2/CZF ML were studied using lake shore (7400) VSM [14].

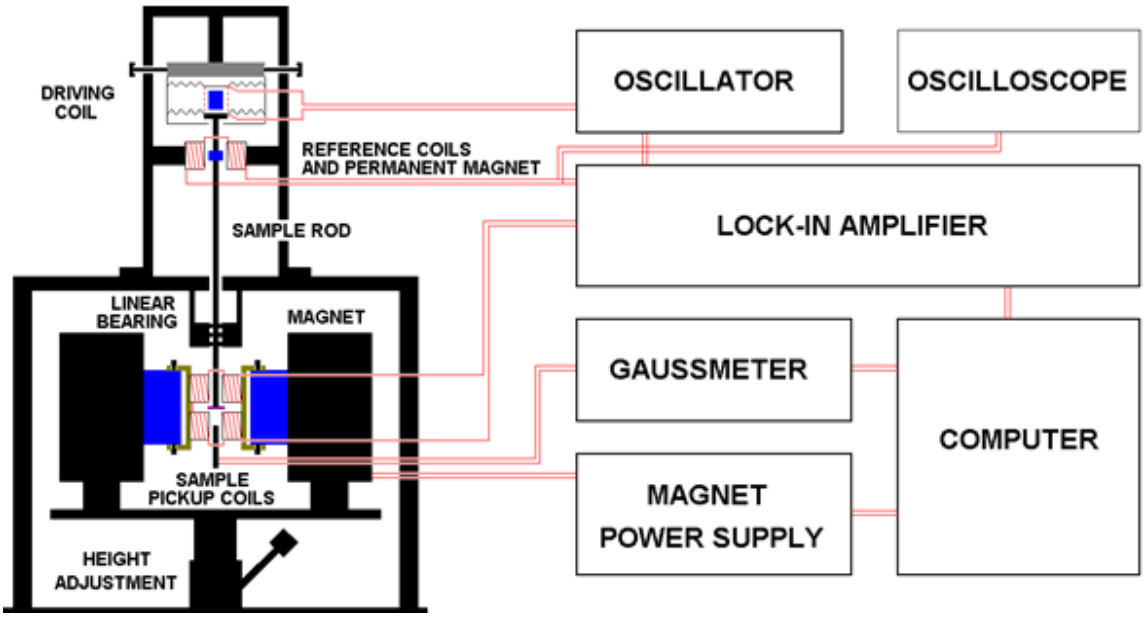

Figure 2.8 *Vibrating sample magnetometer – block diagram.*

The sample holder consists of a long rod made of a non-magnetic material. The sample to be studied is placed at the tip of the sample holder and is placed in a constant magnetic field generated by a pair of electromagnets. If the sample is magnetic, this constant magnetic field will magnetize the sample by aligning the magnetic domains, or the individual magnetic spins, with the field. A dipole moment equal to the product of sample susceptibility and applied field is induced in the sample. The sample holder is attached to a vibrating head which enforces the sample to vibrate in a sinusoidal fashion in the magnetic field. The magnetic stray field due to the dipole moment of the sample changes as sample vibrates and the change in magnetic stray field as a function of time is sensed by a set of pick-up coils. The alternating magnetic field causes an electric current in the pick-up coils according to Faraday's Law of Induction. The induction voltage caused across the coil is given by [15]

$$V(t) = C\frac{d\phi}{dt} \tag{2.4}$$

where, $\varphi(t)$ represents the changing flux in the pickup coils. The generated current is proportional to the magnetization of the sample. The greater the magnetization, larger is the induced current. The induction current is amplified by a transimpedance amplifier and lock-in amplifier. The various components of the VSM are interfaced with a computer. Using controlling and monitoring software, the system can give the extent to which the sample is magnetized and how its magnetization depends on the strength of the constant

magnetic field. The frequency and amplitude of the sinusoidal motion are held constant, which is controlled by a capacitor (reference signal generator). By feeding the signals from the pick-up coils and the reference signal into a demodulator, the magnetic moment of the sample is extracted [16].

In the materials, existence of strong *AB* exchange interactions among the cations is responsible for anti-parallel alignment of spins at *A* and *B* sites with certain resultant magnetic moment ($n_B=M_A-M_B$).The magnetic parameters obtained from the hysteresis loops are magnetisation, coercivity and remnant magnetisation. The specific saturation magnetisation defined as magnetic moment per unit mass (emu/g) is

$$\sigma_s = \frac{Magneticmoment}{mass} emu/g \tag{2.5}$$

The relation between saturation magnetisation and specific saturation magnetisation is

$$M_s = \frac{\sigma_s}{d} emu/cm^3 \tag{2.6}$$

Where d is the density of the material (g/cm^3).

Magnetic moment of the sample can be determined using the relation

$$n_B = \frac{\sigma_s * MW}{5585} Bohr\ magneton \tag{2.7}$$

Where MW is molecular weight of the compound. The Magneto-crystalline anisotropy constant (K_1) can be determined using magnetisation and coercivity [17]

$$K_1 = \frac{H_c * M_s}{0.96} \tag{2.8}$$

A plot of magnetisation versus temperature at a fixed field is known as thermo grams. The plot indicates gradual decrease of magnetisation with temperature and at one particular temperature; magnetisation tends to become zero known as Curie temperature (T_c). Thus, Curie temperature gives an idea about the amount of thermal energy required to disrupt the exchange interactions among the ions.

An important process in the measuring the samples magnetization is saddling of the sample. If the sample is not placed exactly at the centre between the pole pieces, to determine the magnetic moment accurately. This process of aligning a sample is called saddling. It is done by moving the sample on all the three axes and finding the point at which the sample gives maximum magnetic moment. The system is initially calibrated using a standard Ni sample and saddling it. The sensitivity of VSM manufactured by Lake Shore is in the range of 10^{-6} emu.

2.6 Resistivity measurement

The temperature dependent resistance of the samples was measured by the four-probe method using a closed cycle refrigerator (CCR) fitted with a Lakeshore 330 temperature controller.

The closed cycle refrigerator APD DE202 is a two-stage cryogenic refrigerator that operates in the Gifford-McMahon refrigerator cycle [18]. It uses helium gas from a helium compressor to produce the cold temperatures. In this type of refrigerators, the compressor unit is separated from the cold head and connected via flexible or rigid pressure tubings. Connection is made via self-sealing screw-couplings, virtually excluding any loss of helium gas even when screwed on and off repeatedly. The refrigerators can be used to cool cryo-pumps or to cool samples in cryostats. The great advantage of the Gifford-McMahon principle is that compressor unit and cold head (expansion unit) are separated. This provides higher flexibility as the lighter weight cold head can be operated in any mounting position. Other important aspects of CCR system are PID parameters, temperature sensors and temperature controller. The PID parameters vary depending on the setup of each type of CCR. There are only two types of standard sensors used in the CCR system. The first, silicon diode, is the most common and is used for low temperature measurements. The second, platinum resistor is used for high temperature measurements. A Lakeshore 330 temperature controller was used in the present measurements. The major components of the closed cycle cryostat are the expander, compressor, vacuum shroud, and radiation shield as described in figure 2.9.

The expander, commonly referred to as the cold-head or cold finger, is where the Gifford-McMahon refrigeration cycle takes pace. It is connected to a compressor by two gas lines and an electrical power cable. One of the gas lines supplies high pressure helium gas to the expander, the other gas line returns low pressure helium gas from the expander.

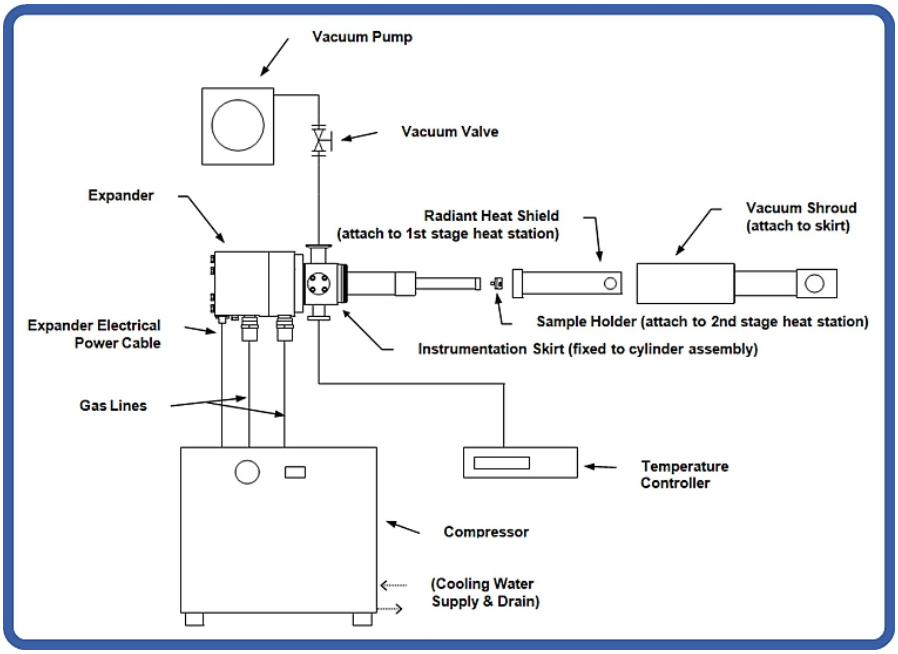

Figure 2.9.Schematic diagram of a closed cycle refrigerator

The compressor provides the necessary helium gas flow rate at the high and low pressure for the expander to convert into the desired refrigeration capacity. The vacuum shroud surrounds the cold end of the expander in vacuum limiting the heat load on the expander caused by conduction and convection. The radiation shield is actively cooled by the first stage of the expander and insulates the second stage from room temperature thermal radiation being emitted from the vacuum shroud.

In addition to these major components the closed cycle cryocooler is often accompanied by several support systems. Typically, laboratory systems will have an instrumentation skirt, which provides a vacuum port and electrical feed through, as well as a temperature controller to measure and adjust the sample temperature. The system also requires electricity, cooling water for the compressor, and a vacuum pump for the sample space.

Much may be learned about the properties of a material by measuring its resistivity. An important example is the characterization of semiconductor materials where the resistivity is strongly related to the level of purposely added impurities. Measurement of the resistivity is used to both characterize the material and as a process control parameter for the semiconductor manufacturing process. The resistivity of the material can be measured by using either two probes or four probes method. With the two probes method, current and voltage are measured in the same connector wires. So, the measured voltage is

added with the potential difference created into the wires (cause of Ohm's law: V=RI). For high resistivity (from 1M ohm/sq), this method can be used because contact resistance is negligible. For low resistivity measurement, this method will be not accurate because contact resistance will be very close to sample resistance. For low resistivity measurements, the best method is the four probe method [19–22]. In this method, current is sent in two probes and voltage is measured by two other probes as shown figure 2.10. So, the measured voltage is really that circulate into the sample with no current. There is no potential difference into the wires and contact. The four probe method is employed for measuring the resistivity of the samples in the present work.

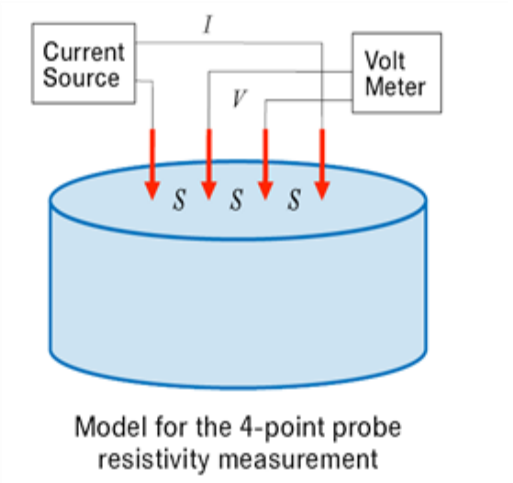

Figure 2.10. Schematic of four-point probe

The four point contacts with equal spacing were made on the rectangular shape pellets using silver paste. Electrical current varying from 1μA to 1mA was passed between two of the probes by using Keithley D.C and A.C. current source (model 6221). The voltage created is measured between other two probes using a Lakeshore (model 332) temperature controller. The D.C. resistivity of the sample is calculated by the relation

$$R = V/I = \rho L/A \tag{2.9}$$

$$\text{Therefore, Resistivity } (\rho) = VA/IL \tag{2.10}$$

Where, R = Resistance of the sample, V = Voltage measured across the terminals, I = Current passed between the terminals, A = Area of cross section of the sample and L = length between the voltage terminals.

References

[1]. Suk-Joong L.Kang, *Elsevier Publisher*, Burlington-MA (2005).

[2]. R.Singh and E.Zacharias, *J.Phys.D.Appl.Phys*., **23**, 199-204 (1990).

[3]. E.Zacharias and R.Singh, *Physica C*, **247**, 221-230 (1995).

[4]. B. D. Culity, *Addison-Wesely Publishing Company Inc.* (1978).

[5]. B. E. Warren, *Dover Publications*, New York (1990).

[6]. C. Suryanarayana and M. Grant Norton, *Springer Publisher*, New York (1998).

[7]. S. M. Patange, S. E. Shirsath, G. S. Jangam, K. S. Lohar, S. S. Jadhav, and K. M. Jadhav, *Journal of Applied Physics*, **109**, 5, 053909 (2011).

[8]. J. I. Goldstein, D. E. Newbury, *Kluwer Academic/Plenum Publishers*, 3rd Edition, (2003).

[9]. Patrick Echlin, 1st Edition, *Springer Publisher*, USA (2009).

[10]. David G. Rickerby, Giovanni Valdre and Ugo Valdre, 1st Edition, *Kluwer Academic Publishers*, Italy (1999)

[11]. David B. Williams and C. Barry Carter, *Springer Publishing* (2009).

[12]. M. A. Hayat, *Academic Press*, USA (1986).

[13]. J. S. J. Pennycook, P. D. Nellist, *Springer Publisher*, USA (2011).

[14]. Roland Grössinger, *Journal of Electrical Engineering*, **59**, 7, 15-20 (2008).

[15]. A. W. Pacyna and K. Ruebenbaur, *J. Phys. E*, **17**, 141 (1984).

[16]. Xiaonong Xu, Aimin Sun, Xin Jin, Hongchang Fan and Xixian Yao, *Rev Sci. Instruments*. **67**, 3914 (1996).

[17]. P.A. Shaikh, R.C. Kambale, A.V. Rao, Y.D. Kolekar, *J. Alloys Compd*., **492**, 590–596 (2010).

[18]. W.H. Higa and E. Wiebe, *National bureau of Standards Technical Publication*, **508**, 99 (1978).

[19]. J. R. Ehrstein and M. C. Croarkin. *National Technical Information Services Special Publication*, **260-131** (1997).

[20]. Standard Test Method for Measuring Resistivity on Silicon Wafers with an In-Line Four-Point Probe ASTM Standard, **F 4-99**.

[21]. Standard Test Methods for Conductivity Type of Extrinsic Semiconducting Materials ASTM Standard, **F 42-93**.

[22]. Standard Test Method for Sheet Resistance of Thin Metallic Films with a Collinear 4 Probe-Array ASTM Standard **F 390–78**.

CHAPTER 3

Synthesis and Properties of Bismuth Oxy-Sulphide Superconductors

3.1 Introduction

In this chapter, we present the synthesis of Bismuth Oxy Sulphide samples with excess Bi_2O_3 and with excess Bi, S over and above the required quantity as per stoichiometric composition of $Bi_4O_4S_3$ phase. And discussed about pinning mechanism in $Bi_4O_4S_3$.

New layered $Bi_4O_4S_3$ superconductor with superconducting transition at 4.4K provides a new challenge to researchers to raise the T_c (transition temperature) by varying the spacer layer or alignment of superconducting and spacer layers. In general, $Bi_4O_4S_3$ structure is composed of two spacer layers that are Bi_2O_2 and SO_4 with one superconducting BiS_2 layer. The band structure of $Bi_4O_4S_3$ reveals that the most dominating band is the resultant of the hybridization of Bi *6p* and S *3p* orbitals. The Fermi level is located at the center of the density of states such that it shows the metallic behaviour at room temperature [1]. The bulk superconducting nature has been proven by several groups and concluded that exclusion of Bi and Bi_2S_3 impurities in these materials is not possible at ambient conditions [2-3]. The electron pairing occurs first in one dimensional chain and then establishes bulk superconductivity through Josephson coupling between them due to shallow band edge of P_x and P_y orbitals of Bi. The application of magnetic field makes the density of states of the spin-up and spin-down electrons asymmetric due to the Zeeman effect and these polarized electrons induce weak insulating behaviour in $Bi_4O_4S_3$ in normal state below 25K [4]. Strong electron phonon coupling in $Bi_4O_4S_3$ has been revealed by the best fit of super fluid density with single gap S-wave equation [5], whereas multiple gap existence was revealed by micro-spin rotation and relaxation measurements [6] and Scanning tunnelling experiments [7]. The effect of hydrostatic pressure shows that as pressure increases, the superconducting transition temperature, T_c decreases [8-9]. The studies have confirmed that

$Bi_4O_4S_3$ is a Type-2 superconductor with lower critical field, H_{c1}~7Oe, upper critical field, H_{c2}~31KOe and coherence length of, ξ~100A^0 [3, 10].

In this chapter, in section 3.3.1, we present the effect of 5% and 10% of excess Bi_2O_3 on synthesis and properties of Bismuth Oxy Sulphide samples. In section 3.3.2, we presented the comparative results of stoichiometric sample and $Bi_4O_4S_3$ synthesized with 10% of excess Bi and S. There are no reports on the magnetic critical current density (J_c) measurements on these materials. Such measurements are essential to understand the vortex pinning mechanisms which are responsible for controlling J_c. The present work has helped in understanding the dominant pinning mechanisms in these materials.

3.2 Experimental Techniques

The polycrystalline $Bi_4O_4S_3$ samples were prepared using conventional solid state reaction method. In this method pure Bi_2O_3 powder, Bismuth metal granules and Sulphur flakes (all from sigma Aldrich with purity>99.99%) were mixed in stoichiometric ratio and ground for 1 hour using an agate mortar. The mixture was used to make pellets using a hydraulic press at ambient conditions. The pellet samples were sealed in a quartz tube under the vacuum of $5x10^{-4}$Torr and sintered at 510^oC for 18 hours followed by furnace cooling. The same procedure was repeated twice to get better homogeneity. The sample obtained is named as BiOS-1 here onwards in this chapter. The samples with 5% and 10% of excess Bi_2O_3 above the stoichiometric ratio were also prepared by same method and named as BiOS-2 and BiOS-3 respectively. Sample with 10% of excess Bi and S in addition to the stoichiometric ratio were prepared through solid state reaction method and named as BiOS-4 in the series.

The X-ray diffraction (XRD) patterns of the samples were recorded using powder X-ray diffractometer (Bruker) with Cu-k_α radiation. The assignment of peaks and lattice parameters estimation was done by using FullProf software. The layer structure of the synthesized samples is confirmed by transmission electron microscopic (TEM) studies. The surface morphology, grain size distribution and composition were analyzed using field emission scanning electron microscopy (FESEM) and energy dispersive spectroscopy (EDS). The temperature dependent electrical resistivity of the samples was measured by four probe method using a closed cycle refrigerator. The AC susceptibility and *M-H* loops were recorded on rectangular samples with dimensions of (4.4×2.7×0.6)$mm^{3,}$

$(3.4\times2.6\times0.6)mm^3$ and $(8.6\times3.3\times1.5)mm^3$ for BiOS-1, BiOS-2 and BiOS-3 respectively, using physical property measurement system (PPMS Quantum design).

3.3 Results and Discussion

3.3.1 Effect of excess Bi_2O_3 on the synthesis of $Bi_4O_4S_3$

3.3.1.1 Structure and Morphology

The XRD pattern for the synthesized polycrystalline BiOS-1 sample is shown in figure 3.1(*a*).

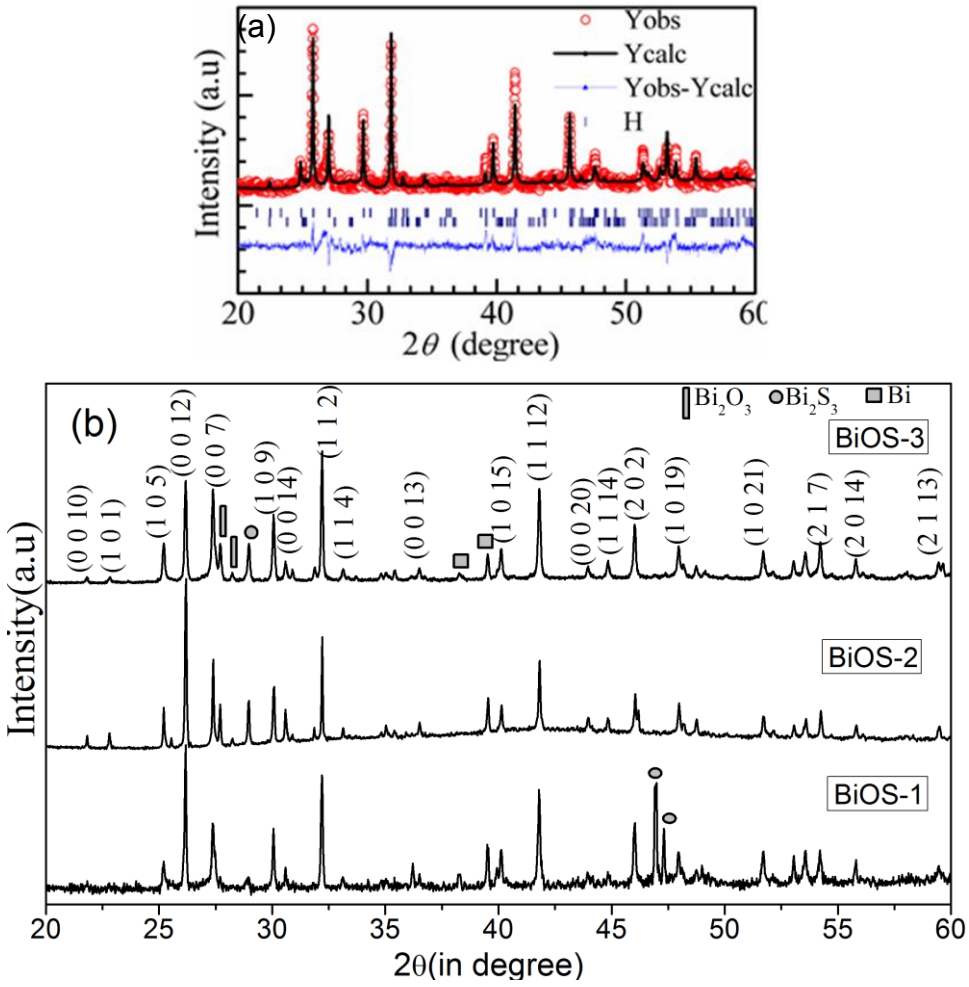

Figure 3.1 *(a) Refined spectra of BiOS-1 sample (b) shows comparative normalized XRD pattern for the BiOS-1, BiOS-2 and BiOS-3 samples.*

Refinement of the data was done using FullProf software and the lattice parameters obtained are a=3.9703A^0, c=41.3984A^0, which are in good agreement with the reported values [1, 3, 9]. Figure 3.1(b) shows the comparative normalized XRD pattern for the three samples. The lattice parameters obtained for BiOS-2 and BiOS-3 are a=3.9657A^0,

c=41.3156A^0 and a=3.9691A^0, c=41.3489A^0 respectively. All the samples show $Bi_4O_4S_3$ phase along with Bi, Bi_2S_3, and Bi_2O_3 impurity phases. It is observed that the intensity of peaks corresponding to $Bi_4O_4S_3$ phase and impurity phases increased with excess Bi_2O_3.

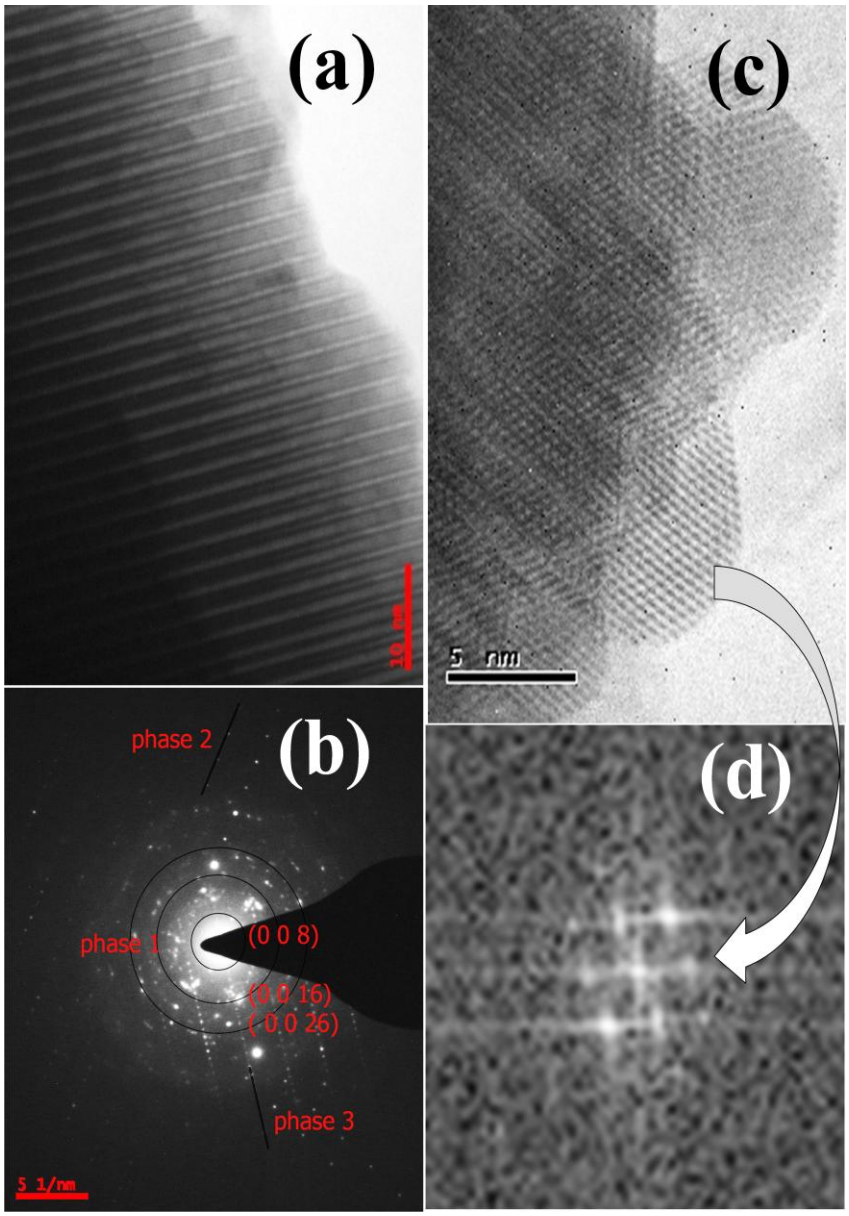

Figure 3.2 *(a) TEM image (b) SAED pattern (c) HRTEM image and (d) FFT image for BiOS-2 sample.*

The TEM images for BiOS-2 sample shown in figure 3.2 clearly indicate stacking of SO_4 layer as interfacing layer between Bi_2O_2 and BiS_2 layers and no stacking faults are observed. From the selected area electron diffraction pattern (SAED) (figure 3.2(*b*)) two impurity phases along with $Bi_4O_4S_3$ phase are clearly observed. The ring pattern confirms the polycrystalline phase of $Bi_4O_4S_3$ (phase1), whereas diffraction pattern oriented in single direction (phase 2 and phase 3) are identified as Bi and Bi_2S_3 metal impurities. From figure

3.2(*c*), defects like; dislocations, twin boundaries are observed. From figure 3.2(*d*), crystal planes are identified corresponding to $Bi_4O_4S_3$ phase. The lattice parameter values calculated using SAED pattern, are in good agreement with the refined values from XRD pattern using FullProf.

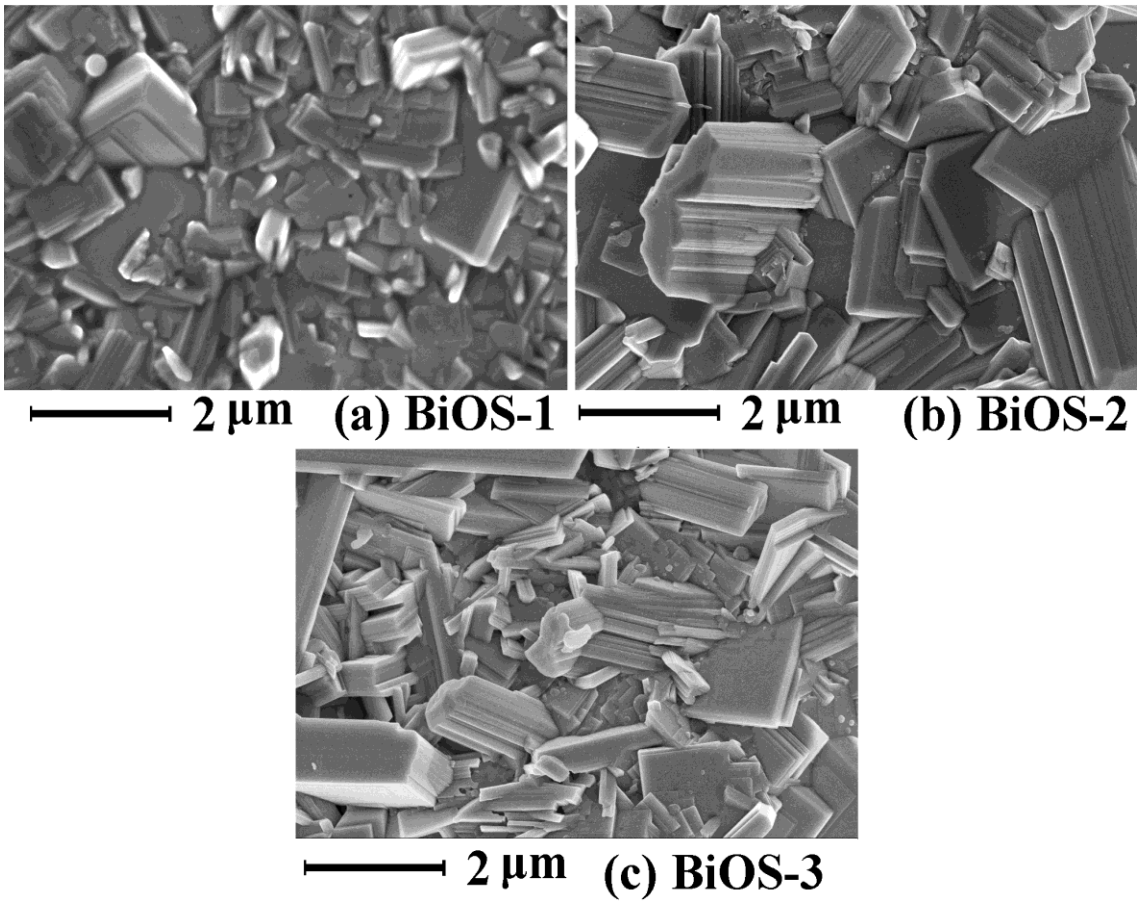

Figure 3.3 *FESEM images for the samples.*

Figure 3.3 shows FESEM micrographs for the synthesized samples. The images show platelet like structure confirming the two dimensional layered structure of $Bi_4O_4S_3$. The average grain size is calculated using image j software and the values are found to be 545nm, 977nm, and 745nm for BiOS-1, BiOS-2 and BiOS-3 samples respectively.

The elemental analysis of the samples (figure 3.4) confirmed that the grains have composition close to stoichiometric ratio. Off stoichiometry in $Bi_4O_4S_3$ is explained by Adam et al [11] by pointing out that $Bi_4O_4S_3$ is a mixed phase of two non-sulphate phases, Bi_2OS_2 which is non superconducting and can act as stacking faults in Bi-O-S system and the other one $Bi_3O_2S_3$, which is superconducting at 4.5K. It is also pointed out that the superconducting volume fraction decreases with increase in stacking faults in $Bi_3O_2S_3$ [11].

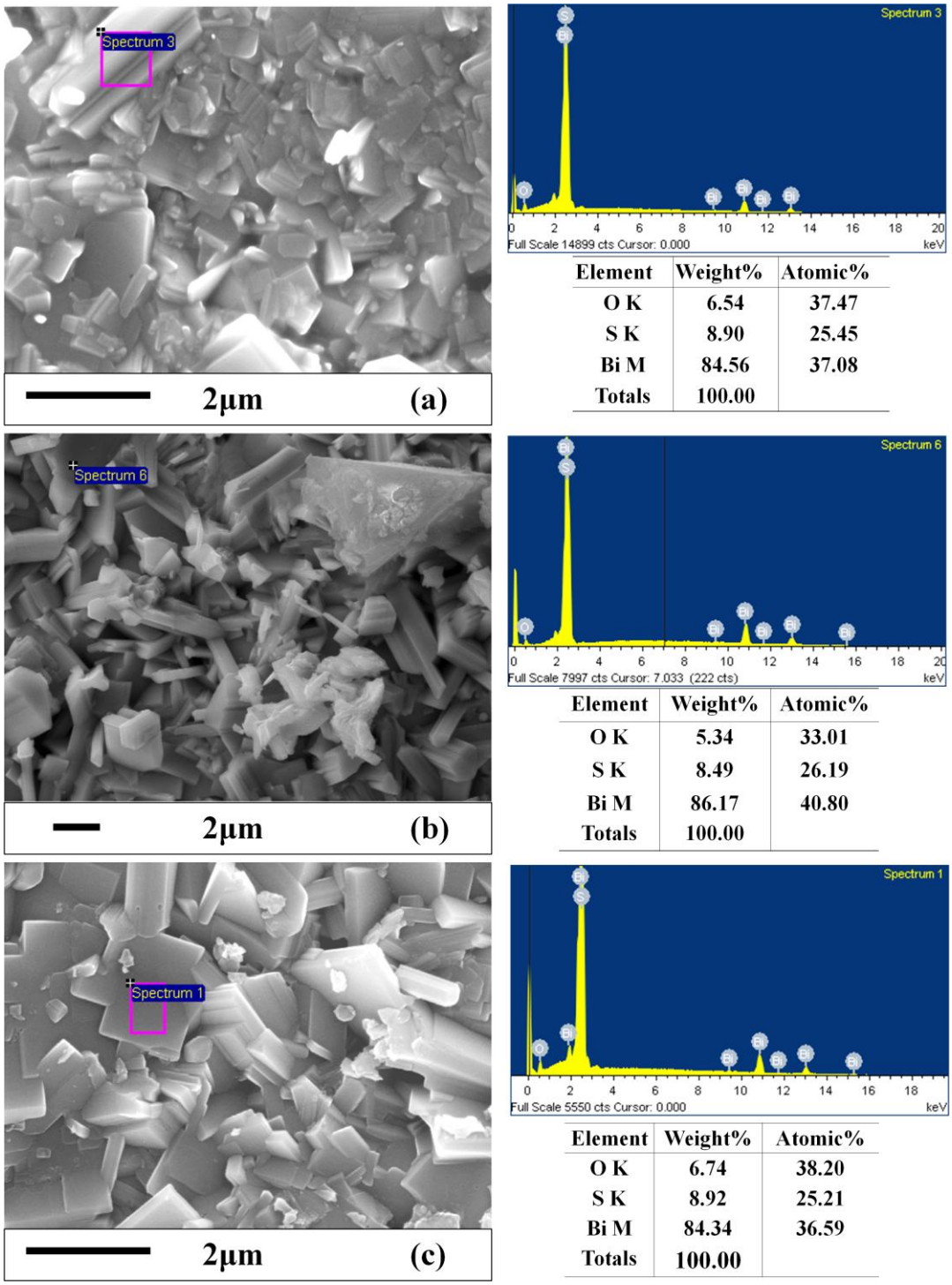

Element	Weight%	Atomic%
O K	6.54	37.47
S K	8.90	25.45
Bi M	84.56	37.08
Totals	100.00	

Element	Weight%	Atomic%
O K	5.34	33.01
S K	8.49	26.19
Bi M	86.17	40.80
Totals	100.00	

Element	Weight%	Atomic%
O K	6.74	38.20
S K	8.92	25.21
Bi M	84.34	36.59
Totals	100.00	

Figure 3.4 *EDS spectra of (a) BiOS-1 (b) BiOS-2 (c) BiOS-3.*

3.3.1.2 Transport Properties

Figure 3.5 shows temperature dependent resistivity of the synthesized samples. From this graph, the room temperature resistivity, superconducting transition onset temperature and residual resistivity ratio (RRR) variation with composition are calculated and listed in table 3.1. All the samples show metallic nature down to 25K suggesting

electron-phonon interactions in the system. Below 25K the data shows very weak insulating behaviour for all the samples. These results are in good agreement with earlier reports [12]. Sheng Li has reported magnetic field induced insulating behaviour below 25K due to the competing order between insulating and superconducting phases of $Bi_4O_4S_3$ [5]. The T_c onset was taken as the temperature at which resistivity decreases by 10% of the lowest value in the normal state.

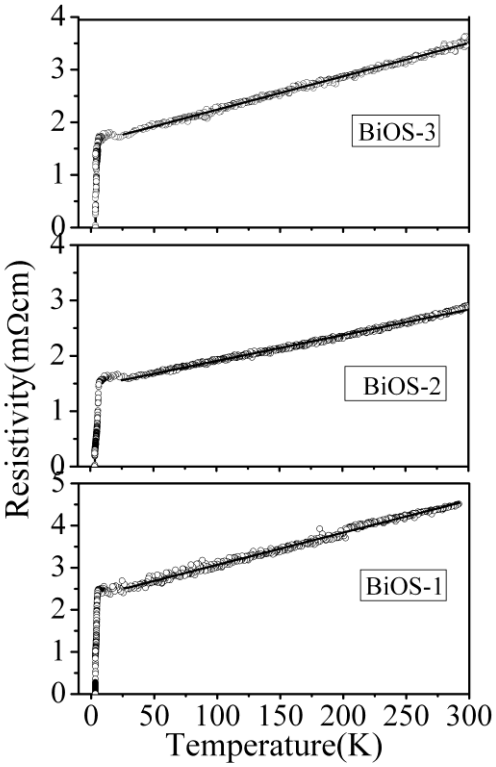

Figure 3.5 Resistivity vs. temperature plots for the BiOS-1, BiOS-2 and BiOS-3 samples. Solid line is the linear fit to the data points.

Table 3.1 *Transport parameters estimated from resistivity data.*

Sample	T_{onset} (± 0.5K)	T_{zero} (± 0.1K)	ΔT (K)	AC Susceptibility T_{onset} (± 0.05K)	ρ_{rt} (mΩ.cm)	ρ_0 (mΩ.cm)	RRR	Metallicity (μΩ.cm/K)
BiOS-1	4.9	3.3	1.2	4.0	4.5	2.3	1.96	7.64
BiOS-2	6.4	3.5	3.2	4.3	2.9	1.5	1.93	4.65
BiOS-3	5.6	3.5	3.9	4.5	3.6	1.7	2.12	6.34

It is observed that the T_c onset and transition width increases with excess Bi_2O_3. In the granular superconducting samples the global superconductivity is achieved when the superconducting grains get progressively coupled to each other by Josephson tunnelling across the grain boundary weak links [13]. The large grain size in BiOS-2 sample reduces the grain boundaries which help in superconducting grain to couple at higher temperature to reach global superconductivity. This results in high T_{onset} in this sample. The increase in transition width may be due to random orientation of the superconducting grains. The residual resistivity decreases with excess Bi_2O_3 suggesting that the purity of the samples increases with excess Bi_2O_3. This may be due to the increase in grain size and homogeneity in the sample and decrease in the defect concentration like grain boundaries.

3.3.1.3 Magnetization Studies

Figure 3.6 shows real (χ') and imaginary (χ'') AC susceptibility as a function of temperature for various samples under applied AC drive field of 10Oe. The studies on Cuprate superconductors have shown that the peak in χ'' is associated with the losses due to granular nature of the samples [14, 15]. In a single phase superconductor loss peak in χ'' can represent intrinsic losses due to the screening of magnetic fields by the superconducting surface currents. The loss is weakly dependent on temperature, magnetic field and frequency. The peak in χ'' in granular superconductor arises due to inter granular weak links or Josephson junction coupling of adjacent superconducting grains. The height and width of this peak is strongly dependent on grain size distribution, temperature, magnetic field, and DC magnetic field history of the sample. This peak behaves like critical current density (J_c) in polycrystalline superconductor.

When the applied field exceeds lower critical field H_{c1}, then the loss peak is due to de-pinning of Abrikosov vortices. This peak is called intra-granular peak and is explained by Bean or critical state models. The experimental data in figure 3.6 confirms the granular nature of the samples. Since the applied field is low i.e. 10Oe, the peak observed in χ'' is predominant due to inter-granular weak–link coupling of the grains. The intrinsic loss peak is not observed clearly. The relatively narrow peak compared to other sample, observed for BiOS-2 sample indicates a narrow distribution of grain size confirming SEM and transport data. The higher T_c observed for BiOS-3 sample may be due to stronger Josephson coupling between superconducting grains giving rise to higher H_{c1} as obtained from *MH* data.

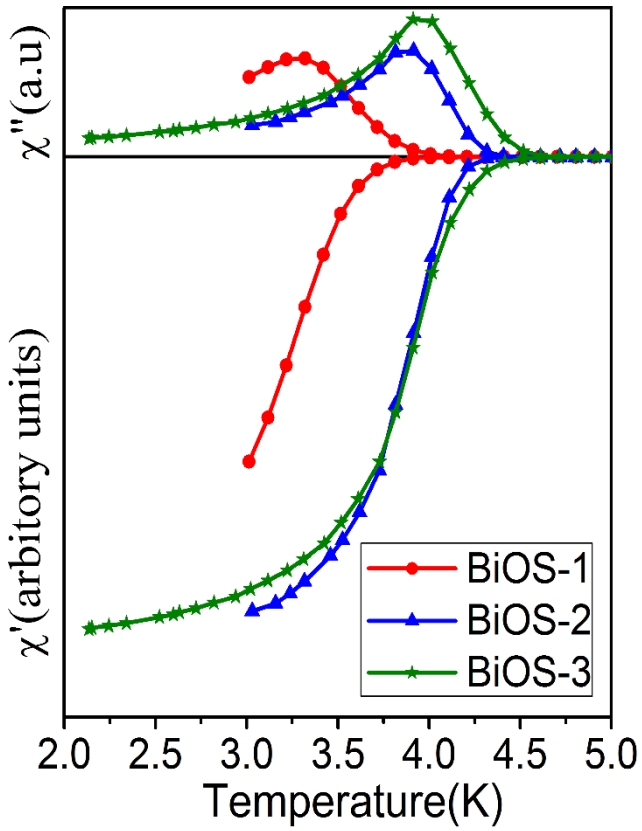

Figure 3.6 *AC susceptibility response with temperature for the BiOS-1, BiOS-2 and BiOS-3 samples with the applied ac field of 10Oe.*

Figure 3.7 shows isothermal magnetization versus magnetic field data at 2.5K. Irreversible nature of the MH curves represents type 2 superconductor nature of the sample with lower critical field (H_{c1}) of 16, 18 and 27Oe for BiOS-1, BiOS-2 and BiOS-3 respectively. Because of limited data points the error in these values may be quite significant. *M-H* loop for a clean and defect free type-2 superconductor is reversible and when the external field is switched off, no magnetic flux is trapped within the superconductor. *M(H)* curve becomes highly irreversible for superconductors containing defects or impurities, which interacts with penetrating flux lines. The loops reveal the irreversibility and remnants magnetization of the samples [16]. The low H_{c1} indicates that smaller Meissonier region and the magnetic induction in the bulk sample can be reached at low applied fields. Inter grain critical current density for the samples with rectangular slab shape is calculated from the irreversible *M-H* loops at 2.5K (figure 3.6) using extended Bean model [17] using following equation

$$J_c=20(\Delta M/d), \text{ here } d=b[1-(b/3a)], a>b \qquad (3.1)$$

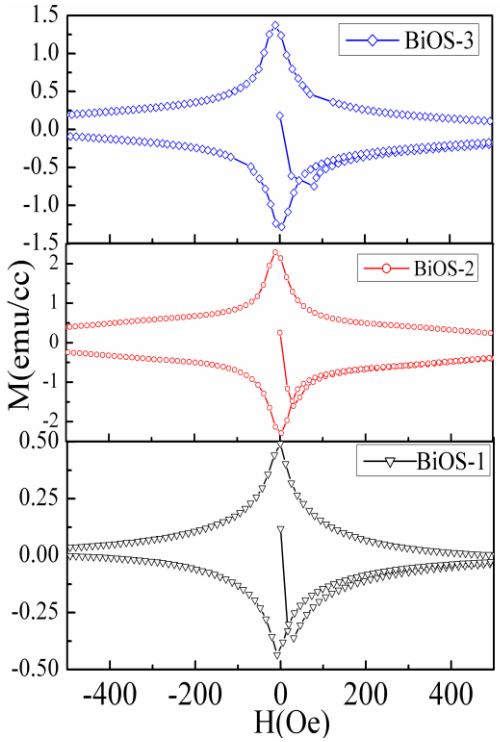

Figure 3.7 *Isothermal M-H plots of BiOS-1, BiOS-2 and BiOS-3 samples at T=2.5K.*

where, ΔM $(M^{+}\text{-}M^{-})$ is the width of the *M-H* loop and *a*, *b* are sample dimensions. Small hysteresis loop of the samples reveals the presence of weak flux pinning and/or weak inter granular coupling [18, 19]. This results in low value for J_c in these samples. Decrease in J_c with increase in field is due to the field induced pins (FIP). The FIPs might be the impurity phases present in the samples. For a bulk superconductor typical J_c behaviour is an exponential decrease with field due to inter-grain currents [18]. In all the samples, J_c decreases exponentially up to some field which is called as deviation field hereafter. Figure 3.8(a) shows the linear dependence of *log* (J_c) on applied magnetic field, up to the deviation field (region-1). In BiOS-1 sample after this deviation filed, J_c decays in another exponential path as shown in figure 3.8(b) (region-2). Exponent of the decay in region-1 is 4.73×10^{-3} whereas it has decreased to 2.42×10^{-3} in region-2, which means in region-2, J_c decreases at a slower rate when compared with region-1. For BiOS-2 and BiOS-3 samples beyond deviation field, J_c varies according to collective pinning model [20]. According to this model, above the crossover field, which is defined as the separating field of single vortex and small bundle, J_c decays according to the following equation

$$J_c(H) = J_c(0) \exp\left[-(H/H_0)^{3/2}\right], \qquad (3.2)$$

where, $J_c(0)$ is critical current density at zero field and H_0 is the normalization field. Figure 3.8*(c)* and *(d)* show that for BiOS-2 and BiOS-3 samples log J_c varies linearly with $H^{3/2}$.

The slope and intercept of this plot gives normalization field (H_0) and maximum current density $J_c(0)$ at the deviation field respectively. The double exponential decay of J_c indicates the existence of new pinning mechanism in the samples. Magnetic flux motion has to be prevented by flux pinning, which represents the strength of pinning force F_p. As long as the flux lines are pinned, the maximum density of super current flows without any loss [21].

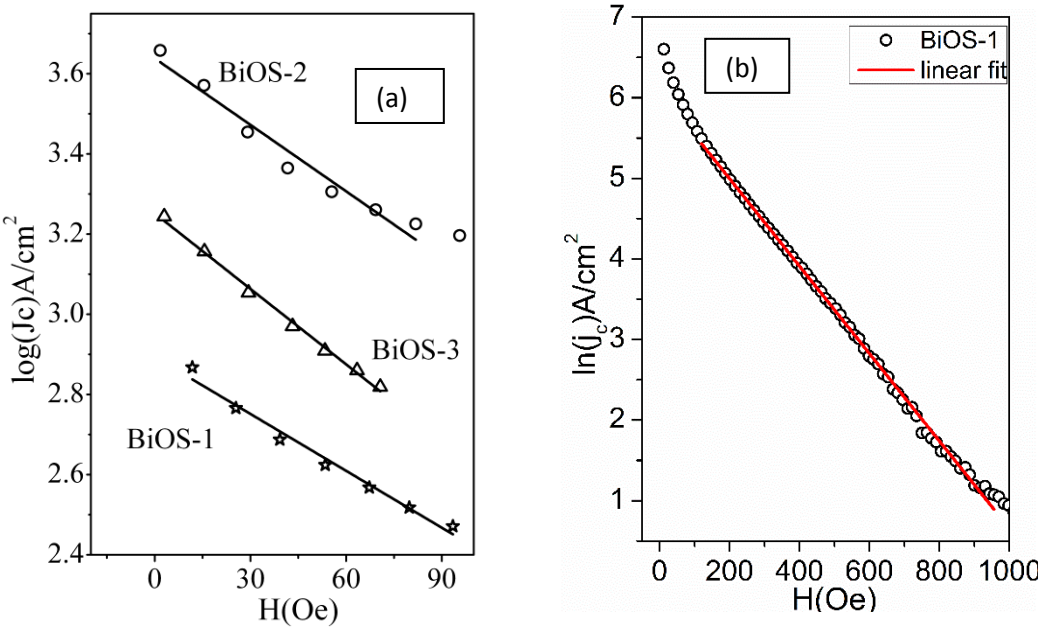

Figure 3.8 *Plots between log (J_c) and applied field (H) (a) Region 1: Linear fit to the data at low fields for all samples (b) Region 2: Linear fit to the data at high fields for BiOS-1 sample.*

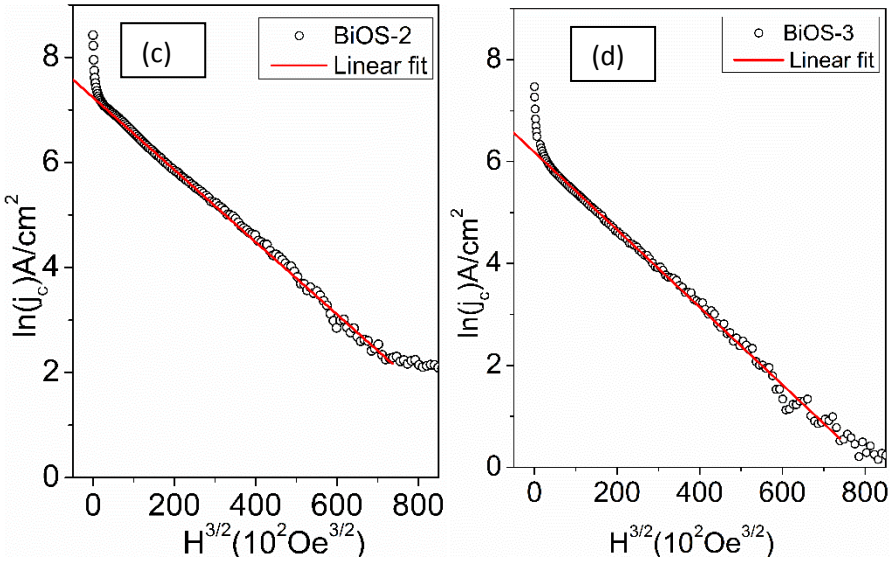

Figure 3.8 *Plots between log (J_c) and ($H^{3/2}$) for (c) BiOS-2 (d) BiOS-3*

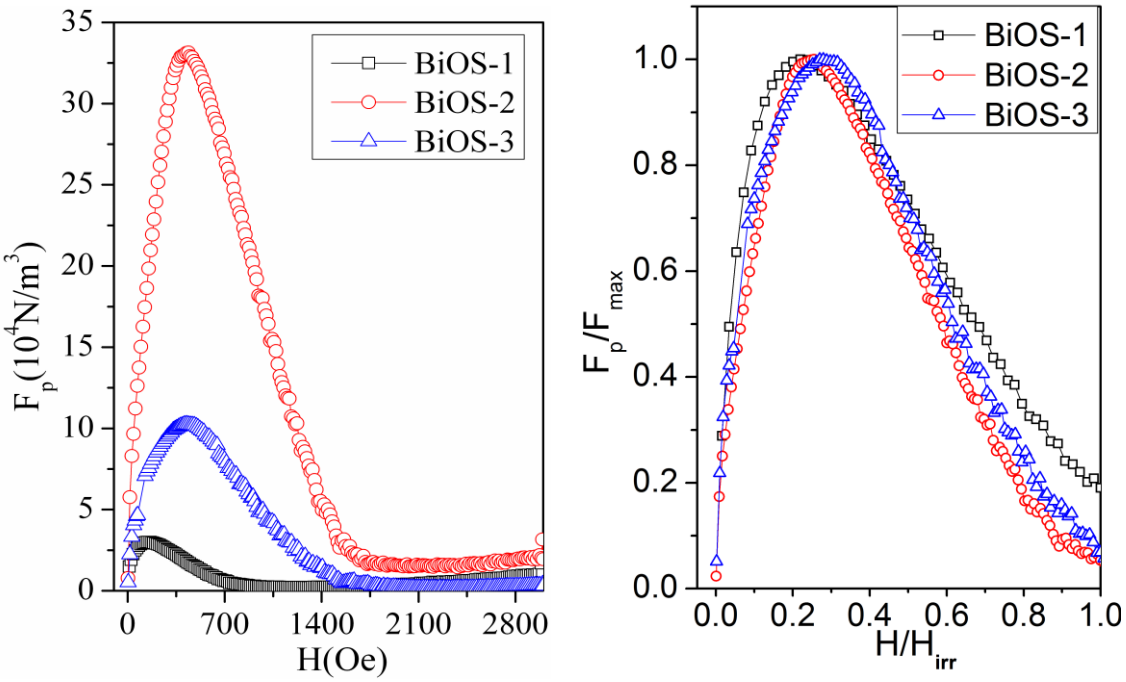

Figure 3.9 *(a) Pinning force vs. applied field and (b) Normalized pinning force vs. reduced field.*

Pinning force per unit volume for the sample is calculated from critical current density (J_c) and applied field intensity (H) using the equation of $F_p=J_c\mu_0 H$, where $\mu_{0=}4\pi*10^{7}N/A^2$ is vacuum permeability. Figure 3.9*(a)* shows the plot of pinning force vs. applied magnetic field which shows that the pinning force increases by an order of magnitude as 5% excess Bi_2O_3 is added in the sample. Further increase in excess Bi_2O_3 to 10% leads to decrease in pinning force. In BiOS-1 sample Bi and Bi_2S_3 impurities act as pinning centers. Whereas in case of BiOS-2 and BiOS-3 samples unreacted Bi_2O_3 impurities also act as pinning centers in addition to Bi and Bi_2S_3 impurities leading to increase in the density of pinning centers. This leads to shift in pinning force peak towards higher field with increase in Bi_2O_3 content. This is in line with the studies on other superconductors i.e. the pinning force is directly proportional to the density of pinning centers [22]. The higher pinning strength in BiOS -2 sample results in higher H_{irr} field among the three samples. Figure 3.9*(b)* shows the normalized flux pinning force per unit volume (F_p/F_{max}) response against the reduced field $h=H_{appl}/H_{irr,}$ (H_{irr} is the applied field up to which the M-H loop is irreversible). This response clearly indicates that the pinning mechanism in the system follows the scaling law as proposed by Krammer [23]. The Scaling law was reported in the case of Nb based superconductors [24-27] and Bi-based superconductors [28]. The obtained maximum value of reduced field (h_{max}) are 0.22, 0.25

and 0.28 for BiOS-1, BiOS-2 and BiOS-3 samples respectively. For the materials containing secondary phases or grain boundaries the maxima occurs at ~0.33.

In case of pinning due to dislocation h_{max} varies between 0.25 and 0.85 depending upon the deformation of the structure [17]. The h_{max} values for the present samples indicate that the pinning mechanism in the present samples is due to core interactions with flux line lattice through grain boundaries and normal metal impurities which are present in the samples.

3.3.1.4 Pinning Mechanism

The geometry of the pinning centers in the present samples is analyzed by Krammer fitting to the response of normalized pinning force per unit volume with reduced field. The best fit is obtained using the equation given below, which is a combination of both surface (first term) and point pinning (second term) mechanism [23].

$$F(h) = A_s h^{0.5} (1-h^2 + B_p h (1-h)^2 \quad (3.3)$$

Figure 3.10 shows best fit (curve-3) as per equation (3.3) obtained by considering combination of point (cuve-1) and surface pinning (curve-2) mechanisms. The obtained A_s and B_p values from the combined best fit curves are given in table 3.2. The combination of surface and point pinning mechanism has been used by other groups [29-30] to explain the pinning mechanism in MgB_2 superconductors.

The h_{max} value of 0.22 obtained for BiOS-1 is close to the value obtained for Bi-based superconductors, indicating pinning mechanism to be similar to that of Bi-based superconductors i.e. the surface pinning due to grain boundaries and the point pinning due to secondary phases [31]. In case of BiOS-2 and BiOS-3 samples the h_{max} values are 0.26 and 0.28 which are close to that of YBCO superconductors, so pinning mechanism in these samples follows collective pinning model [32]. According to collective pinning model, in case of weak pinning forces when an individual pinning center causes a weak deformation of the flux line lattice, if a current is flowing a large region of the flux line lattice containing many pinning centers displaces as a whole. Regions of the vortex lattice in which relative shifts are less than the action force radius (r_f) will be called correlated regions. When the size of the correlated region becomes of the order of the lattice parameter, then the pinning force reaches maximum value and then it drops proportional to *(1-h)* [14, 16].

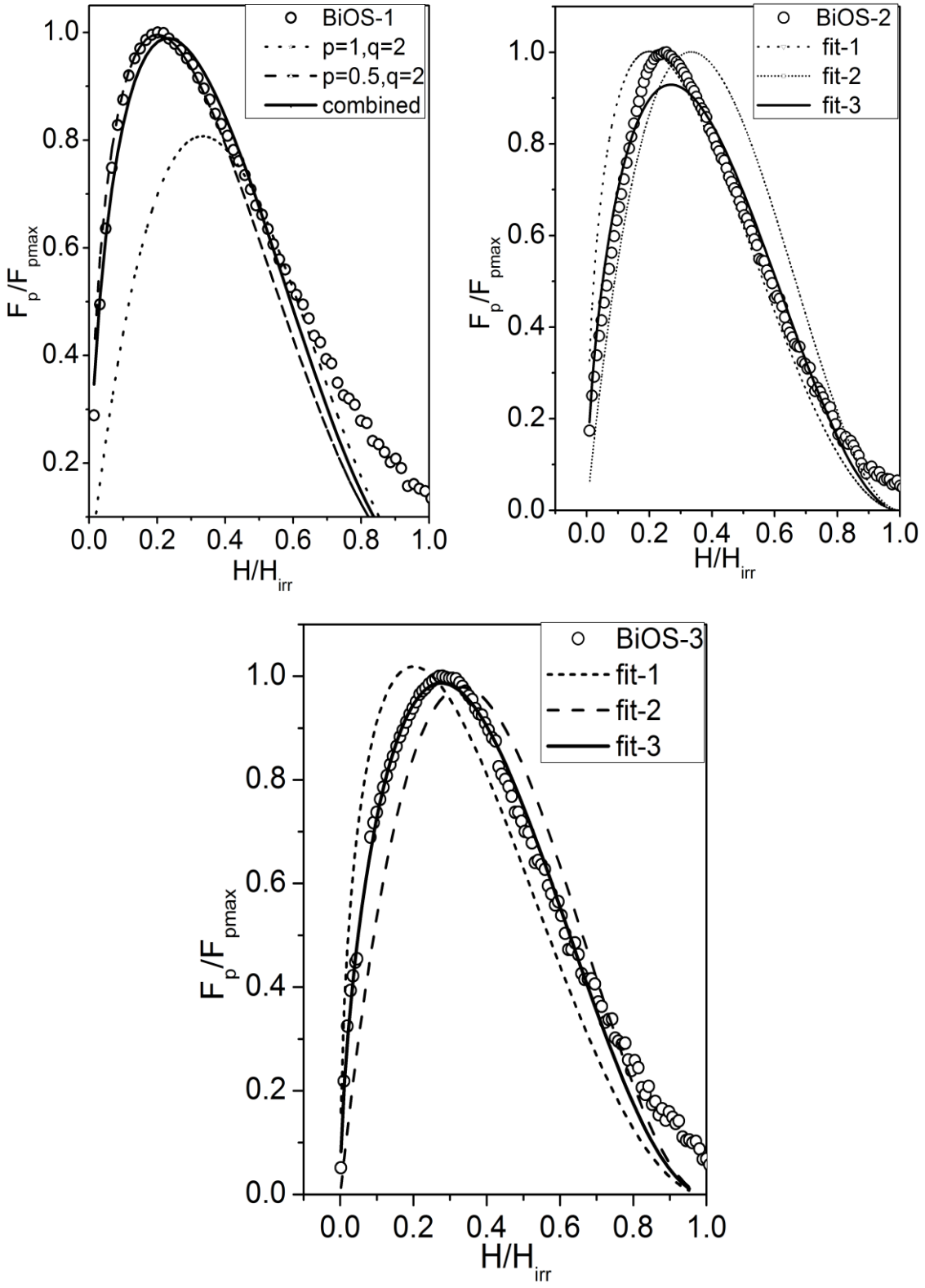

Figure 3.10 *Kramer fitting for the plots between normalized pinning force and reduced field for the BiOS-1, BiOS-2 and BiOS-3 samples. Fit-1 is point pinning (p=1, q=2), fit-2-surface pinning (p=0.5, q=2) and fit-3 is combination of surface and point pinning.*

Table 3.2. *Characteristic parameters and fitting parameters of samples.*

Sample	Grain size (nm)	J_{cmax} (10^3A/cm^2)	F_{max} (10^4dyne/cm^3)	H_{irr} (Oe)	h_{max}	A_s (p=0.5, q=2)	B_p (p=1, q=2)
BiOS-1	**545**	**0.8**	**3.0**	**800**	**0.22**	**2.64**	**1.85**
BiOS-2	**977**	**4.7**	**33.1**	**1656**	**0.26**	**1.77**	**3.05**
BiOS-3	**745**	**1.8**	**10.3**	**1246**	**0.28**	**1.71**	**3.58**

The surface pinning is the dominating pinning mechanism in BiOS-1 sample as indicated by higher value of A_s. Good fit is observed at low h value which suggests the surface pinning domination at low fields. At high h values the point pinning mechanism is found to dominate in BiOS-1 sample.

In case of BiOS-2 and BiOS-3 samples the best fit was observed as per equation *(3.3)* suggesting the presence of both surface and point pinning centers. The point pinning dominates the surface pinning in these sample as indicated by higher value of B_p. The excess Bi_2O_3 acts as point pinning centers. These results suggest that in the present superconductors, J_c dependence on external field follows the collective pinning model. The low J_c values are due to weak links of superconducting grains.

3.3.2. Effect of excess Bi and S on the synthesis of $Bi_4O_4S_3$

In this section we present the synthesis and discussion on results of $Bi_4O_4S_3$ synthesized with excess Bi and S. As the melting points of Bi and S are 270^{o}C and 110^{o}C, i.e., less than the processing temperature of $Bi_4O_4S_3$ (510^{o}C), there is a possibility for off-stoichiometry of Bi and S in $Bi_4O_4S_3$ due to evaporation of Bi and S.

Sample with 10% of excess Bi and S in addition to the stoichiometric ratio were prepared through solid state reaction method and named as BiOS-4 in the series. The comparative results of stoichiometric sample (BiOS-1) and $Bi_4O_4S_3$ sample synthesized with excess Bi and S (BiOS-4) are presented here as follows.

X-Ray diffraction pattern of the samples are shown in figure 3.11. From this figure we can clearly observe that no extra peaks other than $Bi_4O_4S_3$, Bi_2S_3 and Bi are observed

in BiOS-4. Lattice parameters for BiOS-4 are a=3.9666A^0, c=41.3286A^0, which indicated decrease in lattice parameter c from that of BiOS-1 (a=3.9703A^0, c=41.3984A^0).

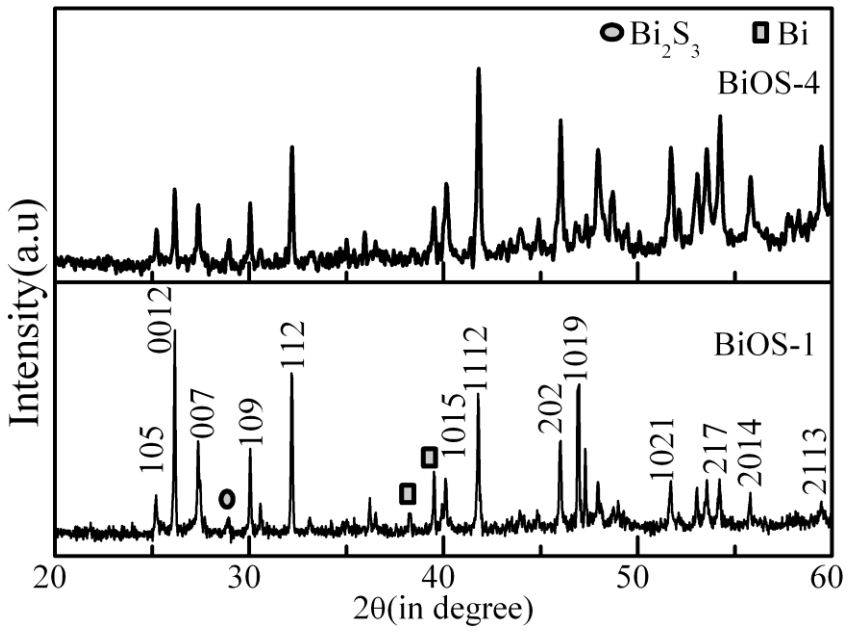

Figure 3.11 *Comparative normalized XRD pattern for the samples.*

FESEM images for the BiOS-1 and BiOS-4 samples are shown in figure 3.12. Platelets like grains confirm the two dimensional layer structure of $Bi_4O_4S_3$ in both the samples. Average grain size, calculated using image-j software, is 545nm and 610nm for BiOS-1 and BiOS-4 samples respectively. Composition analysis of BiOS-4 through energy dispersive spectra is given in figure 3.13. From this figure it is clear that two major phases are identified, one is stoichiometric $Bi_4O_4S_3$ and another one is Bi and S rich phase with oxygen deficiency, which is responsible for the change in superconducting properties of BiOS-4.

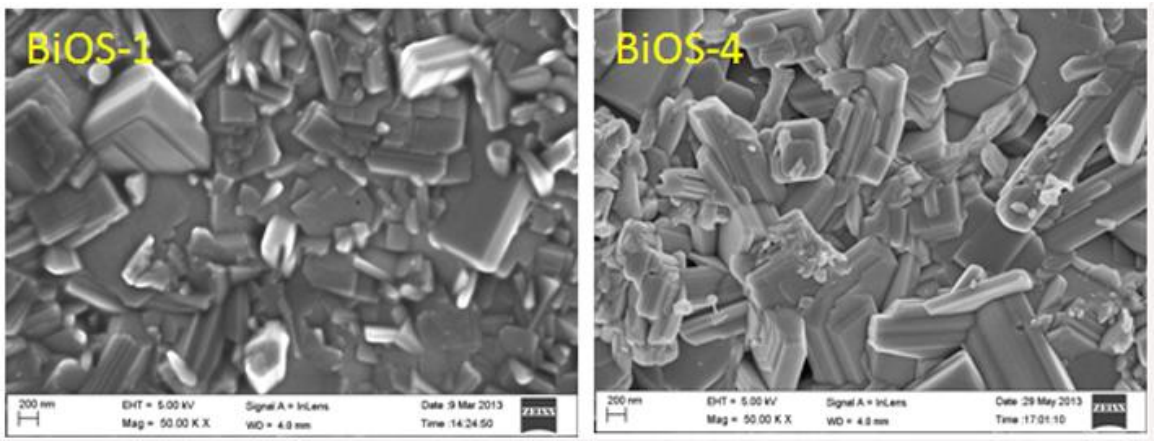

Figure 3.12 *FESEM images for BiOS-1, BiOS-4 samples*

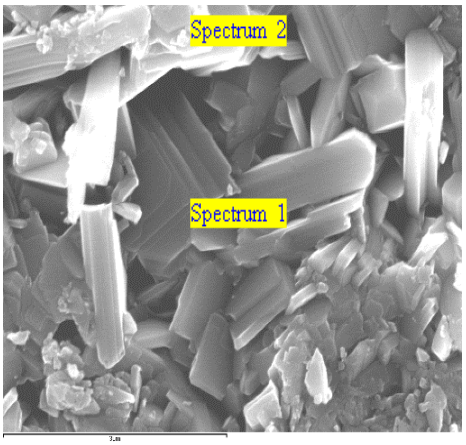

	Spectrum 1		Spectrum 2	
Element	Weight%	Atomic%	Weight%	Atomic%
O K	3.19	21.32	6.24	35.51
S K	10.29	34.36	9.84	27.93
Bi M	86.52	44.32	83.92	36.56
Totals	100.00		100.00	

Figure 3.13 *EDS analysis of the BiOS-4 sample.*

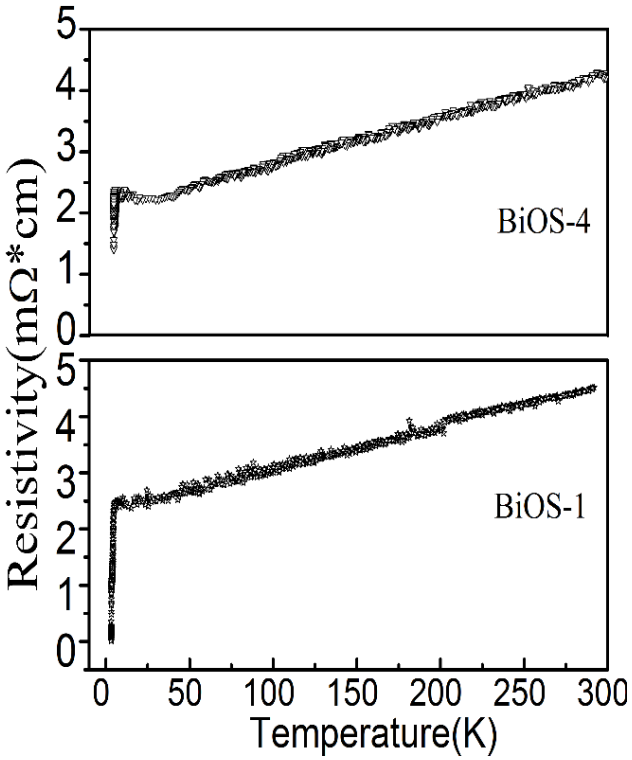

Figure 3.14 *Resistivity Vs Temperature plots for the BiOS-1 and BiOS-4 samples.*

Resistivity change with temperature of the sample was shown in figure 3.14. The exotic behaviour of this material below 25K is due to the strong single S-wave coupling [4]. RRR, room temperature resistivity and transition temperature variation with composition were given in table 3.3. Normal state properties are not much affected with excess Bi and S in BiOS-4 sample. But suppression of superconducting transition is observed which may be due to decrease in superconducting volume fraction.

Table 3.3 *Comparative table of transport properties of BiOS-1 and BiOS-4*

Sample	T_{onset} (± 0.5K)	AC Susceptibility T_{onset} (± 0.05K)	ρ_{rt} (mΩ.cm)	ρ_0 (mΩ.cm)	RRR	Metallicity (μΩ.cm/K)
BiOS-1	4.9	4.0	4.5	2.3	1.96	7.64
BiOS-4	4.8	3.0	4.3	2.2	1.95	7.40

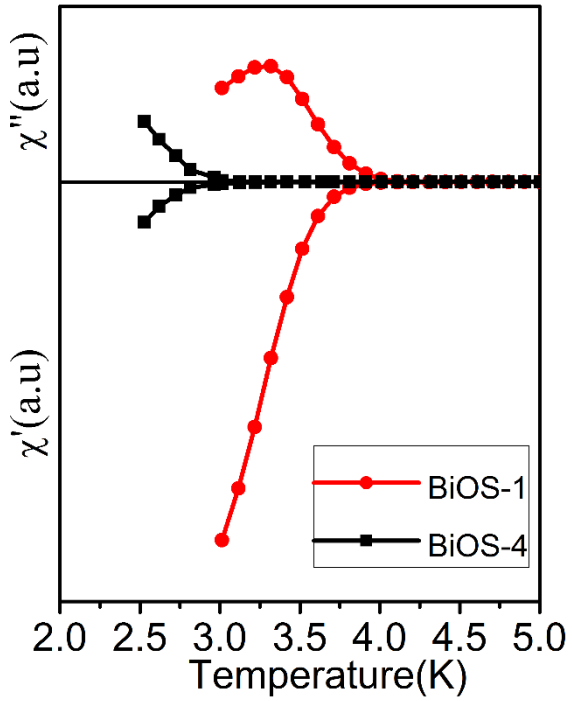

Figure 3.15 *AC Susceptibility variations of the samples with temperature*.

Magnetization study of the samples under applied ac drive field of 10Oe within the temperature range of 5K-2K was shown in figure 3.15. Single peak in the derivative of transition line indicates only one superconducting phase existence in the sample. Transition width is calculated from the peak width of the samples. In case of both BiOS-1 and BiOS-4 samples the right arm of the peak is extrapolated for the estimation of end point at low temperature side. Superconducting onset temperature and volume fraction is decreased in BiOS-4 sample. In spite of increase in grain size and homogeneity the decrease in

superconducting transition temperature and volume fraction is may be due to decrease in the purity of the BiOS-4 sample.

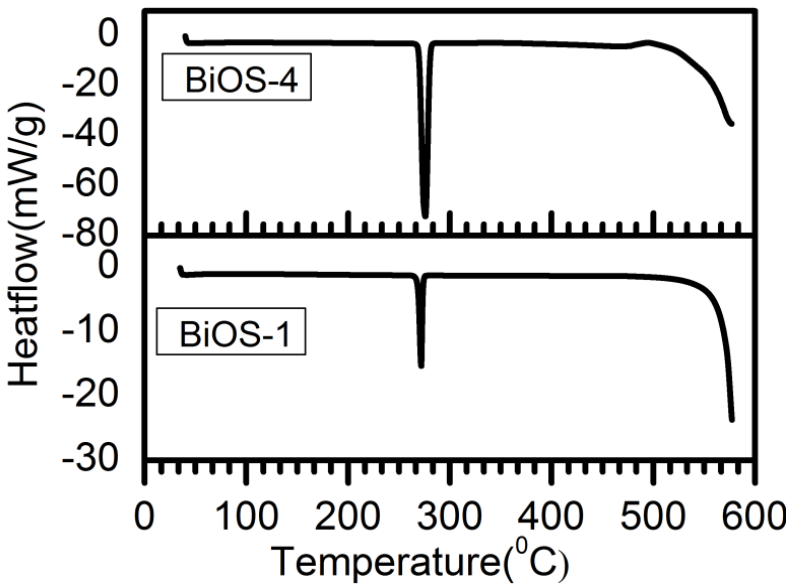

Figure 3.16 *DSC thermo grams for the BiOS-1 and BiOS-4 samples.*

From the DSC studies on BiOS-1 and BiOS-4 samples, as shown in figure 3.16, two exothermic peaks are observed, one is at 270^0C and another one is at 545^0C corresponding to Bi and $Bi_4O_4S_3$ respectively. From the area of the exothermic peak, which is direct measure of enthalpy or heat absorbed for the phase change, we can observe that increase in Bi impurity phase volume and decrease in $Bi_4O_4S_3$ phase volume in BiOS-4 sample when compared to BiOS-1sample. Excess Bismuth and Sulphur helped in the formation of $Bi_4O_4S_3$ with low superconducting volume fraction.

3.4 Chapter Summary

Superconducting Bismuth Oxy Sulphide samples were synthesized with 5% and 10% of excess Bi_2O_3 over and above the required quantity as per stoichiometric composition of $Bi_4O_4S_3$ phase. The excess Bi_2O_3 acts as flux for the $Bi_4O_4S_3$ phase formation and increases the superconducting volume fraction, grain size and critical current density (J_c) compared to the stoichiometric sample. Lattice parameters are almost same for the three samples indicating no significant change in crystal structure. The Transmission electron microscopic images of the samples show them to be multiphase materials. The sample with 5% excess Bi_2O_3 has highest grain size, (T_{onset}) and J_c value. The J_c varies with applied external magnetic field as per the collective pinning model. The pinning force follows scaling law of combination of surface and point pinning. The grain boundaries and impurity

phases act as surface and point pinning centers respectively. The maximum value of reduced field increases from 0.22 to 0.28 as Bi_2O_3 increases, which is close to the value of CuO based superconductors. The dominating pinning mechanism changes from surface pinning to point pinning as the Bi_2O_3 content increases. The J_c values are low due to weak links of the superconducting grains in these materials. The higher J_c values for BiOS-2 sample which has largest grain size indicates that J_c can be increased by increasing the grain size of the sample.

$Bi_4O_4S_3$ samples with 10% excess Bi and S were prepared through solid state reaction method. XRD pattern showed $Bi_4O_4S_3$ phase formation along with Bi and Bi_2S_3 impurity phases. Lattice shrinkage is observed through c axis with no effect along *a*-axis. FESEM images showed slight increment in grain size and homogeneity. The EDS analysis showed most of the grains with Bi rich and S deficiency phase along with superconducting grains. Transport studies reveal that no impact of excess Bi and S on normal state properties of $Bi_4O_4S_3$. T_{onset} is observed at 4.5K but zero transition was not observed. Decrease in T_{onset} and superconducting volume fraction is observed through A.C susceptibility measurement which is in good agreement with transport studies. DSC thermo grams also showed increase in impurity phase contribution in $Bi_4O_4S_3$ synthesized with excess Bi and S. So suppression of T_c and superconducting volume fraction is due to increase in Bi and S rich impurity phase.

References

[1]. Y. Mizuguchi, H. Fujihisa, Y. Gotoh, K. Suzuki, H. Usui, K. Kuroki, S. Demura, Y. Takano, H. Izawa, and O. Miura, *Phys. Rev. B,* **86,** 0220510(R) (2012).

[2]. S.K. Singh, A. Kumar, B. Gahtori, Shruti, G. Sharma, S. Patnayak and V.P.S. Awana, *J. Am. Chem. Soc*., **134,** 16504 (2012).

[3]. H. Takatsu, Y. Mizuguchi, H. Izawa, O. Miura, and H. Kadowaki.: *J. Phys. Soc. Jpn.* **81,** 125002 (2012).

[4]. S. Li, H. Yang, J. Tao, X. Ding, and Hai-Hu Wen, *arXiv*, **1207**, 4955v1 (2012).

[5]. Shruthi, P. Srivastsava, and S. Patnaik, *J. Phys.: Condens. Matter*, **25,** 312202 (2013).

[6]. P. K. Biswas, A. Amato, C. Baines, R. Khasanov, H. Luetkens, Hechang Lei, C. Petrovic, and E. Morenzoni, *Phys. Rev. B,* **88**, 224515 (2013).

[7]. Li Sheng, Yang Huan, Fang DeLong, Wang ZhenYu, TaoJian, Ding XiaXin, and Wen HaiHu: *Sci. China-Phy. Mech. Astron*, **56,** 2019-2025 (2013).

[8]. H. Kotegawa, Y. Tomita, H. Tou, H. Izawa, Y. Mizuguchi, O. Miura, S. Demura, K. Deguchi, and Y. Takano: *J. Phys. soc. Jpn*., **81,** 103702 (2012).

[9]. G. Kalai Selvan, M. Kanagaraj, S. Esakki Muthu, Rajveer Jha, V. P.S. Awana and S. Arumugam, *Phys. Status Solidi RRL* **7,** 510-513 (2013).

[10]. S. G. Tan, L. J. Li, Y. Liu, P. Tong, B. C. Zhao, W. J. Lu, Y. P. Sun, *Physica C* **483,** 94 (2012).

[11]. W. Adam Phelan, David C. Wallace, Kathryn E. Arpino, James R. Neilson, Kenneth J. Livi, Che R. Seabourne, Andrew J. Scott, and Tyrel M. Mcqueen, *J. Am. Chem. Soc*. **135,** 5372-5374 (2013).

[12]. P. Srivatsava, Shruti and S. Patnaik, *Supercond. Sci. Technol.* **27,** 055001 (2014).

[13]. Annapurna Mohanta, Dhrubananda Behra, Simanchalo Panigrahi and Naresh Chandra Mishra, *Indian J. Phys.* **83(4),** 455-463 (2009).

[14]. Candida C, Silva and M. E. McHenry, *IEEE Transaction on Applied Superconductivity*, **7**, 2 (1997).

[15]. N. P. Liyanawaduge, Shiva kumar Singh, Anuj Kumar, V. P. S. Awana, H. Kishan, *J. Supercond. Nov. Magn*., **24**, 1599-1605 (2011).

[16]. Luis De Los Santos V,Angel Bustamante D, J. C. Gonzalez, Juan Feijoo L, Ana Osorio A, Thanos Mitrelias, Yutaka Majima and Crispin H. W. Barnes, *The open superconductors Journal*, **2,** 19-27 (2010).

[17]. A. M. Campbell and J. E. Evetts, *Adv. Phys*. **21,** 199 (1972).

[18]. R. Singh, *J. Phys. D: Appl. Phys.*, **22,** 1523-1527 (1989).

[19]. Chandra shekhar, Amit Srivastava, Pramod Srivastava, Pankaj Srivastava and O.N Srivastava, *Supercond. Sci. Technol*., **25**, 045004 (2012).

[20]. G. Blatter, M. Y. Feigelman, Y. B. Geshkenbein, A. I.Larkin, and V. M. Vinokur, *Rev. Mod. Phys*., **66,** 1125 (1994).

[21]. D. Dew-Hughes, *Philosophical Magazine*, **30**, 2, 293-305 (1974).

[22]. A. I. Larkin and Yu. N. Ovchinnikov, *Journal of Low Temperature Physics*, **34,** 3-4 409-428 (1979).

[23]. E. J. Kramer, *J. Appl. Phys*., **44,** 3 (1973).

[24]. Ronald E. Enstrom and John R. Appert, *J. Appl. Phys*., **43,** 4 (1972).

[25]. K. Tachikawa, Y. Tanaka, and Y. Iwasa, *J. Appl. Phys*., **44,** 2 (1973).

[26]. Yu. F. Bychkov, V. G. Verreshchagin, V. R. Karasik, G. B. Kurganov, and V. A. Mal'Tsev, *Soviet Physics JETP*, **29,** 2 (1969).

[27]. A. K. Raychaudhuri, T. Takayama, and L. Rinderer, *Journal of Low Temperature Physics*, **41,** 1-2 (1980).

[28]. J. M. Gonzalez Calbet, A. Badia, M. Vallet Regf, A. Caneiro, J. Ramirez, C. Rillo, F. Lera, and R. Navarro, *Physica C*, **203,** 223-230 (1992).

[29]. C. H. Cheng, Y. Yang, P. Munroe and Y. Zhao.: *Supercond. Sci. Technol*., **20**, 296-301 (2007).

[30]. D. Tripathi and T. K. Dey, *J. App. Phys*., **114,** 093906 (2013).

[31]. H. Yamasaki, K. Endo, S. Kosaka, M. Umeda, S. Yoshida, and K. Kajimura.: *Phys. Rev. Lett.*, **70,** No. 21 (1993).

[32]. L. W. Song, M. Yang, E. Chen and Y. H. Kao, *Phys. Rev. B*, **45,** No.6 (1992).

CHAPTER 4

Structure and Properties of Ca doped Bismuth Oxy Sulphide Superconductor

4.1 Introduction

In this chapter discussed about the Ca doping effects in Bismuth Oxy Sulphide superconductor.

Multiphase existence along with impurity phases complicates the doping studies in $Bi_4O_4S_3$ [1]. The Se doping in $Bi_4O_4S_3$ at S site results in decrease in T_c due to expansion of lattice parameters because of bigger atomic size of Se. The content of Bi_2S_3 phase slightly increases with increase in Se content [2]. The doping of Ag in $Bi_4O_4S_3$ resulted in gradual suppression in lattice parameters and T_c, and shows semiconducting behaviour beyond some doping level. The suppression of T_c is ascribed to shift in the Fermi energy level [3]. The introduction of CuS_2 layer in $Bi_4O_4S_3$ by replacing Bi with Cu in BiS_2 superconducting layer resulted in suppression of T_c. The XRD peak intensity for the impurity phase is almost invariable with Cu doping level. This indicates that the Cu dopant is going into $Bi_4O_4S_3$ phase and both the lattice parameters shrink with Cu doping till x=0.1, beyond that it exhibits semiconducting behaviour. It is mainly due to the change in electronic structure, the Fermi energy shifts away from density of states by Cu or Ag doping [4]. As the number of CaO layers play important role in Bi-based high T_c superconductors, in the present study we have introduced Ca in $Bi_4O_4S_3$ by doping Ca at Bi site.

4.2 Experimental Techniques

Polycrystalline $Bi_{4-x}Ca_xO_4S_3$ (x=0, 0.25, 0.5, 0.75, 1) samples were prepared by solid state reaction method. Pure Bi_2O_3 powder, $CaCO_3$ powder, Bismuth metal granules and Sulphur flakes (all from sigma Aldrich with purity>99.99%) were mixed in stoichiometric ratio of the formulae $Bi_{4-x}Ca_xO_4S_3$ (x=0, 0.25, 0.5, 0.75, 1) and grinded for 1 hour using an agate mortar. Then the Pellets were prepared using a hydraulic press at ambient conditions. The samples were sealed in a quartz tube under the vacuum of

$5x10^{-4}$Torr and sintered at 510^{o}C for 18 hours followed by furnace cooling. The same procedure was repeated twice to get better homogeneity.

To study the crystalline structure, X-ray diffraction (XRD) patterns of the samples were recorded using powder X-ray diffraction (Bruker) with Cu-k_{α} radiation. Peak assignment and lattice parameters were analyzed using FullProf software. Layer structure of the synthesized materials is confirmed by TEM studies. Surface morphology was analyzed using Field emission scanning electron microscopy (FESEM) and Energy dispersive X-ray spectroscopy (EDS). The electrical properties of the samples were measured by conventional four probe method using a closed cycle refrigerator. The A.C susceptibility and *M-H* loops were recorded on rectangular samples, using physical property measurement system (PPMS Quantum design).

4.3 Results and Discussion

4.3.1 Structural Properties

X-ray diffraction pattern of the samples $Bi_{4-x}Ca_xO_4S_3$, ($0<x<1$) are shown in figure 4.1. Figure 4.1*(a)* is multiphase refinement spectra for un-doped sample. It clearly shows the $Bi_4O_4S_3$ superconducting phase along with small amounts of Bi and Bi_2S_3 impurity phases. Polycrystalline $Bi_4O_4S_3$ samples have tetragonal structure and the lattice parameters are refined using FullProf software with space group I4/mmm and the obtained values are a=3.9704A^{o}, c=41.3969A^{o}. Figure 4.1*(b)* shows refined spectra for $Bi_{4-x}Ca_xO_4S_3$ with x=0.25 sample through which clear multiphase existence can be observed. Refined lattice parameters for this sample are a=3.9668A^{o}, c=41.3467A^{o}. Figure 4.1(*c*) shows the comparative normalized XRD spectra for $Bi_{4-x}Ca_xO_4S_3$ samples with 'x' ranging from 0 to 1. It can be clearly observed from figure 4.1*(c)* that the intensity of Bi_2S_3 phase peak increases at the expense of intensity of peaks corresponding to superconducting $Bi_4O_4S_3$ phase with increase in Ca doping. XRD spectra of sample with x=0.25 shows increase in intensity of peaks corresponding to $Bi_4O_4S_3$ as well as Bi_2S_3 phase. For samples with $x\geq$ 0.5, impurity peak intensity corresponding to Bi and Bi_2S_3 phase increases and $Bi_4O_4S_3$ phase peak intensity decreases with increase in Ca content.

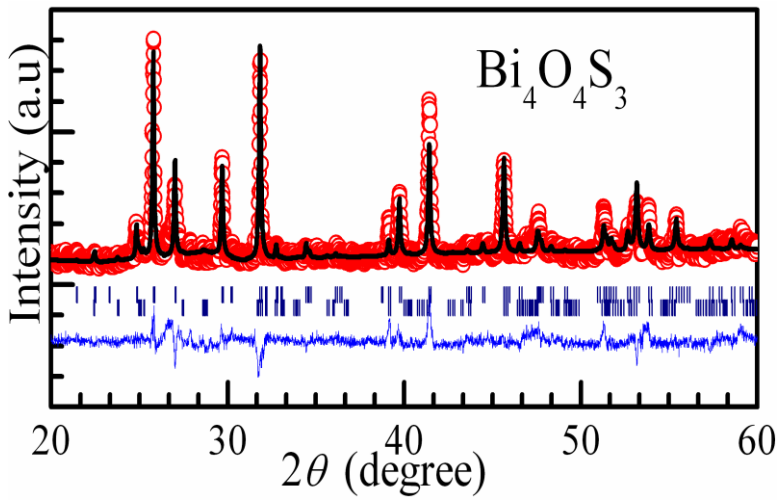

Figure 4.1(a) *Refined XRD pattern for $Bi_{4-x}Ca_xO_4S_3$, with x=0 sample.*

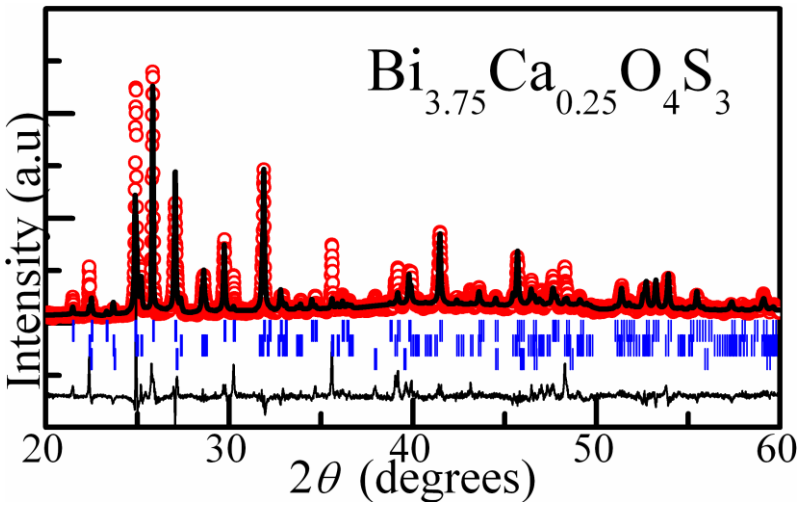

Figure 4.1(b) *Refined XRD spectra for $Bi_{4-x}Ca_xO_4S_3$ with x=0.25 sample.*

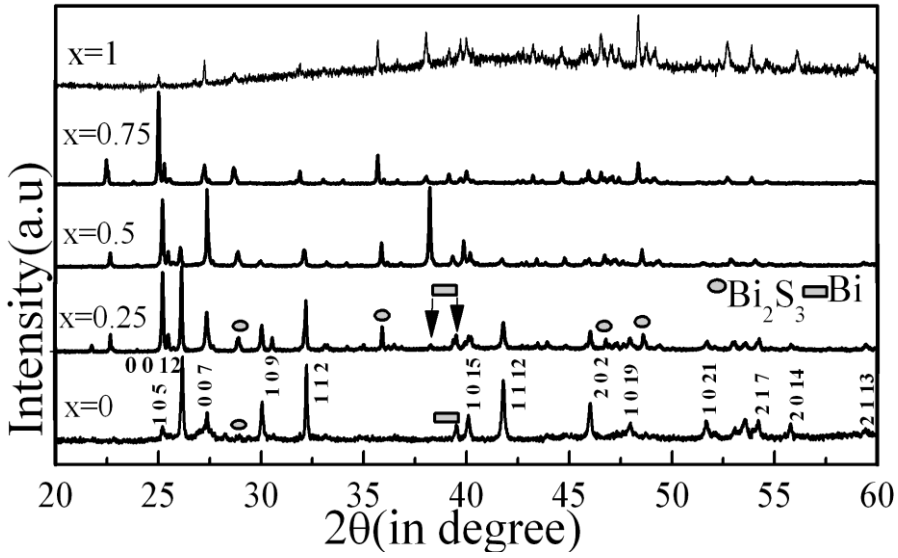

Figure 4.1(c) *Comparative XRD spectra for $Bi_{4-x}Ca_xO_4S_3$ samples with x=0 to 1.*

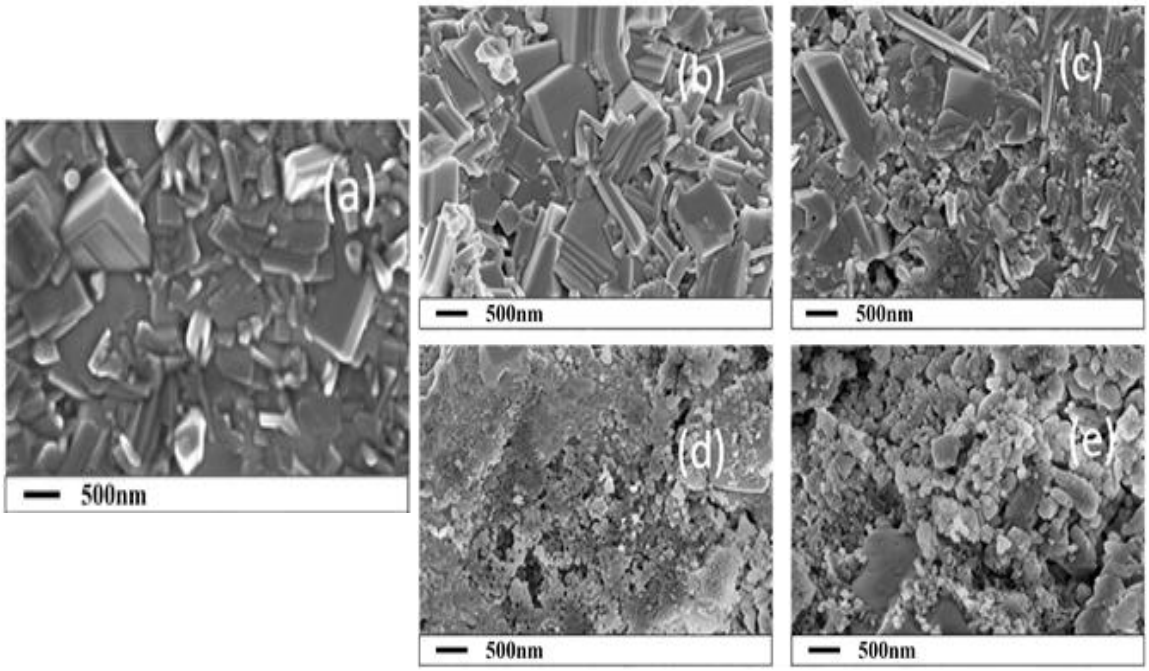

Figure 4.2 *FESEM images for $Bi_{4-x}Ca_xO_4S_3$ samples with x=0 (a), 0.25 (b), 0.5 (c) 0.75 (d) and 1 (e).*

The FESEM images of various samples are shown in figure 4.2. The un-doped sample shows platelet like structure confirming the two dimensional growth of crystal in the sample. Whereas in sample with x=0.25 increase in the size of the platelets is observed. These results are in good agreement with the increase in T_c and the superconducting volume fraction in this sample. The sample with x=0.5 shows platelet like structure along with Ca rich Bi_2S_3 phase. It is also observed that as the Ca doping level increases, the deteriation/disintegration of superconducting phase is clearly observed in these images. EDAX analysis also confirmed the presence of two different phases i.e. Ca doped layer structured $Bi_4O_4S_3$ phase and Ca rich Bi_2S_3 phase.

4.3.2 Micro Structural analysis using TEM

In order to understand the microstructure features, $Bi_{4-x}Ca_xO_4S_3$, ($0<x<1$) samples were studied through extensive structural investigations by means of selected area diffraction (SAED) pattern and high resolution TEM.

Figure 4.3 shows TEM images of undoped $Bi_4O_4S_3$ sample. Figure 4.3*(a)* clearly shows the polycrystalline $Bi_4O_4S_3$ phase. The lattice spacing *(d)* values are calculated from the diameter of the rings, which can be matched with the d-spacing of $Bi_4O_4S_3$ with high (*h k l*) values in XRD spectra. It also reveals the presence of polycrystalline Bi metallic phase. The double spots on the rings with high intensity are from the same (*h k l*) planes of

these two different phases. Figure 4.3*(b)* shows single crystalline diffraction pattern (DP) corresponding to Bi_2S_3 phase. Lattice parameters for $Bi_4O_4S_3$ and Bi_2S_3 were calculated from the d-spacing values of DP. The high resolution TEM image in Figure 4.3*(c)* shows existence of Bi_2S_3 Nanoparticles in $Bi_4O_4S_3$. Figure 4.3*(d)* shows the presence of inhomogeneity and multi phases in the sample. Lattice fringes corresponding to $Bi_4O_4S_3$ and Bi_2S_3 along with defects like lattice dislocations and grain boundaries can be observed. The structural phase separation and complex superstructure commonly observed in HRTEM and DP have been mainly ascribed to the presence of impurities in the sample [5].

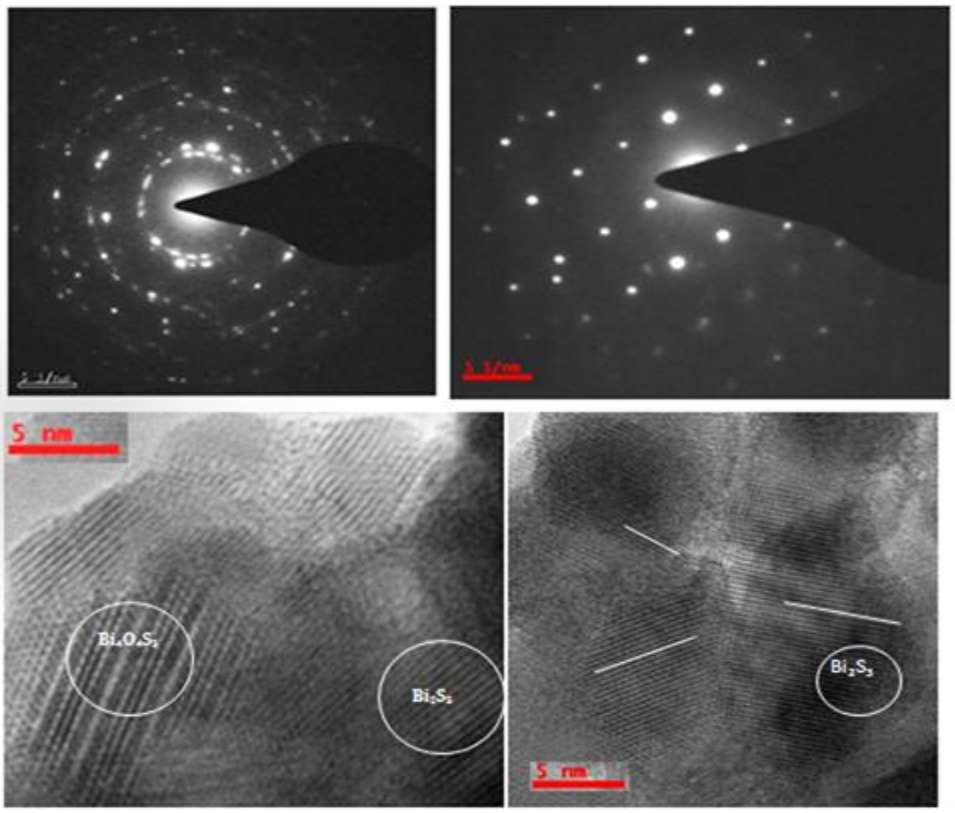

Figure 4.3 *shows TEM images of undoped $Bi_4O_4S_3$ sample.*

The SAED pattern of the sample with x=0.25 is shown in figure 4.4*(a)*. The ring pattern confirms two phases i.e. polycrystalline Bi and $Bi_4O_4S_3$ phases, identified through the d-spacing calculations from the diameter of the rings in SAED pattern. Figure 4.4*(b)* shows HRTEM image of sample with lattice fringes corresponding to $Bi_4O_4S_3$. Figure 4.4*(c)* shows lattice fringes in HRTEM from crystallized Bi_2S_3. Average grain size of Bi_2S_3 is found to be ~25nm. Figure 4.4*(d)* shows the interference pattern of two DP originating from single crystalline Bi_2S_3 and single crystalline $Bi_4O_4S_3$ grains. Lattice parameters calculated for these two phases from SAED pattern are listed in table 4.1. TEM images show that Bi_2S_3 is well crystallized and corresponding SAED pattern (figure 4.4*(d)*) shows

unique pattern of diffraction spots which can be readily indexed with (0 0 2) and (2 2 0) planes, confirming that the Bi_2S_3 has single crystalline structure along the [0 0 1] growth direction consistent with SAED pattern results. The d-spacing values calculated from HRTEM image (figure 4.4*(c)*) correspond to the (1 1 0) and (0 0 1) planes. These results are in good agreement with the earlier reports on high crystalline bismuth Sulphide Nano-rods [6-7]. Lattice defects, particularly dislocations in the superconductor having complex structure, are observed in these materials. Preferential fractures in between the layers can also be observed through HRTEM image.

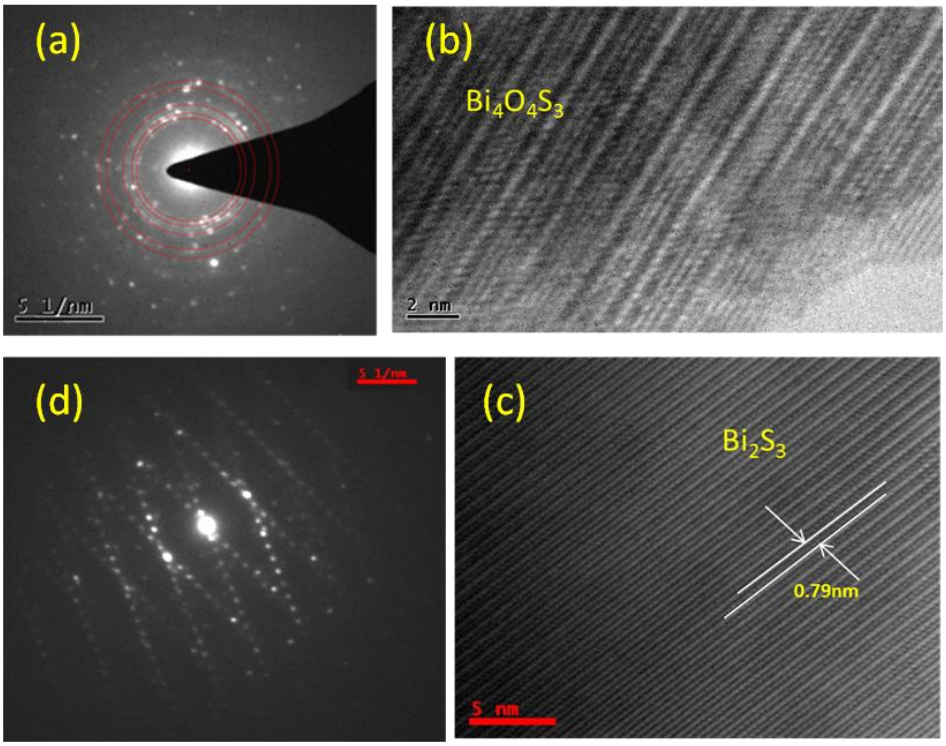

Figure 4.4 *TEM images for the $Bi_{4-x}Ca_xO_4S_3$, x=0.25 samples.*

Figure 4.5 shows TEM images for sample with *x*=0.5. The HRTEM image (figure 4.5*(a)*) clearly shows the lattice fringes corresponding to Bi_2S_3 phase. SAED pattern (figure 4.5*(b)*) shows overlapping of three phases in which Ring pattern confirms polycrystalline Bi and $Bi_4O_4S_3$ phase. Yellow colour ring corresponds to polycrystalline Bi phase. These results are in good agreement with the XRD results where XRD peak corresponding to the d-value of 2.3579A^o from Bismuth has highest intensity. In diffraction pattern the double spots correspond to two overlapped phases identified as $Bi_4O_4S_3$ and single crystalline Bi_2S_3. Lattice parameters calculated from SAED pattern are listed in table 4.1. Figure 4.5*(c)* shows SAED pattern for single crystalline grain of Bi phase. Figure 4.5*(d)* shows single crystalline Bi_2S_3 phase.

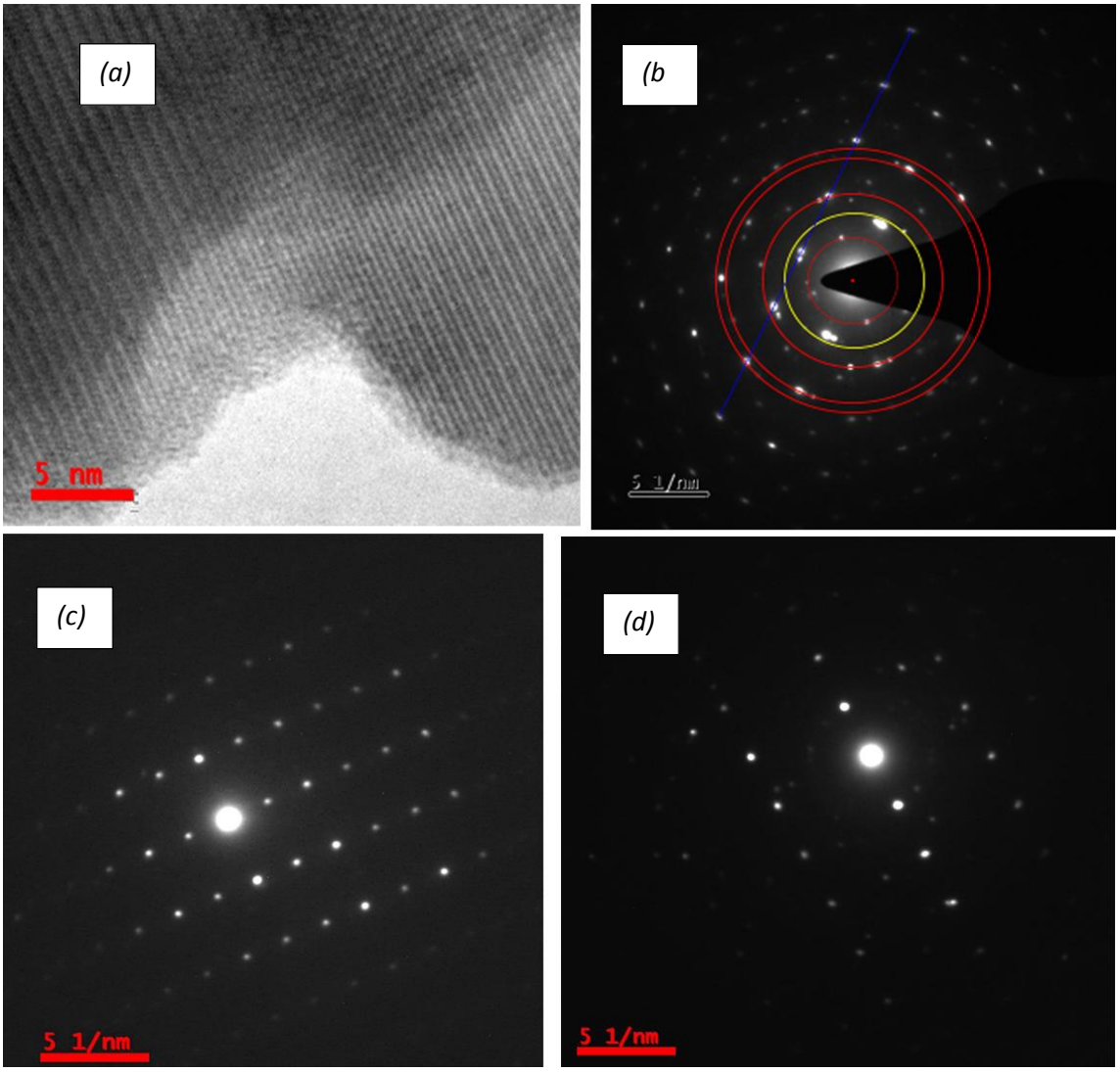

Figure 4.5. *TEM images for the $Bi_{4-x}Ca_xO_4S_3$, x=0.5 samples.*

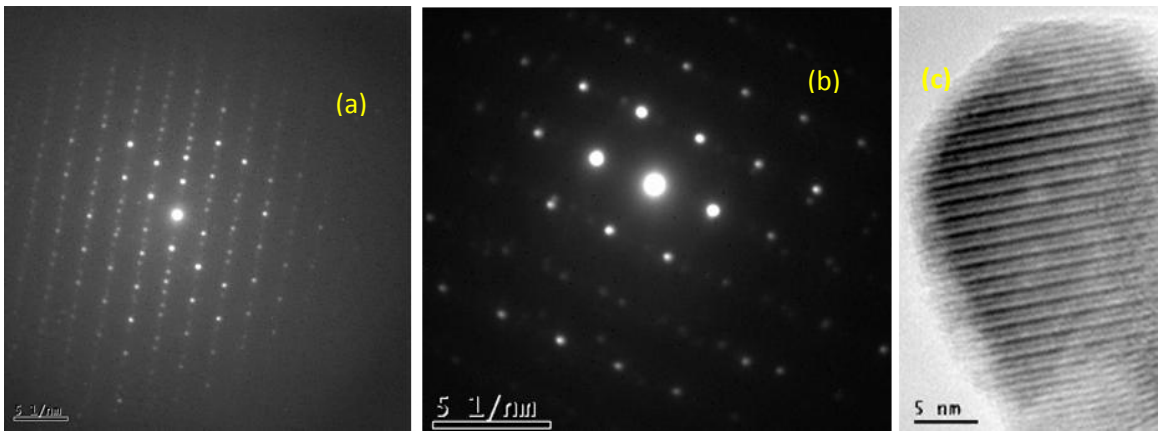

Figure 4.6 *TEM images for the $Bi_{4-x}Ca_xO_4S_3$, x=0.75 samples.*

Figure 4.6 shows TEM images for *x*=0.75 sample. It can be observed from the diffraction pattern (figure 4.6*(a)*) that the sample contains twin boundaries. The most

striking structural phenomena observed in the TEM observations are the appearance of series of super lattice spots along with the main diffraction spots. Superstructure reflections around basic Brag spot in figure 4.6*(a)* originate from the domains, where the superstructure vectors are twinned. Generally twinning is due to lattice mismatch between two different phases. The two different phases are identified as single crystalline Bi_2S_3 and single crystalline grain of $Bi_4O_4S_3$. Figure 4.6*(b)* shows the diffraction pattern from a super lattice consisting of single crystalline grains of Bi and Bi_2S_3. The lattice mismatch between Bi_2S_3 and Bi is comparatively less thus the Bi_2S_3 and Bi diffraction patterns appear as one diffraction pattern [6]. The HRTEM image shows lattice planes corresponding to Bi_2S_3 (figure 4.6*(c)*). The calculated lattice parameters are given in table 4.1.

Table 4.1 *Lattice parameters for Bi_2S_3 and $Bi_4O_4S_3$ calculated from TEM-SAED pattern.*

Sample name	Bi_2S_3			$Bi_4O_4S_3$	
	***a* (A^0)**	***b* (A^0)**	***c* (A^0)**	***a=b* (A^0)**	***c* (A^0)**
Ca (*x*) = 0	**11.17**	**11.54**	**3.90**	**3.97**	**41.44**
Ca (*x*) = 0.25	**11.11**	**11.41**	**3.99**	**3.97**	**41.52**
Ca (*x*) = 0.5	**11.16**	**11.34**	**3.94**	**3.99**	**41.38**
Ca (*x*) = 0.75	**11.14**	**10.55**	**4.08**	**3.9**	**41.4**
Ca (*x*) = 1	**11.08**	**11.43**	**3.92**	**3.99**	**41.44**

Figure 4.7 shows TEM images for *x*=1 sample. SAED pattern shown in figure 4.7*(a)* confirms the multiphase existence in the sample. Amorphous background (continuous ring pattern) confirms the disintegrated polycrystalline $Bi_4O_4S_3$ phase. Line pattern is due to single crystalline Bi_2S_3 phase and some low intensity points on circle correspond to single crystalline grain of $Bi_4O_4S_3$. Figure 4.7*(b)* represents incommensurate modulation of Bi_2S_3 and $Bi_4O_4S_3$. The super lattice spots followed by main phase spots were observed. Two spots were identified as $Bi_4O_4S_3$ with *d* spacing 3.042 (1 0 9) 2.73 (1 0 11). The third spot corresponds to Bi_2S_3 with *d* spacing 3.146 (2 3 0). Lattice parameters calculated using d spacing of diffraction pattern are given in table 4.1. The HRTEM image for this sample shown in figure 4.7(*c*) represents lattice planes of Bi_2S_3 phase.

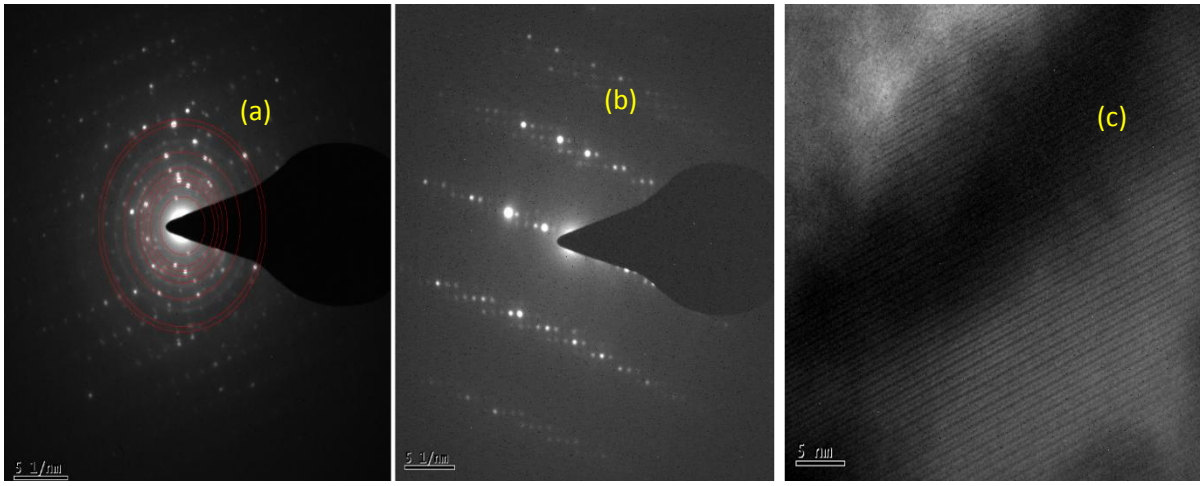

Figure 4.7 *TEM images for the* $Bi_{4-x}Ca_xO_4S_3$, *x=1 samples.*

4.3.3 Transport Properties

The resistivity verses temperature for various samples are shown in figure 4.8*(a).* Figure 4.8*(b)* shows resistivity variation at low temperature for *x*=0 and *x*=0.25 samples indicating increase in superconducting transition temperature (T_c) with Ca doping. The superconducting transition temperature values T_c^{onset} and T_c^{zero} are given in table 4.2. Change in room temperature resistivity, metallicity and residual resistivity ratio were calculated for *x*=0 and *x*=0.25 samples and the corresponding values were given in table 4.2. The increment in T_c^{onset} is due to the larger grain size of *x*=0.25 sample which can reduce the grain boundaries and help superconducting grains to couple at higher temperature to reach global superconductivity. The decrease in RRR and increase in metallicity in *x*=0.25 sample is due to increase in grain size and homogeneity and decrease in defects like grain boundaries. The *x*=0.5 sample shows metal to semiconductor transition at ~150K with no significant change in T_c (onset). The *x*=0.75 sample shows metallic behaviour up to 175K as temperature is lowered below room temperature followed by semiconducting behaviour with further decrease in temperature. Sample with *x*=1 shows weak semiconducting behaviour down to 100K and strong semiconducting behaviour below 100K. The change in transport properties with Ca doping is mainly due to the structural changes. As indicated by TEM analysis it is confirmed that Ca is going into interstitial position of Bi_2S_3 phase which could be the reason for the increase in semiconducting behaviour with Ca doping in $Bi_4O_4S_3$.

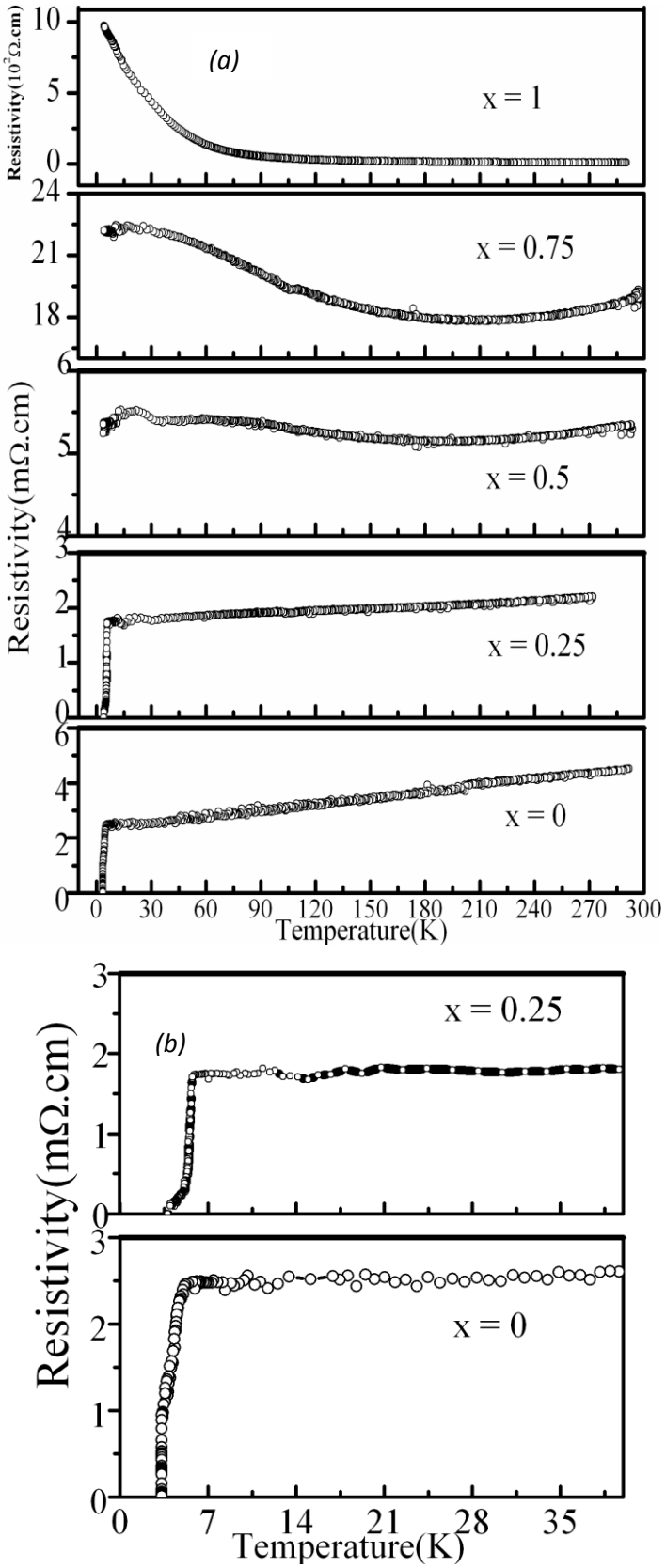

Figure 4.8 ***(a)*** *Resistivity vs. temperature plots for various* $Bi_{4-x}Ca_xO_4S_3$ *samples.* ***(b)*** *Resistivity vs temperature for* $Bi_{4-x}Ca_xO_4S_3$ *samples with x=0 and x=0.25 in the low temperature region.*

Table 4.2 *Comparative table of Transport parameters for the superconducting samples.*

Sample	Resistivity		AC Susceptibility		ρ_{rt}	ρ_0	RRR	Metallicity
	T_{onset} (± 0.5K)	T_{zero} (± 0.1K)	T_{onset} (± 0.05K)	T_{zero} (± 0.05K)	($m\Omega.cm$)			($\mu\Omega.cm/K$)
x=0	**4.9**	**3.3**	**4**	**3.3**	**4.5**	**2.3**	**1.96**	**0.8**
x=0.25	**5.8**	**3.7**	**4.3**	**3.5**	**2.2**	**1.5**	**1.28**	**1.6**

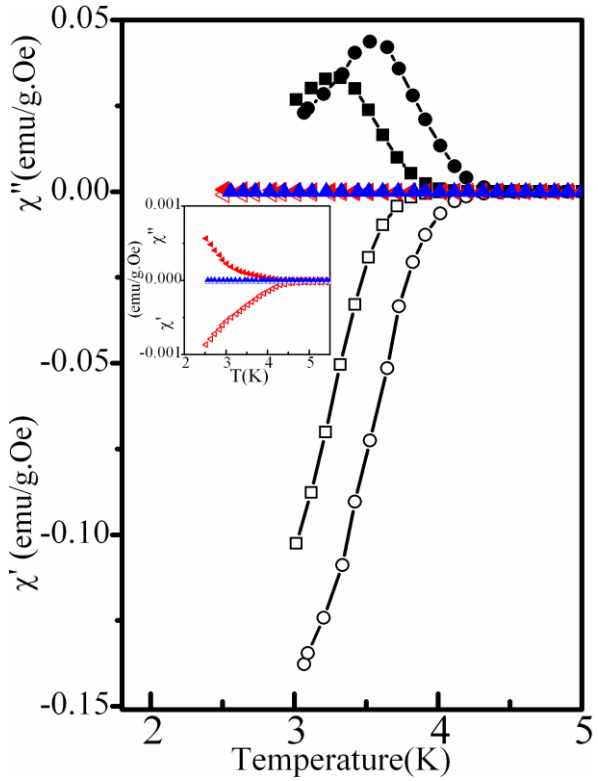

Figure 4.9 *AC susceptibility Vs Temperature plots for $Bi_{4-x}Ca_xO_4S_3$ samples with x= 0(□), x=0.25(○), x=0.5(◄), x=1(▲). And inset: shows low field data for x=0.5 and x=1 sample.*

4.3.4 Magnetization Studies

Figure 4.9 shows real and imaginary AC susceptibility variation with temperature for various samples under applied AC drive field of 10Oe. The peak in χ'' is associated with losses due to granular nature of the samples as observed in stoichiometric $Bi_4O_4S_3$ and CuO based superconductors [8, 9]. In a single phase superconductor loss peak in χ'' can represent

intrinsic losses due to the screening of magnetic fields by the superconducting surface currents. The loss is weakly dependent on temperature, magnetic field and frequency. The peak in χ'' in granular superconductor arises due to inter-granular weak links or Josephson junction coupling of adjacent superconducting grains. The height and width of this peak is strongly dependent on grain size distribution, temperature, and DC magnetic field history of the sample. This peak behaves like critical current density in polycrystalline superconductor. When the applied field exceeds H_{c1} then the loss peak is due to depinning of Abrikosov vortices, this peak is called intra-granular peak and is explained by Bean critical state model. The experimental data in figure 4.9 confirms the granular nature of the $Bi_{4-x}Ca_xO_4S_3$ ($0<x<1$) samples.

Since the applied field is low i.e. 10Oe, the observed peak in χ'' is predominant due to inter-granular weak link coupling of the grains. The intrinsic loss peak is not observed clearly. The T_c^{onset} and superconducting volume fraction increases with Ca doping. The T_c^{onset} for x=0 sample is 4.0K and the same for x=0.25 and x=0.5 is 4.3K and T_c^{zero} is increased from 3.3K to 3.5K for x=0.25. As the doping is increased to x= 0.5, broad transition due to poor grain connectivity (inserted in figure 4.9,) is observed and for this sample T_c^{zero}<2.5K. Sample with x=1 shows complete suppression of superconducting phase. These results are in good agreement with the transport data. The higher T_c observed for x=0.25 sample is due to strong Josephson coupling between superconducting grains giving rise to higher H_{c1} observed from *M-H* data

Isothermal Hysteresis loop at 2.5K for x=0 sample is shown in figure 4.10*(a)*. Lower critical field (H_{c1}) for this type-2 superconductor is calculated from the irreversible *M-H* data and the value is 16Oe. Low value of H_{c1} indicates small Meissonier region. Flux trapping at low fields is mainly due to the weak links present in the sample. Inter grain Critical current density (J_c) was calculated from hysteresis loop of x=0 according to Bean model using the following equation [10]

$$J_c=20(\Delta M/d), \text{ here } d=b\,[1-(b/3a)],\ a>b \qquad (4.1)$$

where ΔM (M^+-M^-) is the width of the *M-H* loop and *a*, *b* are sample dimensions. Figure 4.10 shows *M-H* loop for x=0 sample. The estimated J_c maximum at 2.5K is 736A/cm^2 and it decreases exponentially with applied magnetic field (Figure 4.10*(b)*). This exponential decrease in J_c is due to weak inter-granular coupling in the sample [11].

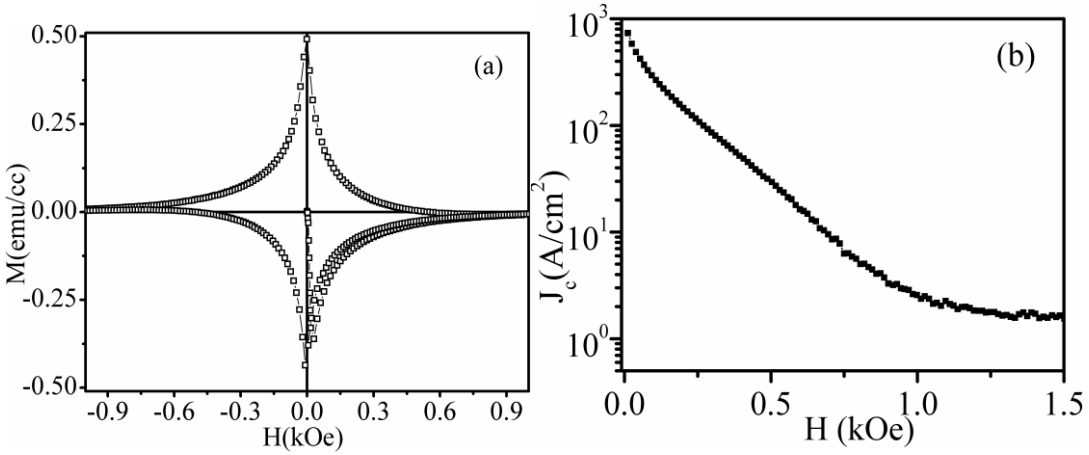

Figure 4.10 *(a) Hysteresis loop at 2.5K for x=0 sample, (b) Critical current density variation with field in x=0 sample at 2.5K.*

Figure 4.11*(a)* shows the irreversible symmetric hysteresis loops for x=0.25 sample at different temperatures. Increase in the hysteresis loop width with decrease in temperature is due to increase in the impurity phase and lattice defects, (observed through TEM images) thus results in increase in the critical current density of this sample (J_{cmax}=2854A/cm^2). The J_c variation with applied field at different temperature is shown in figure 4.11*(b)*.

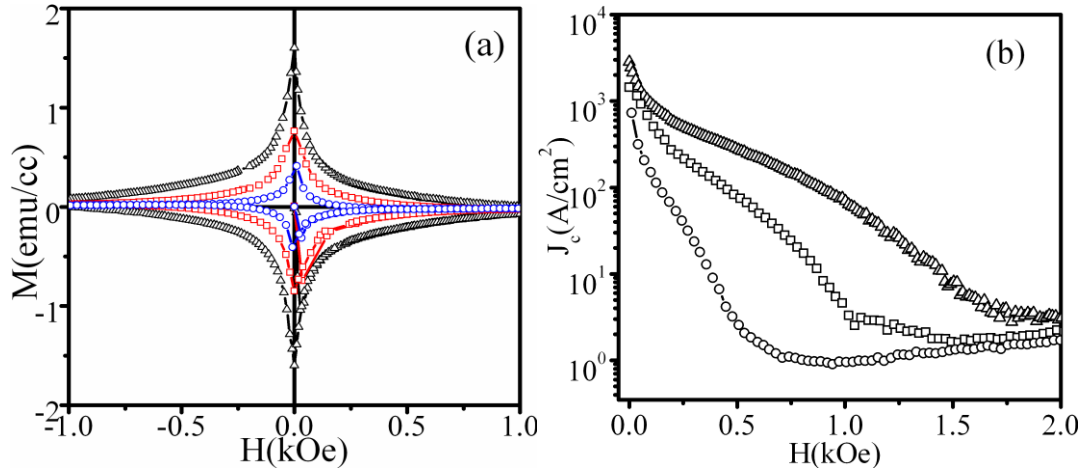

Figure 4.11 *M-H loops (a) and J_c (b) variation with field at different temperatures for x=0.25 sample. Here symbols representation follows as Δ = 2.5K, □=3K, ○=3.5K.*

Figure 4.12*(a)* clearly shows increase in the width of hysteresis loop in x=0.25 sample than x=0 sample, because of more flux trapping due to defects like dislocations, grain boundaries, and impurity phases. Figure 4.12*(b)* shows the increment in J_c due to x=0.25 Ca doping to almost three times of the value for un-doped sample. From microstructure analysis we have observed the increase in grain size, homogeneity and grain connectivity in x=0.25 sample as compared with un-doped (x=0) sample. This could be the

reason for high J_c in this material. In case of x=0 sample at low fields J_c decreases exponentially up to 100Oe, beyond this field J_c decreases in another exponential path in which the decrement rate is lower than that at low fields. In case of sample with x=0.25, J_c decreases exponentially up to 100Oe, beyond this J_c decreases slowly which is due to flux trapping by impurity phases and grain boundaries.

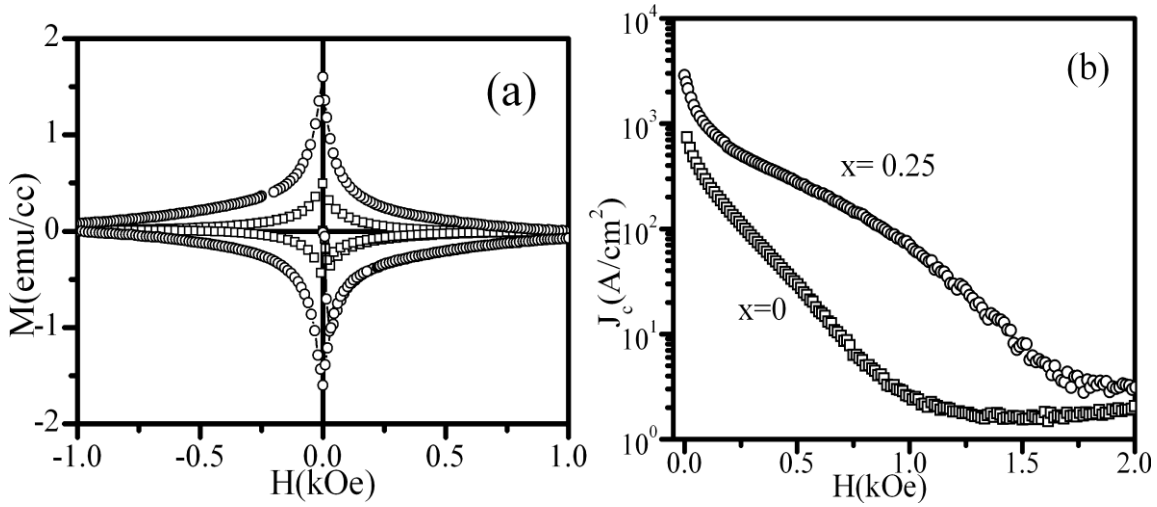

Figure 4. 12 *(a) Comparative hysteresis loops (a) and J_c (b) plots for x=0 (□-symbol) and x=0.25(○-symbol) samples at 2.5K.*

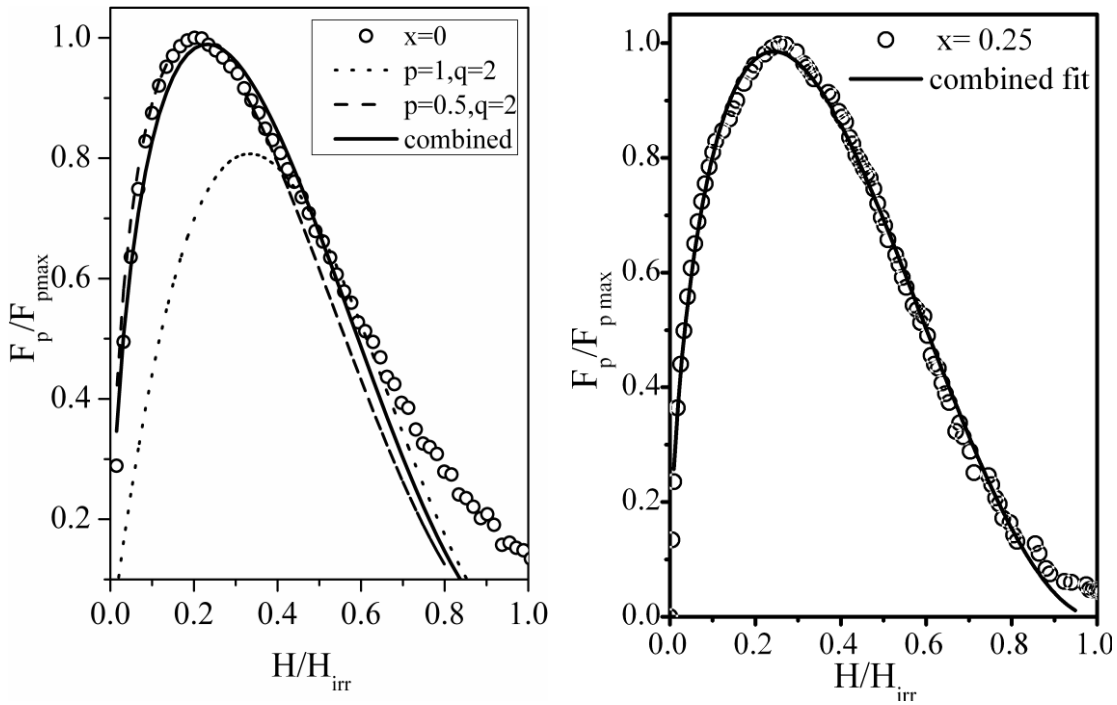

Figure 4.13. *Normalized pinning force response with reduced field for x=0 (a) and x=0.25 (b) sample. Solid line represents Kramer fit to the data.*

4.3.5 Pinning Mechanism

The Pinning mechanism in these samples is analyzed using Kramer scaling method [12]. According to this model the pinning force per unit volume is calculated using the equation $F_p=\mu_0 H\times J_c$, where $\mu_0=4\pi$x10^{-7}N/A^2. Figure 4.13 shows the normalized pinning force response with reduced field ($h=H/H_{irr}$) at 2.5K for un-doped sample and for Ca doped with x=0.25 sample. Reduced field maxima (h_{max}) is observed at 0.22 and 0.26 for x=0 and x=0.25 samples respectively. These values indicate the presence of normal core interaction with flux lattice line and pinning mechanism is mainly due to the impurity phases and grain boundaries as in the case of CuO based superconductors [13, 14].

Geometry of pinning centers in these samples is found by doing Kramer fit to the normalized pinning force vs. reduced field curve (figure 4.13) using the following equation

$$F(h) = A_s h^{p1} (1-h)^{q1} + B_p h^{p2} (1-h)^{q2} \qquad (4.2)$$

where, p, q values depend on the type of pinning centers and A_s and B_p are fitting parameters. According to Dew Hughes model, in case of pinning due to surface pinning centers p_1=0.5, and q_1=2 and in case of pinning due to point pinning centers p_2=1, and q_2=2 [15]. When there is more number of pinning centers present in the sample, then the normalized pinning can be written as the summation of all type of pinning centers [16].

Table 4.3 *comparison of J_c and Kramer fit parameters for the superconducting samples.*

Sample	J_{cmax} (10^3A/cm^2)	F_{pmax} (10^4 dyne/cm^3)	h_{max}	A_s (p=0.5,q=2)	B_p (p=1,q=2)
x=0	**0.8**	**3.0**	**0.22**	**2.64**	**1.85**
x=0.25	**2.85**	**14.2**	**0.26**	**2.5**	**2.0**

Comparative results on pinning mechanism for x=0 and x=0.25 samples are tabulated in table 4.3. Best fit to the normalized pinning force response with reduced field is observed with combination of both surface and point pinning centers using equation (4.2). In case of x=0 sample surface pinning domination over point pinning is confirmed through the combined fitting parameters, which are surface pinning coefficient A_s=2.64 and Point pinning coefficient B_p=1.85. Whereas in the case of x=0.25 sample, normalized pinning force data is well fitted with combination of Kramer surface and point pinning centers in the entire field range with the combined fit parameters A_s=2.50 and B_p=2.00. There is a

slight decrement in A_s and increment in B_p for x=0.25 sample over x=0. This may be due to bigger grain size and better homogeneity in x=0.25 sample over x=0 sample. Grain boundaries can act as surface pinning centers and impurity phases can act as point pinning centers. In x=0 sample at low fields surface pinning due to grain boundaries dominates whereas at high fields point pinning due to impurities dominates. In the case of x=0.25 sample pinning is due to both surface and point pinning centers in entire field range.

4.4 Chapter Summary

Bismuth Oxy Sulphide samples of composition $Bi_{4-x}Ca_xO_4S_3$ ($0<x<1$) were synthesized by solid state reaction method. The samples with x=0, 0.25 and 0.5 showed superconducting transition. The superconducting transition temperature T_c^{zero} increases with Ca doping of x=0.25. The sample with x=0.5 showed metal to semiconductor transition at ~150K with no significant change in T_c^{onset}. The sample with x=0.75 is not superconducting and showed semiconducting behaviour below 150K. The sample with x=1 showed strong semiconducting behaviour below 100K. These changes are ascribed to the disintegration of superconducting phase into other non-superconducting phases like Bi_2S_3. The change in structure as a function of Ca doping was analyzed through XRD, TEM, and FESEM. The XRD pattern showed increase in the intensity of Bi_2S_3 peaks with increase in Ca doping at the expense of decrease in the intensity of peaks corresponding to $Bi_4O_4S_3$ phase. The analysis of TEM images indicates the existence of mono crystalline Bi_2S_3 Nano particles in all the samples. The sample with x=0.25 shows increase in grain size and homogeneity and grain connectivity as well as increase in the impurity phases. For the samples with x=0.5, x=0.75 and x=1, superconducting grains were observed through TEM images. Disappearance of superconductivity in these three samples may be due to loss of grain connectivity and increase in the impurity phases. The lattice parameters calculated from SAED pattern show the large shrinkage in lattice parameters of Bi_2S_3, which confirms that Ca dopant is going into the interstitial positions of Bi_2S_3. With the increase in Ca doping, the disintegration of superconducting phase is observed from FESEM images. The estimated critical current density increases with Ca doping of x=0.25. This increment in J_c is attributed to the increase in the density of impurity phases that can act as pinning centers. The pinning mechanism follows scaling law with temperature in these samples. Kramer fit to the normalized pinning force response with reduced field confirms the presence of both surface and point pinning centers, where grain boundaries can act as surface pinning centers and impurity phases can act as point pinning centers in these samples.

References

[1]. Xian Zhang, Yufeng Liu, Ganghua Zhang, Yingqi Wang,Hui Zhang, and Fuqiang Huang, *ACS Appl. Mater. Interfaces,* **7**, 4442-4448, (2015).

[2]. Rajveer Jha and V. P. S. Awana, *Physica C*, **498**, 45-49 (2014).

[3]. S. G. Tan, P. Tan, Y. Liu, W. J. Lu, L. J. Li, B. C. Zhao and Y. P. Sun, *Eur. Phys. J. B*, **85**, 414 (2012).

[4]. Y. Liu, P. Tong, S.G. Tan, W. J. Lu, L. J. Li, B. C. Zhao, S. B. Zhang, and Y.P. Sun, *Physica B*, **412**, 119-121 (2013).

[5]. Z. Wang, Y. J. Song, H. L. Shi, Z. W. Wang, Z. Chen, H. F. Tian, G. F. Chen, J. G. Guo, H. X. Yang and J. Q. Li, *Physical review B*, **83**, 140505(R) (2011).

[6]. Rong Chen, Man Ho So, Chi-Ming Che and Hongzhe Sun, *J.Mater.Chem*., **15**, 4540-4545 (2005).

[7]. Xiaohu Huang, Youwen Yang,Xincun Dou, Yonggang Zhu, Guanghai Li, *Journal of Alloys and Compounds*, **461**, 427-431 (2008).

[8]. C. Candida, Silva, M. E. MaHenry, *IEEE Trans. Appl. Supercond*., **7**, 2 (1997).

[9]. Liyanawaduge, N. P. Singh, S. K. Kumar, Awana V. P. S., Kishan H., *J.Supercond.Nov.Magn*., **24**, 1599-1605 (2011).

[10]. A. M. Campbell and J. E. Evetts, *Adv. Phys*., **21,** 199 (1972).

[11]. R. Singh, J. *Phys. D, Appl. Phys.*, **22,** 1523-1527 (1989).

[12]. E. J. Kramer, *J. Appl. Phys*., **44,** 3 (1973).

[13]. Yamasaki H, Endo K, Kosaka S, Umeda M, Yoshida S, Kajimura K, *Phys.Rev.Lett*., **70**, 21 (1993).

[14]. Song L.W, Yang M, Chen E, Kao Y. H., *Phy Rev.B*, **45**, 6 (1992).

[15]. D. Dew-Hughes, *Philosophical Magazine*, **30**, 2, 293-305 (1974).

[16]. A. Crisan, V.S. Dang, G. Yearwood, P. Mikheenko, H. Huhtinen, P. Paturi, *Physica C*, **503**, 89-93 (2014).

CHAPTER 5

Studies on the composite system of glass-ceramic Bi-2212 and MgB_2 Superconductors

5.1 Introduction

Among the layer structured high transition temperature (T_c) superconductors, $Bi_2Sr_2Ca_{n-1}Cu_nO_{6+\delta}$ composition gives three different phases based on the number of CuO layers. Its T_c varies as 20K, 85K, and 110K with increase in n=0, 1, 2 respectively [1, 2]. The Bi-2212 phase formation through glass ceramic route leads to highly dense and pore free high T_c superconductor, thus enhancing the chances of practical applications of these materials [3]. Chemical doping of oxides and Nanoparticles addition/subtraction are, the most useful ways to improve the structural, mechanical and superconducting properties of high T_c superconductors, making them suitable for high temperature and magnetic field applications.

A lot of research is going on with the concept of addition of metal/superconductor to high T_c superconductors. The recent studies on addition of MgB_2 in Bi-2223 reported the regular improvement in superconducting and micro structural properties up to optimum doping level. Whereas the excess doping concentration forces these properties to decrease rapidly. In this composite system, MgB_2 Nano inclusions behave as the effective flux pinning centers in Bi-2223 leading to considerable increase in self field critical current density (J_c) [4]. Addition of MgO Nano particles to Bi-2212 resulted an increment in the flux pinning which lead to the increase in J_c [5]. Ce doping at Ca site in Bi-2212 resulted decrease in superconducting parameters because of hole filling mechanism as Ca^{+2} was replaced by Ce^{+4} [6,7], whereas Ce addition to Bi-2212 makes difference in Bi-2212 structure by replacing Cu atoms leading to degradation of structural and superconducting properties [8]. In most of the previous reports on pinning mechanism on Bi-2212 phase,

normalized pinning force data was not well fit to the entire reduced field range and most of the results are analysed considering presence of surface pinning centers in Bi-2212 [9-11].

Another layer structured MgB_2 superconductor has great importance because of its low cost and its applications in the area of superconducting wires and magnets [12]. MgB_2 mixing with high T_c superconductor was tried by several groups in order to increase the J_c. Addition of superconducting Nanoparticles of YBCO does not give better improvement in J_c of MgB_2 [13, 14]. The addition of oxides, in small amount, to MgB_2 does not change the superconducting phase formation but improves the J_C, irreversible field (H_{irr}), and upper critical field (H_{c2}). An improvement of pinning properties and the irreversibility field was expected by the addition of small particles due to enhanced grain boundary pinning. Here, in case of oxides addition, MgO and SiO_2 particles are dissolved in the MgB_2 grain structure or in the grain boundaries, thus pinning force is increased by about 10% with MgO particles addition to the MgB_2 [15]. Size of the additives also plays an important role in affecting the properties of the superconducting material. In case of addition of micro sized MgO particles to MgB_2, only interfaces can act as pinning centers. Whereas in case of Nano sized MgO inclusions in MgB_2, the MgO Nanoparticles themselves can act as flux pinning centers [16]. Small addition of Nano-ceria to polycrystalline MgB_2 resulted in a significant enhancement of the J_c. Despite the fact that polycrystalline samples are inhomogeneous and have randomly oriented grains, the introduction of Nano phase into the MgB_2 microstructure induces grain size reduction and improves grain connectivity, which has a direct impact on the flux pinning properties. The flux pinning force is enhanced with Nano CeO_2 addition to MgB_2 [17]. Addition of excess Mg improved the J_c in MgB2, here the inter particle region act as weak links (WLNS), whereas the addition of Nano-SiC and Nano-Ag particles degraded it [18]. The critical current density was enhanced significantly by adding B-2223 to MgB_2 [19]. Proximity effect near the interface of two different superconductors ($T_{c1} > T_{c2}$) affects the density of states of both superconductors [20].

Mixing of two high T_c superconductors is an emerging field in superconductivity to enhance critical current density. In this context we mixed Bi-2212 and MgB_2 layer structured high T_c superconductors in two different weight percentages. One sample with Bi-2212 as matrix and MgB2 as reinforcing material, (2:1) and the second sample with MgB_2 as matrix and Bi-2212 as reinforcing material (1:2). The composite samples show an increase in critical current density and decrease in irreversibility field. The flux pinning mechanisms in Bi-2212, MgB_2 and their composite systems are analysed.

5.2 Synthesis and Characterization Techniques

Bi-2212 glasses were prepared by melt quenching method. For Bi-2212 phase formation we have used Calcium rich Bi-4334 composition, which is optimum composition to get single phase of Bi-2212. Raw powders of Bi_2O_3, $SrCO_3$, $CaCO_3$, and CuO (99.99% pure) were weighed as per $Bi_4Sr_3Ca_3Cu_4O_{6+\delta}$ stoichiometry composition, and grinded thoroughly for 2hours using agate mortar and then calcined at 800^0C for 24hours. The reacted black powder was melted at 1000^oC in a platinum crucible and held at the same temperature for 10minutes to ensure thorough mixing and then it was quenched quickly between two copper blocks. The obtained shiny glasses of 0.5-1mm thickness were crystallized by sintering in air at 820^0C for 4days. These Bi-2212 glass ceramics were grinded for 1hour in air using agate mortar, then the resultant powder was mixed with commercially available MgB_2 (Sigma Aldrich, with purity>99%) in 1:2 and 2:1 weight ratios of Bi-2212 and MgB_2, respectively. The composite mixture was again grinded for one hour in normal atmosphere using agate mortar. The resultant composite powder was pressed into pellets at ambient conditions using hydraulic pressure unit. These composite pellets were used for different characterizations.

Crystalline nature and structure of the composite samples were characterized using x-ray diffraction technique and transmission electron microscopy. Surface morphology and grain distribution was observed using field emission scanning electron microscopy and composition analysis was done through energy dispersive spectra. Superconducting transition was observed by measuring magnetic moment with variation in temperature using physical property measurement system-vibrating sample magnetometer (PPMS-VSM). Magnetic moment response of the synthesized samples with applied field up to ±5T at a constant temperature (10K) was recorded using PPMS-VSM.

5.3 Results and Discussion

Figure 5.1 shows comparative X-ray diffraction pattern for the composite samples along with constituent compounds. Peaks were assigned using JCPDS software. XRD pattern for glass ceramic sample showed single phase of Bi-2212. MgB_2 sample showed well crystallized peaks of MgB_2 phase along with MgO impurity phase. In case of 1:2 composite sample XRD pattern showed MgB_2 as major phase and Bi-2212 as minor phase, whereas in case of 2:1 composite sample, XRD pattern confirms that Bi-2212 is major phase and MgB_2 is minor phase.

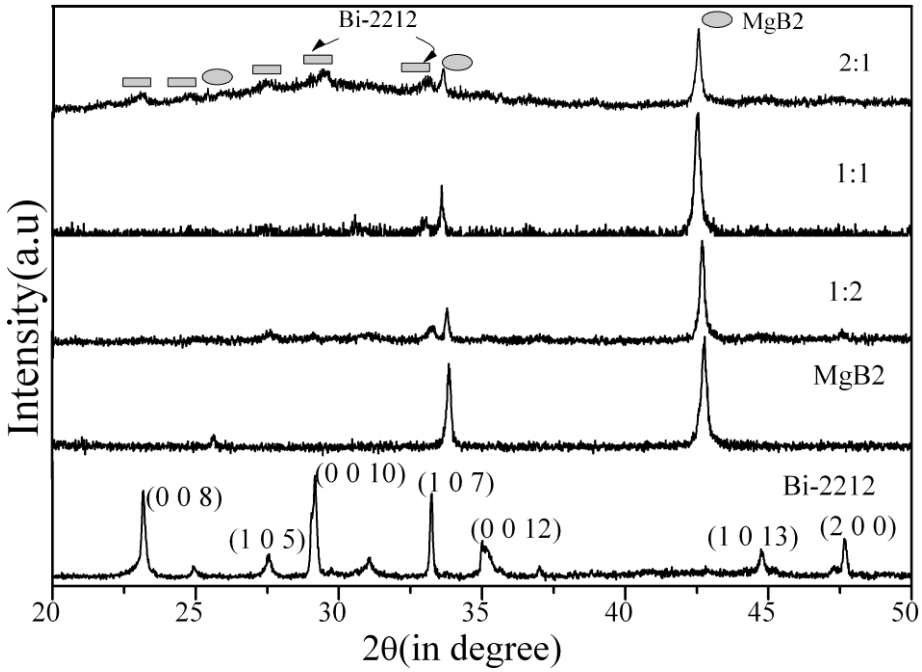

Figure 5.1 *XRD patterns for the samples*

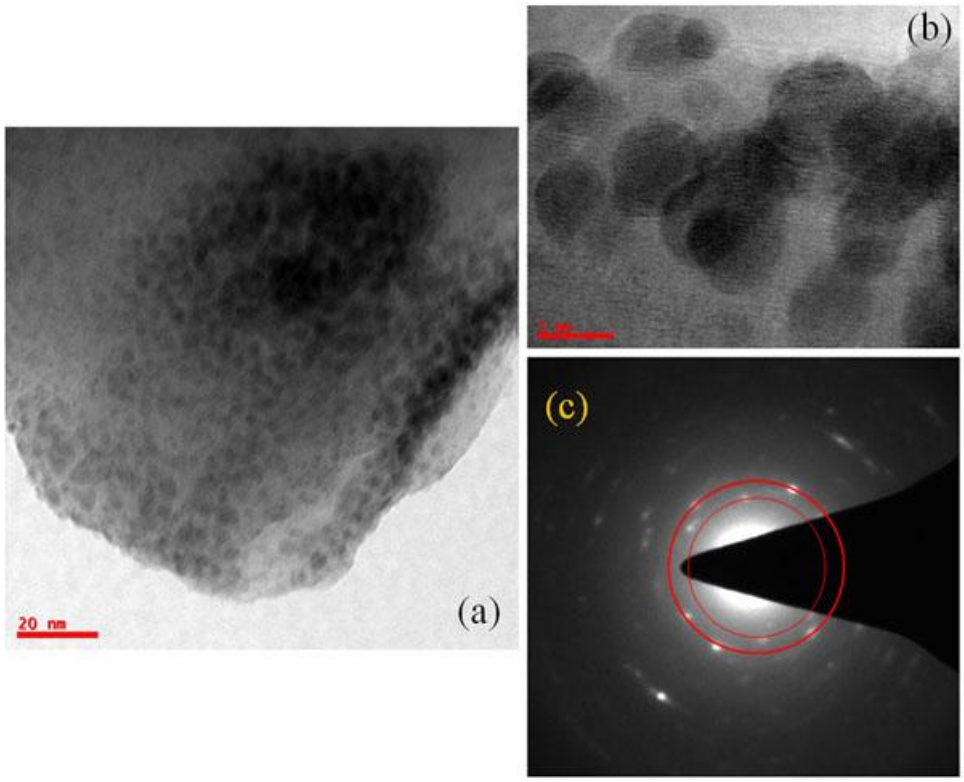

Figure 5.2 *TEM images for Bi-2212 glass ceramic. (a, b) HRTEM image (c) Diffraction pattern.*

From XRD pattern of the composite samples it is concluded that Bi-2212 and MgB2 remained separately and new peaks corresponding to mixed phase are not observed. Transmission electron microscopy results of the composite and individual samples of MgB_2

and Bi-2212 are shown in figure 5.2. Figure 5.2*(a)* shows the Nanoparticles of Bi-2212 phase. Fast Fourier transformation shows the diffraction points from the (1 0 3) lattice plane. Figure 5.2*(b)* shows the lattice fringes of (0 0 2) plane of Bi-2212 with *d*-spacing of 15.4A^{o}. Along with single crystalline Nanoparticles of Bi-2212 phase, Bi-2201 phase is also observed. In figure 5.2*(c)* the amorphous background in diffraction pattern confirms the glass phase of Bi-2201 and ring pattern joining through bright spots correspond to Bi-2212 superconducting phase [21].

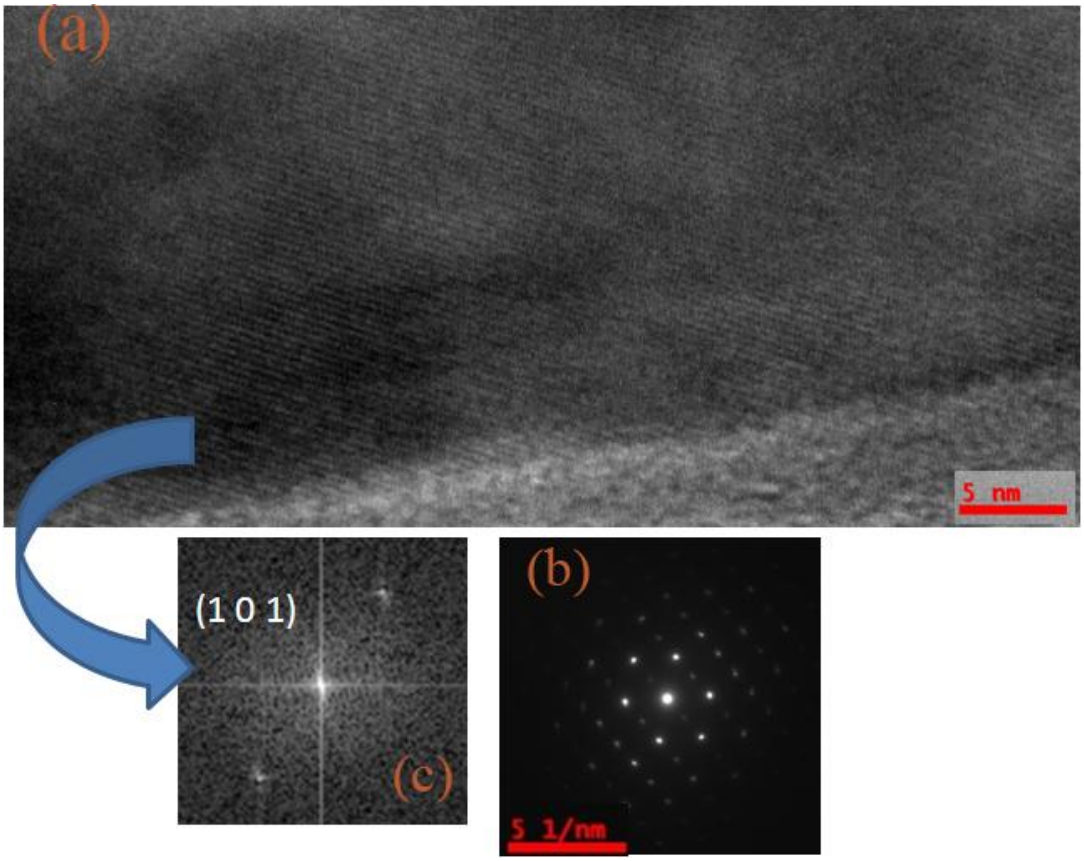

Figure 5.3 *TEM images for MgB_2. (a) HRTEM image for MgB_2 phase (b) Diffraction pattern (c) FFT of lattice fringes in (a).*

TEM images for MgB_2 sample are shown in figure 5.3. HRTEM image shows the lattice fringes corresponding to (1 0 1) plane of MgB_2 [22]. Diffraction pattern clearly shows that the hexagonal arrangement of lattice points in MgB_2.

Figure 5.4 shows TEM images for composition of two superconductors in 1:2 ratios. Figure 5.4*(a)* shows the mixed phase of the two different compositions. MgB_2 Nanoparticles along with Bi-2201 impurity phase are observed. The Bi-2212 phase is observed both in bulk and Nano size. Figure 5.5 shows the TEM images for composite samples of Bi-2212 and MgB_2 in 2:1 ratio. Figure 5.5(a) shows layer structure with lattice

spacing of 15.04A^{o} corresponding to (0 0 2) plane of Bi-2212. Figure 5.5*(b)* shows the presence of two phases in the composite sample. Two phases are shown with red circles. Circle *A* shows the lattice fringes corresponding to (0 0 1) plane of MgB_2 and circle *B* shows the lattice fringes corresponding to (1 0 5) plane of Bi-2212.

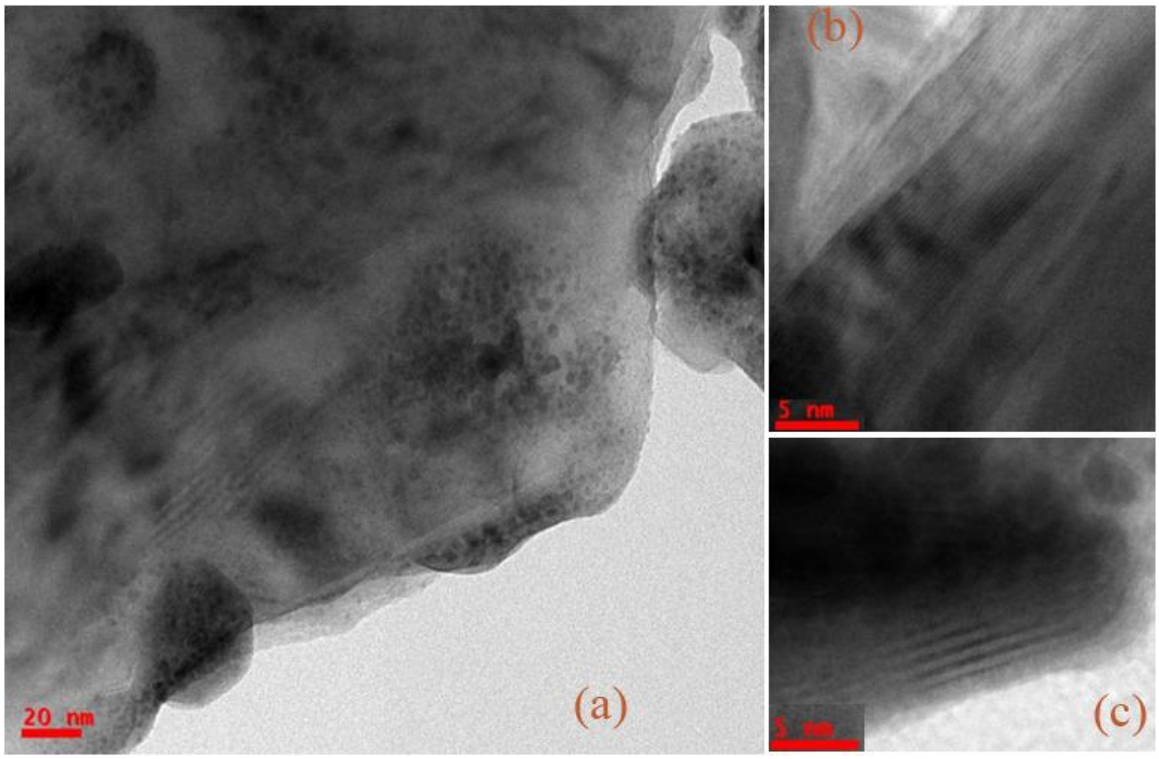

Figure 5.4 *(a) TEM images for 1:2 ratios (weight) of Bi-2212 and MgB_2. (b) and (c) shows lattice fringes corresponding to MgB_2 and Bi-2212 respectively.*

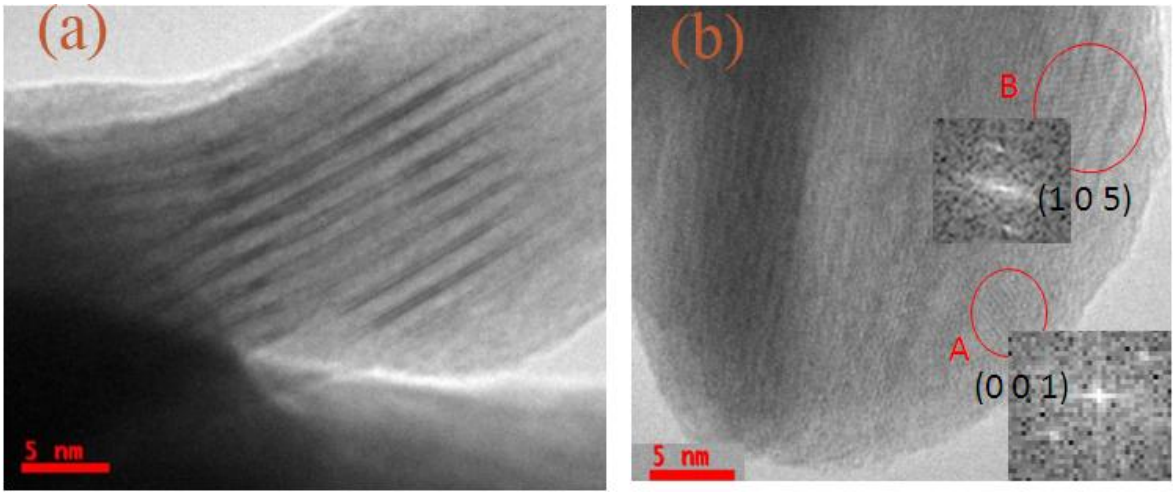

Figure 5.5 *TEM images for 2:1 ratio (weight) of Bi-2212 and MgB_2. (a) shows lattice fringes corresponding to Bi-2212 phase. (b) Shows the presence of lattice fringes corresponding to both phases in the composite sample.*

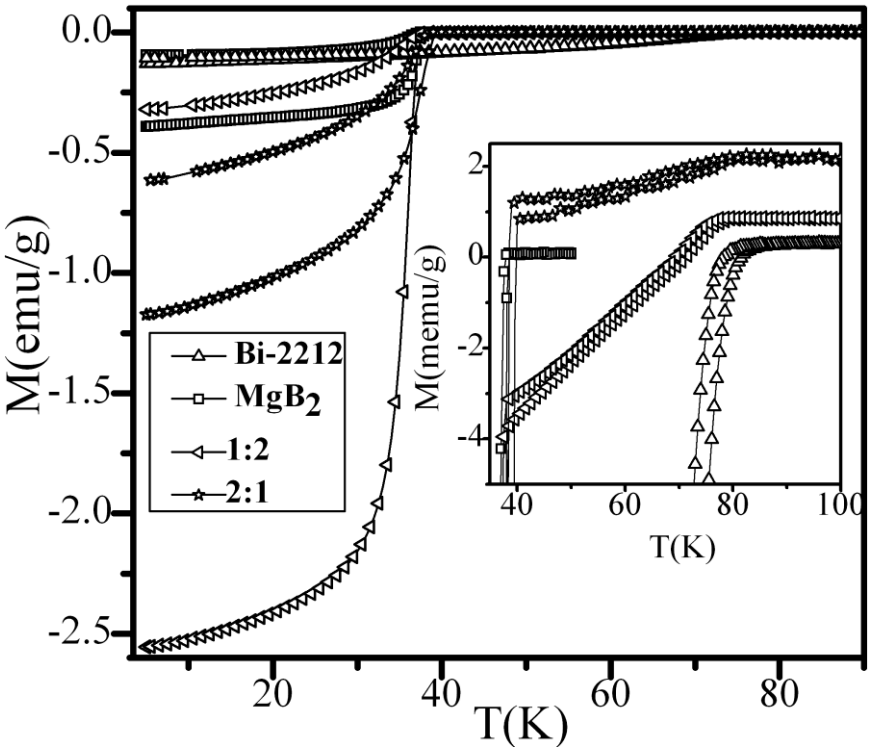

Figure 5.6 *Magnetization vs temperature plots for the samples.*

Figure 5.6 shows the magnetization *vs* temperature data of the samples in both field cooled and zero field cooled modes. In case of zero field cooled mode, the sample was cooled to 5K and data was taken while warming from 5K to 100K. In case of field cooled process, 20Oe field was applied on the sample and then cooled to 5K. Data was taken while warming from 5K to 100K. Figure 5.6 shows the superconducting transition at 80K and 39K, which corresponds to individual Bi-2212 and MgB_2 samples respectively. Figure 5.6 clearly shows that the composite samples show two superconducting transitions one is at 80K, which corresponds to Bi-2212 phase and second transition at 39K, which corresponds to MgB_2 phase. Enlarged view of superconducting onset is shown in inset of figure 5.6. The superconducting volume fraction is increased in composite samples.

Hysteresis loops at 10K for the samples are shown in figure 5.7. The flux trapped in the superconductor is observed through the width of these hysteresis loops. Asymmetry is also observed in all the hysteresis loops. At temperatures higher than ~10K the high field *M(H)* dependence of high T_C superconductors have a pronounced asymmetry with respect to M=0 axis, so the main parts of hysteretic loops fall in the second and fourth quadrants. This asymmetry grows with temperature. The asymmetric *M(H)* dependencies were described as due to the surface and volume super currents, which together lead to the total

magnetization. Asymmetry in porous and textured system hysteresis loops was explained with the extended variant of critical state model.

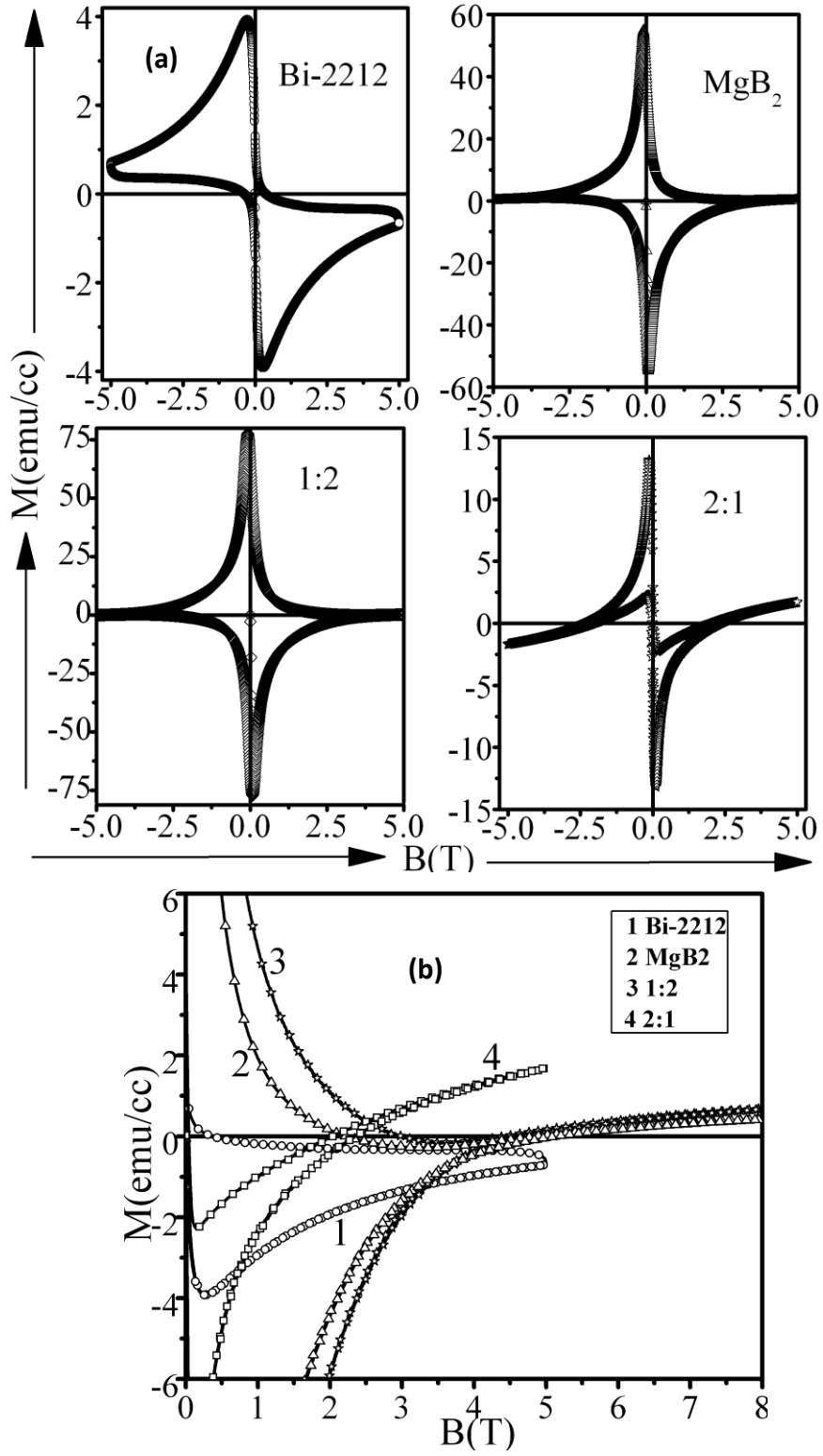

Figure 5.7 *(a) Magnetization hysteresis loops at 10K for various samples. (b) Enlarged view of hysteresis loop closing of the samples.*

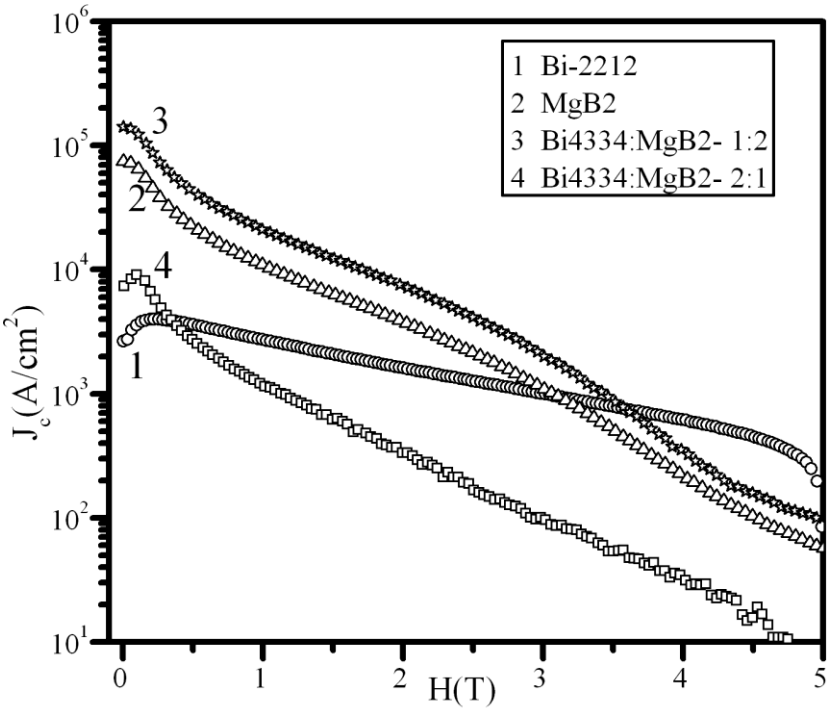

Figure 5.8 *J_c variation with field in the samples.*

According to this model, *M(H)* dependence of the sample consisting of sufficiently small superconducting granules should be fully reversible at all temperatures. However, asymmetry is due to inhomogeneous distribution of magnetic field and pinning force in the superconductor. In case of small granular superconductors demagnetizing effects are very small and the irreversibility due to volume pinning is much smaller than plate like Nano-crystal superconductors. Asymmetric hysteresis loops are mainly due to the disorder and high density of impurities [23, 24]. Paramagnetic behaviour at high fields (figure 5.7*(b)*) in MgB_2 and MgB_2 added Bi-2212 samples are owing to the superposition of strong paramagnetic background of MgB2. Similar behaviour was observed in case of Ho_2O_3, TiO_2 doping in MgB_2 superconductor [25-27]. The critical current density is calculated for the composite and individual samples using magnetic hysteresis loops of rectangular slab type samples. From the hysteresis loops that the flux trapping at low fields and fast flux creeping at high fields were observed. The J_c was calculated according to Beans extended critical state model [28] using the following equation

$$J_c=20(\Delta M/d) \tag{5.1}$$

Here $d=b[1-(b/3a)]$, $a>b$, ΔM (M^+-M^-) is the width of the *M-H* loop and *a, b* are sample dimensions. Field dependence of J_c at 10K for the composite samples is shown in figure 5.8, J_c has increased in composite samples comparatively with the constituent materials.

The variation in J_c values in self-field and at 4T for the composite samples and constituents of composites are given in table 5.1. From this table we can understand that in 1:2 composite sample, increase in J_c and stability of J_c at higher fields observed due to the reinforcing property of Bi-2212 in MgB_2 matrix. The high J_c in composite samples is attributed to the presence of glass ceramic inclusions in MgB_2 matrix, which act as flux pinning centers. In case of 2:1 composite sample the fast decrease in J_c is attributed to the reinforcing property of MgB_2 in Bi-2212 matrix.

Table 5.1 *Comparative table for composite and constituents of composite systems*

	J_c(zero) (A/cm^2)	J_c(4T) (A/cm^2)	F_p (N/CC)	h_{max}
Bi-2212	0.02×10^5	0.99×10^3	0.3×10^8	0.23
MgB2	0.7×10^5	0.1×10^4	1.1×10^8	0.15
1:2	1.4×10^5	0.2×10^4	2.1×10^8	0.15
2:1	0.07×10^5	0.94×10^2	0.13×10^8	0.15

Pinning force per unit volume is calculated using the equation $F_p = \mu_0 H \times J_c$, where $\mu_0 = 4\pi \times 10^{-7}$ N/A^2. Pinning force is increased in composite samples, is shown in figure 5.9. In superconductors, pinning force mainly depends on the type of interactions, geometry and properties of pinning centers. Pinning force is nothing but the strength of the interaction between flux line lattices (FLL) with pinning centers (PC). Figure 5.9, shows that the pinning force is zero at B=0, passing through at least one maxima and returning to zero at H_{c2} (where J_c=0), which is a universal feature in all hard superconductors [29]. There are two types of pinning centers and two types of interactions are possible as explained by Dew-Hughes. One is due to the superconducting pinning centers, in this case the difference between the properties of FLL and PC will be less and the pinning will be weak and this type of pinning mechanism is called Δk pinning, which is due to small change in Ginzburg-landue parameter (k), which is arising from the changes in normal state resistivity because of random distribution of dislocations. Second one is due to normal metal or insulating pinning centers, in this case the difference between the properties of FLL and PC will be high leading to strong pinning and it is called normal pinning. If the

size (*a*) and shape (*l*) of the pinning center is greater than penetration depth (λ) then the induction field (*B*) is able to adjust to equilibrium value everywhere and this value is different in pins from that of in matrix. This difference will lead to barrier to flux motion at the interface between pin and matrix, which is cause of pinning. This type of pinning is called Δl pinning, which is due to magnetic interaction. If the value of *a* or *l* is less than λ then the induction cannot adjust to equilibrium value it will have some average value. In this case Gibbs free energy of flux lines will be different at pinning centers and matrix due to difference in superconducting properties. This type of interaction is called core interaction.

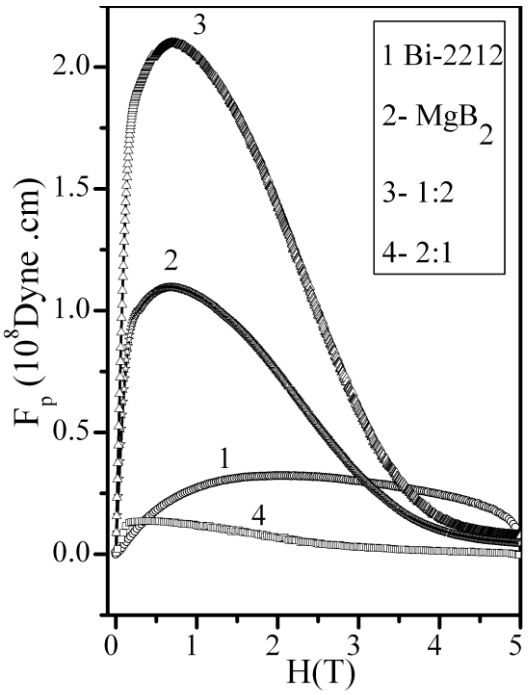

Figure 5.9 *Pinning force vs field Plots.*

According to Dew–Hughes considerations three types of pinning centers with different dimensions are possible. Pins with lower dimensions than inter flux line spacing (*d*) are called point pinning centers. Pins with two dimensions greater than *d* are called surface pinning centers and pins with all dimensions greater than *d* are called volume pinning centers. Figure 5.10 shows the normalized pinning force response with reduced field ($h=H/H_{c2}$) at 10K for the samples. Most characteristic feature of this curve is its maxima, which will be different for different pinning functions. Reduced field maxima (h_{max}) for glass ceramic Bi-2212 is observed at 0.33 (figure 5.10*(a)*). Pinning mechanism in this sample is mainly due to normal and core point pinning centers. Geometry of the pinning

centers was found by doing Kramer fit to the normalized pinning force curve. According Kramer model [30], pinning force function is given as

$$F(h) = F_p/F_{pmax} = C(H_{c2}(T))^2 h^p (1-h)^q \quad (5.2)$$

Here c is constant, $h=H/H_{c2}$, p and q are $p=0.5$ *and* $q=2$ for normal core surface pinning, $p=1$ *and* $q=2$ for normal core point pinning and $p=1$ *and* $q=1$ for superconducting core volume pinning. Low field data of normalized pinning force response to the reduced field for glass ceramic Bi-2212 sample showed good fit with the combination of Kramer surface and point pinning mechanism (equation (5.3)), whereas high field data is well fitted with volume pinning mechanism. Best fit (0.999%) to the normalized pinning force in the entire reduced field range was observed with the equation showing summation of surface, point and volume pinning centers (equation (5.4)).

$$F(h) = A_s h^{0.5} (1-h)^2 + B_p h (1-h)^2 \quad (5.3)$$

$$F(h) = A_s h^{0.5} (1-h)^2 + B_p h (1-h)^2 + C_v (h (1-h)) \quad (5.4)$$

here A_s, B_p, C_v are fitting parameters, p and q values vary depending on the type of pinning centers. For comparative study of pinning mechanism in Bi-2212, we have also studied pinning mechanism in Bi-2212 synthesized by solid state reaction method. In this case volume pinning dominates over surface and point pinning mechanisms (figure 5.10*(b)*).

The h_{max} is observed for powder ceramic Bi-2212 sample at 0.5 which indicates superconducting core volume pinning. At low reduced fields, surface pinning more dominant (up to h=0.1), with h_{max}=0.22. Above this field, point pinning dominates up to the reduced field of h=0.25 with h_{max}=0.33. Above this field, volume pinning is more dominating. Best fit (0.999%) is observed with equation (5.4), which shows combination of all the three (point, surface and volume) pinning mechanisms. Our results are in good agreement with the theoretical prediction by Dew-Hughes. More than one type of pinning centers in one system may be due to the nucleation of precipitant at nodes of a pre-existing dislocation structure or establishment of a cell structure whose nodes coincide with previously formed precipitants. This could give rise to mixture of point, surface and volume pinning with a broad peak extending from h=0.33 to h=0.6 [27].

Pinning mechanism in bulk MgB_2 is analysed by doing Kramer fit to the normalized pinning force response to the reduced field. Figure 5.10*(c)* shows the best fit (0.999%) is observed with the equation showing combination of Kramer surface and point pinning centers (equation (5.3)). The h_{max} for this sample is observed at 0.15 indicating the surface

pinning due to grain boundaries along with point pinning due to impurities. The normalized pinning force response to the reduced field for the composite samples is shown in figure 5.10*(d)*. The reduced field maxima (h_{max}) is observed at 0.15 and it is independent of composition implying that the dominating pinning mechanism is same for all samples.

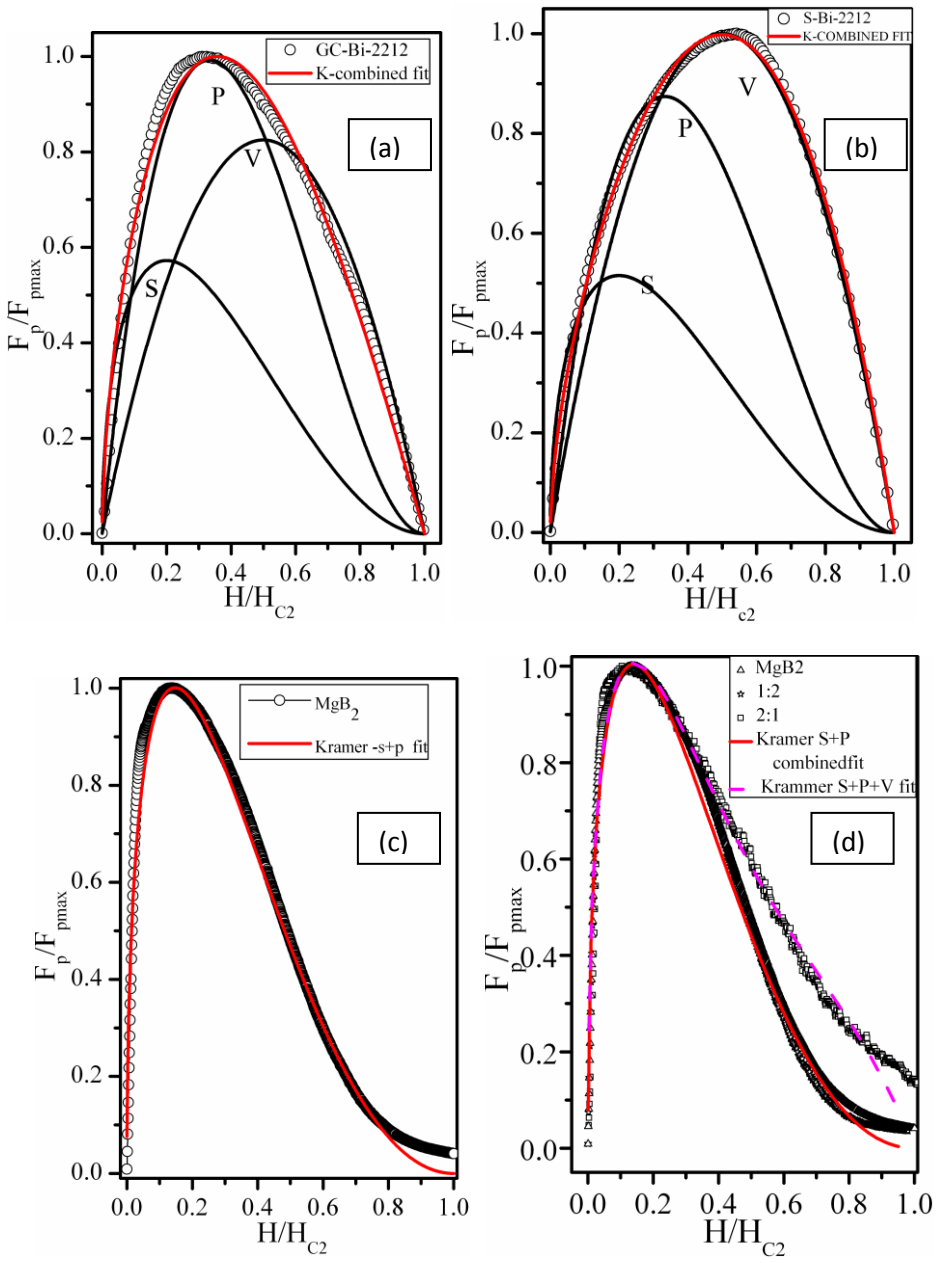

Figure 5.10 *Normalized pinning force vs reduced field for (a) Glass ceramic Bi-2212, (b) powder ceramic Bi-2212, (c) MgB_2 and (d) composite, S-surface, P-point, V-volume pinning fit. Red colour line is fit by equation (5.3) and pink line is fit by equation (5.4).*

Normalized pinning force follows the scaling law with combination of Kramer surface and point pinning mechanism in 1:2 composite sample (red curve in figure 5.10*(d)*). In case of 2:1 composite sample best fit (pink curve in figure 5.10*(d)*) is observed with

equation (5.4), confirming the presence of surface, point and volume pinning centers as in the case of Bi-2212 glass ceramic. Our results are in good agreement with earlier reports on composite system of Bi-2212 powder ceramic and MgB_2, in which h_{max} is observed at 0.17 [31]. Low values of h_{max} for composite samples indicate the random orientation of grain boundaries in the sample and also consistent with the theoretical prediction that the repulsive pins are less effective in pinning than attractive pins. Here repulsive pins are inclusions of material with higher T_c than matrix. This type of pinning centers enhance the order parameter, causing the maximum superconducting volume fraction in the composite samples.

5.4 Chapter Summary

In summary, composite system of glass ceramic Bi-2212 superconductor and MgB_2 superconductor were prepared at an ambient conditions and observed an increment in critical current density (J_c). We synthesized Bi-2212 superconductor by both glass ceramic route and solid state methods. The composites of the glass ceramics Bi-2212 and MgB_2 in 1:2 and 2:1 weight ratios were synthesized. Glass ceramic inclusions are observed in bulk MgB_2 through high resolution TEM images of the composite samples. These morphological and structural changes in composite samples are in good correlation with magnetization observations. Magnetization vs temperature data showed superconducting transitions at two temperatures, one at 80K corresponding to Bi-2212 phase and the second transition at 39K corresponding to MgB_2 phase. Critical current density and pinning force are increased in composite systems by 10 times when compared to that of individual sample. Pinning mechanism in glass ceramic Bi-2212, powder ceramic Bi-2212 and MgB_2 is analyzed in details. In case of Bi-2212 glass ceramic, point pinning is more dominating, whereas in powder ceramic of Bi-2212, volume pinning is more dominating. However, in both the samples all three i.e. point, surface and volume pinning centers are present. In MgB_2, pinning mechanism is well explained by considering both surface and point pinning centers. The pinning mechanism in composite sample is same as in MgB_2. Normalized pinning force data is well fitted with combination of Kramer surface and point pinning centers. Reduced field maxima are observed at 0.15 for composite samples. Low value of h_{max} for composite samples indicates the random orientation of grain boundaries in the composite samples.

References

[1]. H. Maeda, Y. Tanaka, M. Fukutomi, T. Asano, *Jpn. J. Appl. Phys.*, **27,** L209-L210 (1988).

[2]. J. M. Tarascon, W. R. McKinnon, P. Barboux, D. M. Hwang, B. G. Bagley, L. H. Greene, G. W. Hull, Y. LePage, N. Stoffel, and M. Giroud, *Phy. Rev. B,* ***38,*** 13 (1988).

[3]. E. Zacharias, and R. Singh, *Physica C*, **247,** 221-230 (1995).

[4]. M. Dogruer et.al, *Journal of alloys and compounds*, **556**, 143-152 (2013).

[5]. F. Jordan, O. Pna, R. Horyn, *Physica C*, **235-240**, 945-946 (1994).

[6]. D. Rama sita and R. Singh, *Solid State Communications*, **94,** 12, 969-972 (1995).

[7]. S. Bal, M. Dogruer, G. Yildirim, A. Varilci, C. Terzioglu, Y. Zalaogl, *J. Supercond*. Nov. Magn., **25**, 847-856 (2012).

[8]. W. Wei, J. Schwartz, K. C. Goretta, U. Balachandran, A. Bhargava, *Physica C,* **298,** 279-288 (1998).

[9]. J. M. Gonzalez-Calbet et al., *Physica C,* **203,** 223-230 (1992).

[10]. H.Yamasaki et al., *Phy. Review. Lett.,* **70,** 21 (1993).

[11]. P. Fabbricatore et al., *Phy. Rev. B*, **54,** No.17 (1996).

[12]. Jun Nagamatsu, Norimasa Nakagawa, Takahiro Muranaka, Yuji Zenitani and Jun Akimitsu, *Nature*, **410,** 43-63 (2001).

[13]. Y.Y. Xu, J. Ren, S. H. Han, and H. Zhang, *International Journal of Modern Physics B*, **21,** 18&19, 3352-3354 (2007).

[14]. X. F. Rui, X. F. Sun, X. Xu, L. Zhang, and H. Zhang, *International Journal of Modern Physics B*, **99,** 1-3, 375-377 (2005).

[15]. Olaf Perner, Wolfgang Habler, Jurgen Eckert, Claus Fischer ,Christine Mickel, Gunter Fuchs, Bernard Holzapfel and Ludwig Schultz, *Physica C*, **432,** 15-24 (2005).

[16]. D. Tripathi, T. K.Dey, *J. Supercond. Nov. Magn,* **28,** 2025-2032 (2015).

[17]. C. H. Jiang et al., *Physica C,* **423,** 45-50 (2005).

[18]. M. Gharaibeh et al., *Journal of Applied Physics*, **107**, 063908 (2010).

[19]. P. P. S. Bhadauria et al., *Journal of Applied Physics*, **113**, 063908 (2013).

[20]. V. Cherkez et al., *Physical review X*, **4**, 011033 (2014).

[21]. R. M. Hazen et al., *Physical Review Letters*, **60,** No 12, 1174-1177 (1988).

[22]. Ye Zhu, MrekNiewczas, Martin Couillard, Gianluigi A. Botton, *Ultra microscopy*, **06,** 1076-1081 (2006).

[23]. D. M. Gokhfeld, D. A. Balaev, M. I. Petrov, S. I. Popkov, K. A. Shaykhutdinov and V. V. Val'kov, *Journal of Applied Physics*, **109**, 033904 (2011).

[24]. D. X. Chen, R. B. Goldfab, R. W. Cross and A. Sanchez, *Physical Review B,* **48,** 8, 6426-6429 (1993).

[25]. D. C. Larbalestier, L. D. Cooley, M. O. Rikel et al., *Nature*, **410,** 186-189 (2001).

[26]. C. Cheng and Y. Zhao, *Physica C*, **463-465,** 220-224 (2007).

[27]. V. G. Prokhorov et al., *Supercond. Sci. Technol*., **22,** 045027 (2009).

[28]. D. X. Chen, R. W. Cross and A. Sacnchez, *Physica C*, **33,** Issue 7, 695- 703 (1993).

[29]. D. Dew-Hughes, *Philosophical Magazine*, **30:2,** 293-305 (1974).

[30]. E. J. Kramer, *J. Appl. Phys*., **44,** No.3, 1360-1370 (1973).

[31]. T.M.Shen et al, *Supercond.Sci.Technol*., **18,** L49-L52 (2005).

CHAPTER 6

Hetero structures of Glass Ceramic Bi-2212 and MgB_2 Superconductors

6.1 Introduction

Hetero structures of superconductors with metal, insulator semiconductors and superconductors are being studied in recent years. Hetero structures of two superconductors are interesting in view of their applications. Structural and chemical compatibility between oxide matrix and pinning phase enables strong vortex pinning and opens up the possibility of growing superconducting super lattice structures. Multilayer growth method enhances the possibility of high field applications with high critical current density (J_c) in all configurations. Anisotropy in J_c, defined as the ratio of J_c parallel to the *ab* plane (J_c^{ab}) and J_c parallel to the *c*-axis (J_c^{c}), decreased in artificially engineered super lattices of Pnictides [1] and YBCO [2, 3].

In this chapter, we present the artificial pinning engineering through formation of Hetero structures of Bi-2212 and MgB2 superconductors. Bulk multi layers of Bi-2212 and MgB_2 superconductors are prepared through hydraulic pressure unit at an ambient conditions. The structural and magnetic properties of the synthesized samples are discussed.

The high T_c BiSCCO-2212 superconductor has complex unit cell structure, in which some of the atoms form Oxygen deficient perovskite like structure while other appears to be in rock-salt structure. The diverse physical properties of materials in the perovskites and related compounds make this family a good choice for assembling Hetero-structures and for studying and exploiting interfacial phenomenon. Superconducting superlattices of Bi-2212 with various number of Bi-2201 were studied extensively by Eckstein et al [4] and concluded that the pairing interaction, responsible for the high-T_C superconductivity, is essentially two dimensional, very little coupling between adjacent high T_c unit cells is necessary for the formulation of the superconducting condensate. The superlattices of YBCO and non-superconducting PBCO resulted in reduced superconductive transition

temperature because of parasitic effects in YBCO [5]. Multilayer growth of NbN on top of Nb layer resulted in enhancement of effective first penetration field of Nb layer compared to single Nb layer [6].

6.2 Experimental Techniques

We have prepared bi-layer and tri-layer Hetero structures of Bi-2212 and MgB_2 layered superconductors, the schematic of these samples is shown in figure 6.1. Bi-2212 superconductors were prepared through Glass ceramic route as described in earlier chapter. The glass ceramics were grinded for one hour in air using agate mortar then the resultant powder was pressed into pellet at ambient conditions using hydraulic pressure unit. On top of it we made a pellet of MgB_2 at the same pressure. The thickness of MgB_2 layer is ~0.5mm (this sample is named as Hetero-1) in the series. Another bi-layer sample with MgB_2 layer thickness of 0.4mm is prepared and named as Hetero-2.

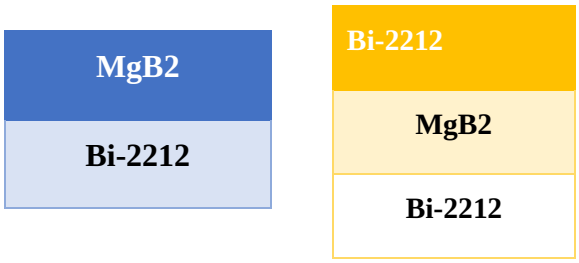

Figure 6.1 *Schematic of bi-layer ant tri-layer samples*

Tri layer samples were prepared with Bi-2212 glass-ceramic as top and bottom layers and MgB_2 as middle layer. Two tri-layer samples were prepared with 0.7mm and 0.6mm of MgB_2 layer thickness and named as Hetero-3 and Hetero-4 respectively. To check the crystalline structure the X-Ray diffraction (XRD) patterns of the sample was recorded using powder X-ray diffractometer (Bruker) with Cu-k_α radiation. Superconducting phase identification was done by *dc* magnetization measurement of the samples, using physical property measurement system (PPMS). Surface morphology and phase separation was observed through Field emission scanning electron microscopy (FESEM) and Transmission electron microscopy (TEM). Hysteresis loops for the samples at 10K were recorded using PPMS.

6.3 Results and Discussion

The X-ray diffraction patterns for the synthesized Hetero-structure samples are shown in figure 6.2. Peak assignment to Bi-2212 phase was done using JCPDS. The presence of both Bi-2212 and MgB_2 major phases along with small amount of Bi-2201 impurity phase are clearly noticed. Broad peaks along with satellite peaks at high angles confirm the super lattice structure of bulk multilayer samples.

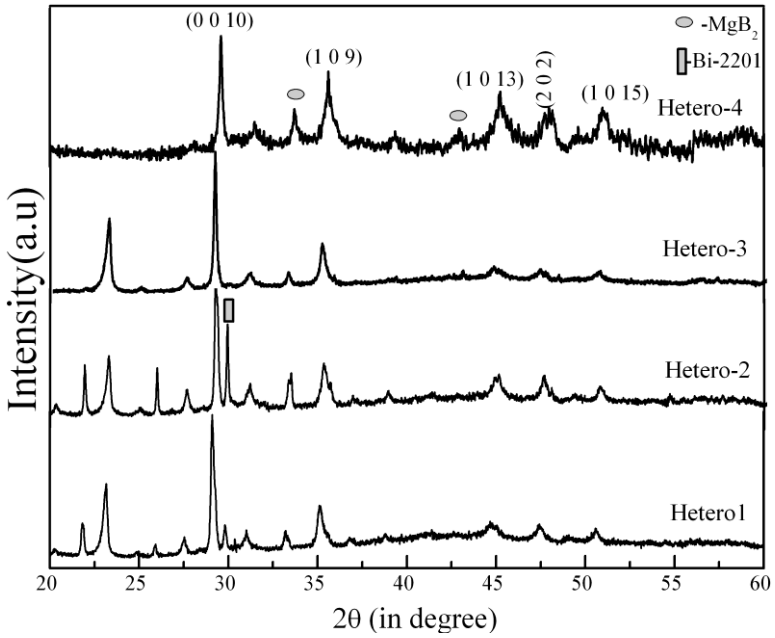

Figure 6.2 *XRD pattern for the various samples.*

Morphology of the samples is observed at surface and interfaces of the layers through FESEM images of the samples (from figure 6.3 to 6.5). Figure 6.3 shows interface of Hetero-1 sample at different magnifications. From these images one can observe low porosity and good adherence at the interface of Bi-2212 and MgB_2 layers. Well crystallized grains were observed in both the layers. Figure 6.4 shows FESEM images at the interface of Hetero-2 sample at different magnifications. From these images one can observe increase in porosity at the interface in Hetero-2 sample when compared to Hetero-1. Well crystallized spherical grains of MgB_2 and platelet like structured grains of Bi-2212 are observed clearly in these images. Figure 6.5 shows FESEM images for Hetero-3 sample, in which one can observe three layers clearly and one of the interfaces is shown at different magnifications. From these images one can observe high porosity and impurity phase accumulation at the interfaces of the Bi-2212 and MgB_2 layers in Hetero-3 sample. Surface

morphology, and phase identification was done through FESEM images for cross section of the Hetero-4 sample and shown in figure 6.6.

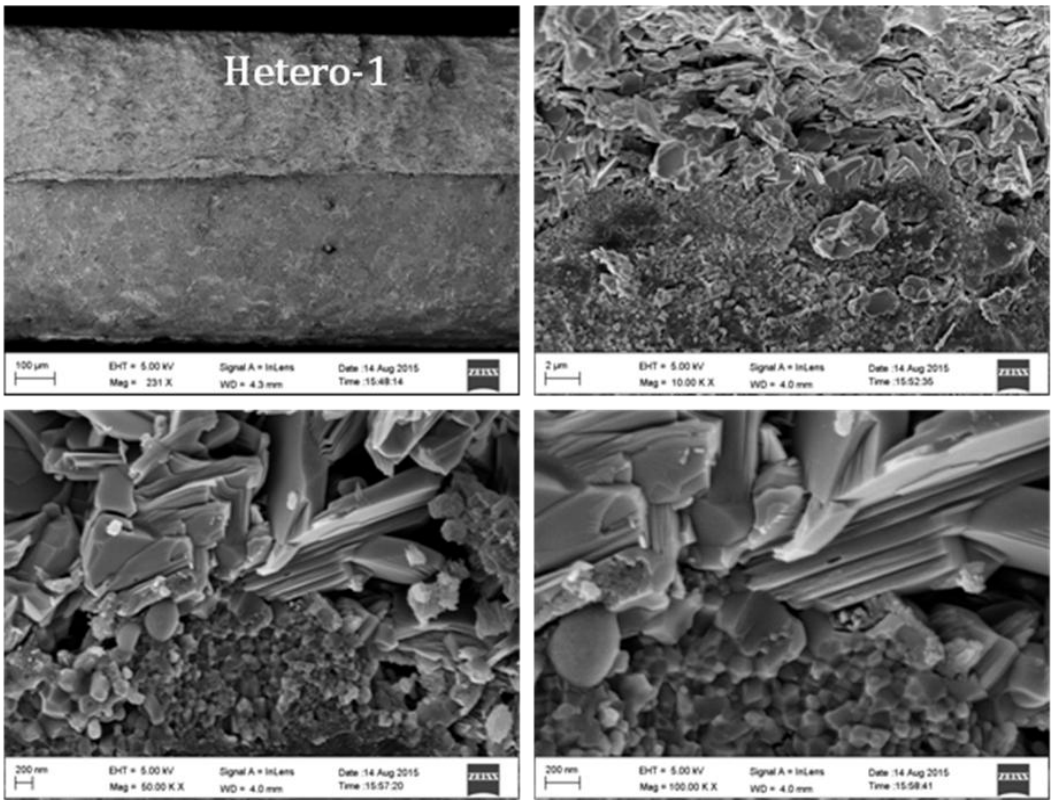

Figure 6.3 *FESEM images for Hetero-1 sample at different scales.*

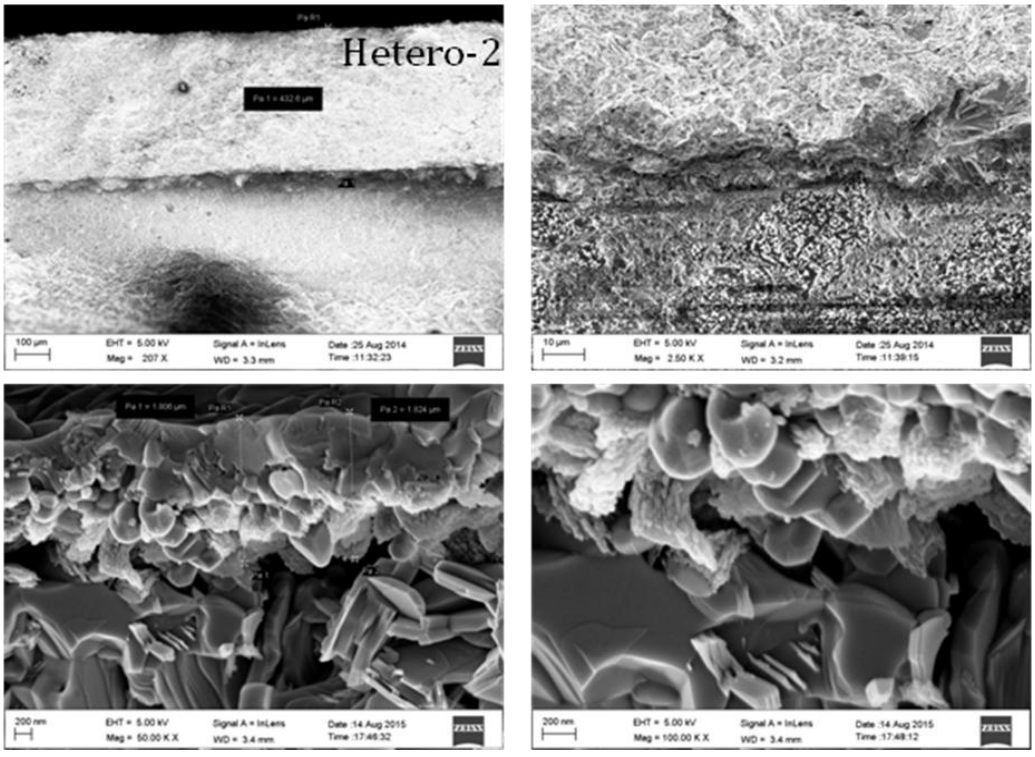

Figure 6.4 *FESEM images for Hetero-2 sample at different scales.*

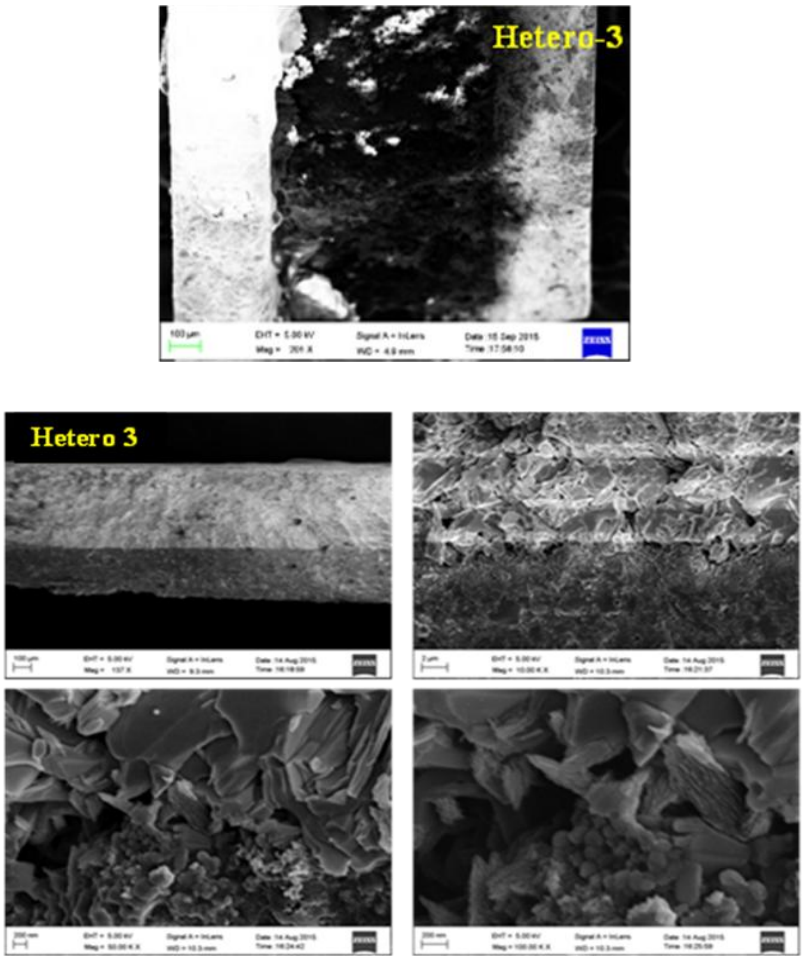

Figure 6.5 *FESEM images for Hetero-3 sample at different scales.*

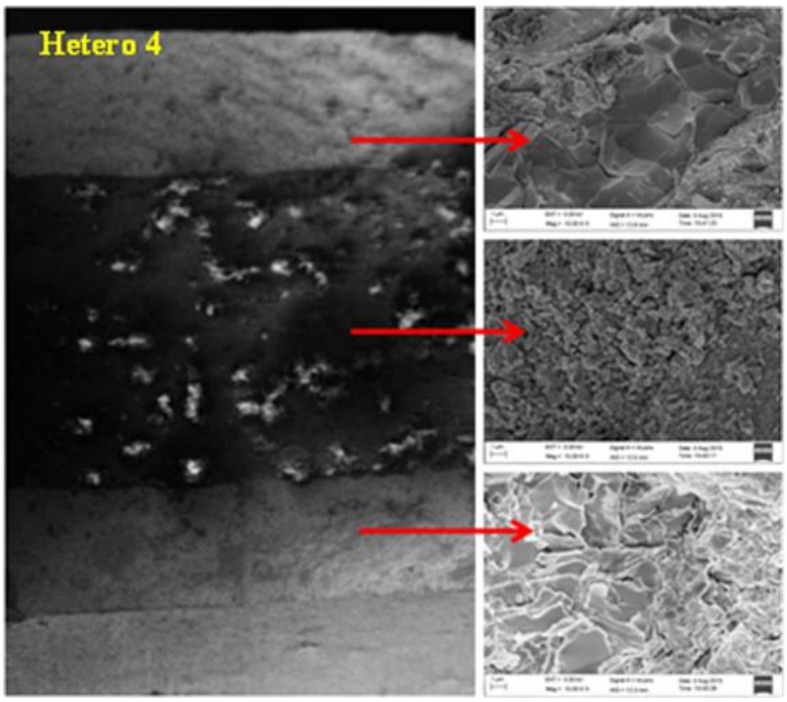

Figure 6.6 *FESEM images for Hetero-4 sample at different scales.*

Bi-2212 layers (top and bottom layers) and MgB_2 layer (middle) are observed in figure 6.6. Thickness of the tri-layer sample is ~1.1mm. The thickness of individual layers is 250µm+250µm for top and bottom layers of Bi-2212, and 600µm for MgB_2 layer. Surface morphology is shown with high magnification images (shown by arrows in figure 6.6). Well crystallized Bi-2212 grains are observed in top and bottom layers and MgB_2 grains in the middle layer. Bright colour masses on the surface of middle layer are MgO obtained from EDS analysis. A clear increment in grain connectivity is observed from Hetero-3 to Hetero-4 samples.

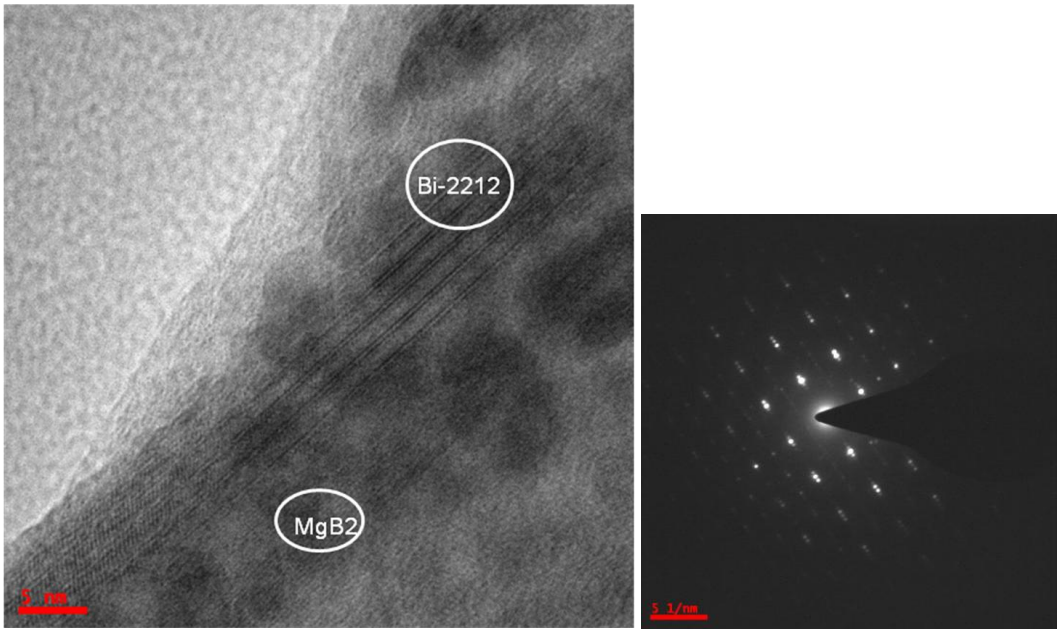

Figure 6.7 *TEM images for Hetero-1 sample.*

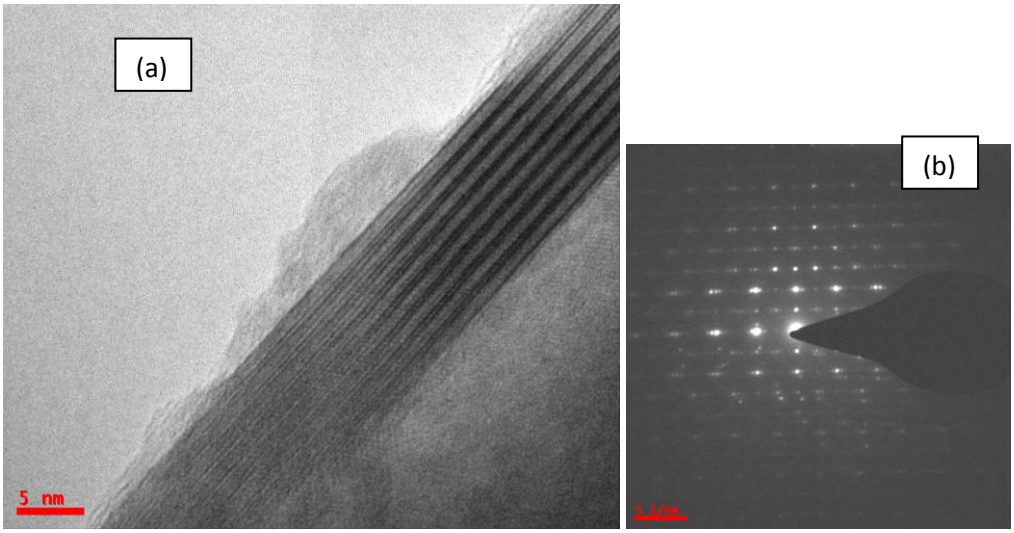

Figure 6.8 *TEM images for Hetero-2 sample.*

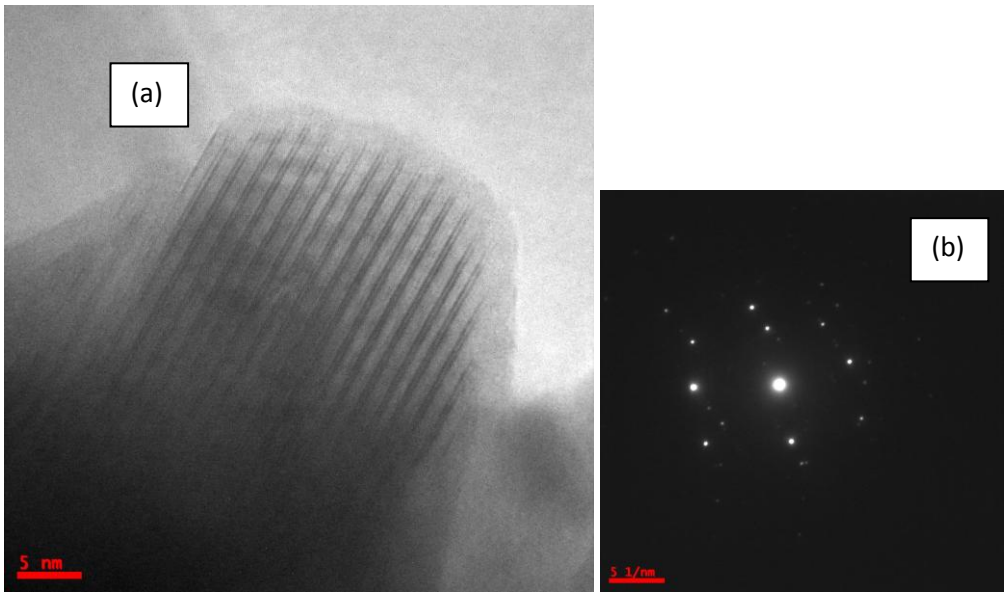

Figure 6.9 *TEM images for Hetero-3 sample.*

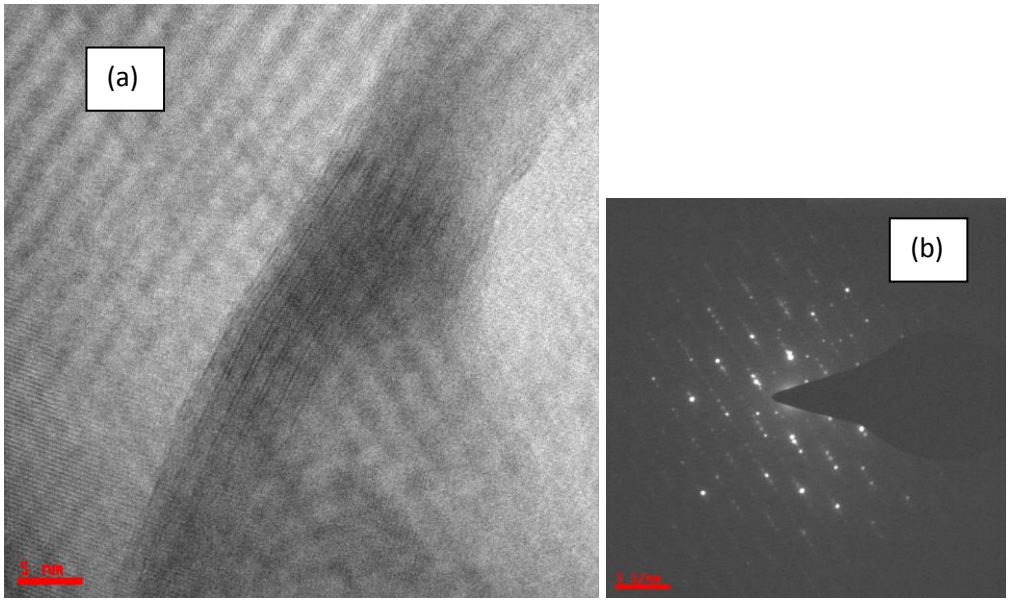

Figure 6.10 *TEM images for Hetero-4 sample.*

Specimens for TEM were prepared by doing smooth scratch at the cross section of the sample. TEM micrograph shows cross section of superlattices in which different layers can be clearly distinguished because of high atomic number contrast between the layers. Figures 6.7-6.10 show HRTEM images and diffraction patterns of the Hetero samples. HRTEM images of all samples show lattice planes corresponding to Bi-2212 and MgB_2, confirming the presence of both phases with clear grain boundaries. From the diffraction pattern of the samples one can see satellite spots along with major spots, which confirm the super lattice structure of the Hetero samples.

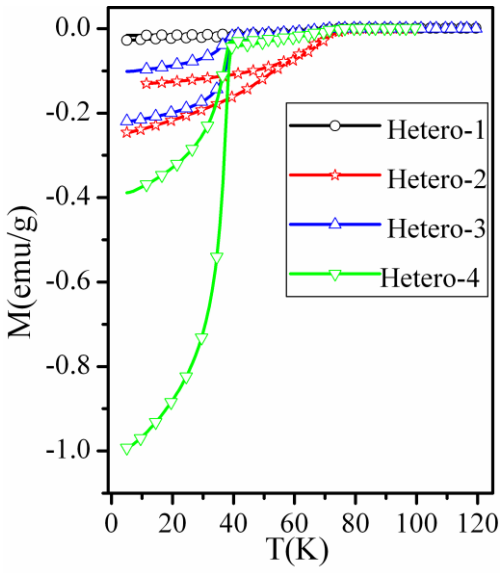

Figure 6.11 *Magnetization vs Temperature plots for the samples.*

The superconducting transition temperature of hetero structure samples was measured from the magnetization *vs* temperature data. Figure 6.11 shows the *d.c*. magnetization data of various samples both in zero field cooled (ZFC) and field cooled (FC) process. FC process was carried out under the applied dc magnetic field of 100Oe. All the samples show two transitions, one at 80K corresponding to Bi-2212 and another one at 39K corresponding to MgB_2. Superconducting volume fraction increased with decrease in MgB_2 layer thickness. Tri-layer samples show increase in superconducting volume fraction compared to bi-layer samples.

Magnetic hysteresis loops on the rectangular samples were measured at 10K, by applying field perpendicular to the sample surface. Hysteresis loops of the samples show asymmetry which is intrinsic property of Bi-2212 superconductor [8]. From this we can say that Bi-2212 dominates in the Hetero samples. Asymmetry is increased from bi-layer to tri-layer samples. The magnetic moment also increases considerably. Hysteresis loop width is directly proportional to the flux trapped in the superconductor. The same sample can show various magnetization loop shapes at different temperatures or up to different values of maximal magnetic field. The geometric shape, its structure and homogeneity of the sample influence the *M(H)* dependence. At temperatures higher than ~10K the high field *M(H)* dependence of high T_C superconductors have a pronounced asymmetry with respect to the M=0 axis, so the main parts of hysteretic loops fall in the second and fourth quadrants. This asymmetry grows with temperature [9-13]. The critical current density is calculated for the samples using magnetic hysteresis loops of rectangular slab type samples.

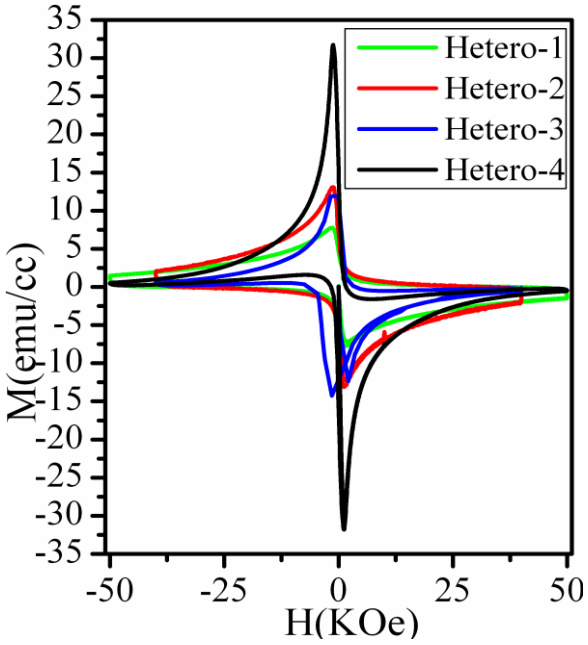

Figure 6.12 *Magnetization Hysteresis loops at 10K for various samples.*

From the hysteresis loops (figure 6.12) we observed the flux trapping at low fields and fast flux creeping at high fields. J_c was calculated according to Beans extended critical state model [14] using the following equation

$$J_c=20(\Delta M/d) \tag{6.1}$$

here, $d=b\,[1-(b/3a)]$, $a>b$, $\Delta M\ (M^{+}-M^{-})$ is the width of the *M-H* loop and *a*, *b* are sample dimensions.

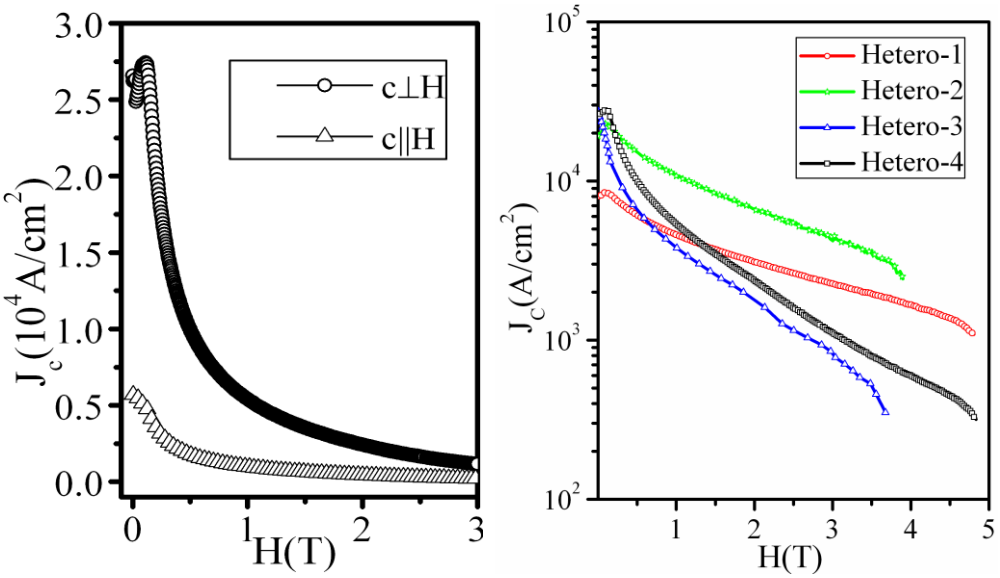

Figure 6.13 *(a) J_c anisotropy in Hetero-4 and (b) Critical current density variation with field in the samples.*

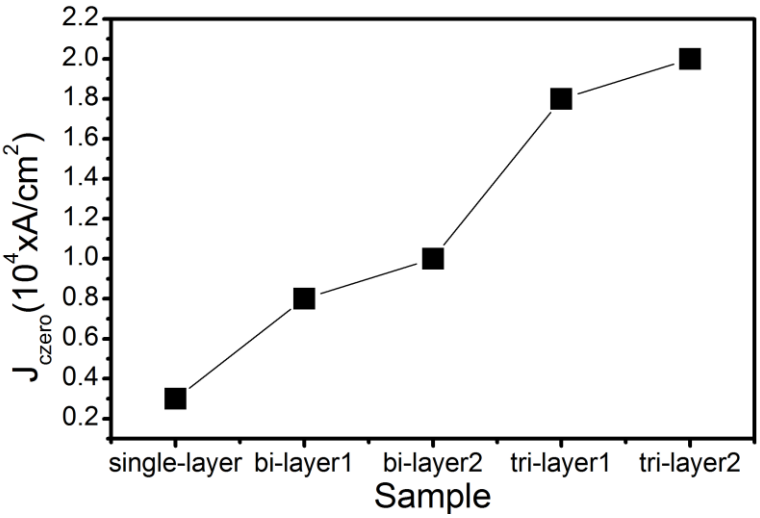

Figure 6.14 *J_c^{zero} variation of the samples.*

Field dependence of J_c at 10K for the Hetero samples is shown in figure 6.13. Anisotropy in critical current density is shown in Hetero-4 sample by plotting in-plane and out of plane J_c variation with field (figure 6.13*(a)*). Anisotropy in J_c is anticipated as the in-plane critical current density value J_c^{ab} should be at least 60% higher than the values along *c*-axis direction J_c^c. J_c anisotropy ratio for aligned MgB_2 crystallites at H=0 is 1.5 [15]. In the present (tri-layer) Hetero-4 sample J_c^c is higher than J_c^{ab}. The inverted J_c anisotropy ratio is 4.6 at H=0. High inverted anisotropy in J_c is due to enhancement of ab-plane properties due to multilayer growth process in tri-layer (Hetero-4) sample. Figure 6.13*(b)* shows J_c^c variation with field in all the samples. From this figure we can observe clearly that the self-field critical current density (J_c^{zero}) increases from bi-layer to tri layer, whereas at 3T, J_c is high in bi-layer sample than tri-layer sample. Fast decrease in J_c of tri-layer samples is observed when compared with bi-layer sample. From figure 6.14 it is clearly observed that the critical current density has increased in Hetero structured samples compared to bulk single layer of Bi-2212. There are two possibilities to explain this increment, one is proximity effect and another one is interfacial effects. But in the present samples, possibility of proximity transition is ruled out as there is no change in the T_c value of the two superconducting phases in Hetero samples. And the interfacial effects are dominated by bulk properties of the superconducting layers. Hence increase in J_c with increase in superconducting layers thickness is attributed to the increase in superconducting volume fraction. Fast decrease of critical current density in tri-layer samples is owing to different pinning mechanism and microstructure defects in these samples compared to bi-layer samples.

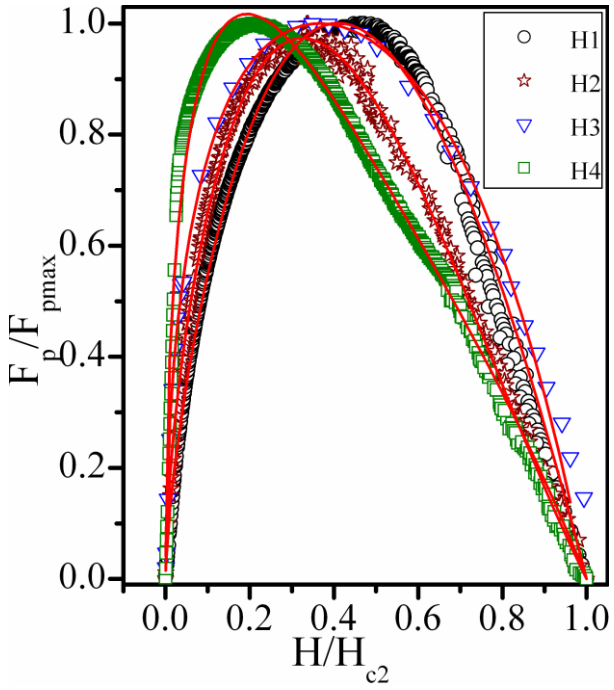

Figure 6.15 *Normalized pinning force vs reduced field for various samples.*

Pinning force per unit volume is calculated using the equation $F_p=\mu_0 H \times J_c$, where $\mu_0=4\pi x10^{-7} N/A^2$. Pinning force is increased in Hetero samples. Figure 6.15 shows the normalized pinning force response with reduced field ($h=H/H_{c2}$) at 10K for the samples. h_{max} varies from 0.5, 0.31, 0.29, 0.2 for Hetero-1 to Hetero-4 samples respectively. This suggests that the dominating pinning mechanism is different in each Hetero sample. In case of Hetero-1 sample pinning is due to mainly volume pinning centers, in Hetero-2 and Hetero-3 sample point pinning centers dominate over volume and surface pinning centers whereas in case of Hetero-4 sample pinning is mainly due to surface pinning centers. According to Dew Hughes predictions, grain, twin and Martensite boundaries, stacking faults, dislocations such as sub-grain, polygonized boundaries, plate like precipitates and the surface of the superconductor act as surface pins. Large precipitates and thick walled dislocation cell structures act as volume pinning centers and Nano size impurity phases act as point pinning centers [16]. This analysis was well supported by the Krammar fit to the data. Exact geometry of pinning centers was found from Kramer fit to the normalized pinning force response to the reduced field. According to Kramer theory [17] the relation between normalized pinning force and geometry of pinning centers is given by the following equation.

$$F(h)=F_p/F_{pmax}=Ah^p(1-h)^q \qquad (6.2)$$

here, h is reduced field defined as H/H_{c2}, p and q are shape parameters of pinning centers and A is constant. For point pinning p=1 and q=2, for surface pinning p=0.5 and q=2, and p=1, q=1 for volume pinning [17]. Both the surface pinning, point pinning fits and their combined fit also failed to explain the exact pinning geometry in the present samples. We succeeded in fitting the curve to the following equation which combine surface, point and volume pinning mechanism,

$$F(h)=A_s h^{0.5}(1-h)^2+B_p h(1-h)^2+C_v(h(1-h)) \quad (6.3)$$

This equation gave best fit for all samples. In all the samples, grain boundaries act as surface pinning centers, lattice defects and impurity phases act as point pinning and volume pinning centers. Dominating pinning mechanism is determined from the corresponding fitting constants (A_s, B_p, C_v for surface, point, volume pinning respectively) and the values are given in table 6.1.

Table 6.1 *Comparative table for the various properties of Hetero samples*

	Sample	MgB_2 layer Thickness (mm)	$J_{c(zero)}$ (A/cm^2)	$J_{c(3T)}$ (A/cm^2)	h_{max}	A_s	B_p	C_v
Single	Bi-2212		0.2×10^4	0.15×10^4	0.33	1.56	0.46	2.38
Bi-Layer	Hetero 1	0.5	0.8×10^4	0.2×10^4	0.5	0.91	0.66	2.91
	Hetero 2	0.4	1×10^5	0.6×10^4	0.3	1.50	1.71	1.51
Tri-Layer	Hetero 3	0.7	1.9×10^5	0.8×10^3	0.29	2.87	3.88	3.76
	Hetero 4	0.6	2×10^5	0.1×10^4	0.2	4.20	3.85	1.92

6.4 Chapter Summary

In summary, the Hetero structure of Bi-2212 and MgB_2 superconductors were synthesized and studied for their superconducting properties. X-ray diffraction pattern and dc magnetization studies confirm the presence of both superconducting phases in these Hetero structured samples. The *d.c* magnetization shows the superconducting transition at 80K and 39K for Bi-2212 and MgB_2 phases respectively. In case of tri layer sample critical current density is calculated from hysteresis loop of the sample both in-field and out of field configurations. Inverted anisotropy in J_c is due to enhancement of ab-plane properties

due to multilayer growth process. Morphology of the samples at the surface crossection shows well crystallized grains of superconducting phases in their respective layers. Critical current density increases in multilayer of Bi-2212 and MgB_2 superconductors due to increase in superconducting volume fraction. Instability of J_c at high fields is attributed to different pinning mechanism and microstructural variations in the samples. In Hetero-1 sample surface pinning due to grain boundaries is dominant pinning mechanism. In Hetero-2 and Hetero-3 samples, point pinning due to lattice defects and impurities is dominant pinning mechanism. Whereas in case of Hetero-4 sample, volume pinning due to impurity phases is the dominant pinning mechanism.

References

[1]. S. Lee, C. Tarantini, P. Gao, J. Jiang, J. D. Weiss, F. Kametani, C. M. Folkman, Y. Zhang, X. Q. Pan, E. E. Hellstrom, D. C. Larbalestier, and C. B. Eom, *Nature Materials*, **12**, 392-396 (2013).

[2]. Yasuji T. Suga, H. Kurosaki, S. B. Kim, T. Maeda, Y. Yamuda, I. Hirabayashi, Y. Iijima, K. Kakimoto, and T. Saitoh, *Physica C*, **378-381**, 971-974 (2002).

[3]. A. Kiessling, J. Hanisch, T. Thersleff, E. Reich, M. Weigand, R. Huhne, M. Sparing, B. Holzapfel, J. H. Durrell and L. Schultzisssling, *Supercond. Sci. Technol*., **24**, 055018 (2011).

[4]. J. N. Eckstein and I. Bozovic, *Annu. Rev. Mater. Sci*., **25**, 679-709 (1995).

[5]. Triscon J. M, Fischor O, Bruner O, Antognaza L, Kent A. D, Karkut M. G, *Phys. Rev. Lett*., **64**, 804, (1990).

[6]. C. Z. Antoine, S. Berry, M. Aurino, J. F. Jacquot, J. C. Villegier, G. Lamura, and A. Andreone, *IEEE Transactions on Applied Superconductivity*, **21**, No.3, 2601-2604, (2011).

[7]. E. Zacharias and R. Singh, *Physica C*, **247**, 221-230 (1995).

[8]. D. M. Gokhfeld, D. A. Balaev, M. I. Petrov, S. I. Popkov, K. A. Shaykhutdinov and V. V. Val'kov, *Journal of Applied Physics*, **109**, 033904 (2011).

[9]. D. X. Chen, R. B. Goldfab, R. W. Cross and A. Sanchez, *Physical Review B.,* **48,** 8, 6426-6429 (1993).

[10]. D. C. Larbalestier, L. D. Cooley, M. O. Rikel et al., *Nature,* **410**, 186-189 (2001).

[11]. C. Cheng and Y. Zhao, *Physica C*, **463-465,** 220-224 (2007).

[12]. V. G. Prokhorov et al., *Supercond. Sci. Technol*., **22,** 045027 (2009).

[13]. D. X. Chen, R. W. Cross and A. Sacnchez, *Physica C,* **33**, 7, 695-703 (1993).

[14]. A. M. Campbell and J. E. Evetts., *Adv. Phys*., **21**, 199 (1972).

[15]. O. F. de Lima, C. A. Cardoso, *Physica C*, **386**, 575-577 (2003).

[16]. D. Dew-Hughes, *Philosophical Magazine,* **30:2**, 293-305 (1974).

[17]. E. J. Kramer, *J. Appl. Phys*., **44,** No.3, 1360-1370 (1973).

SUMMARY AND CONCLUSIONS

The work on three different layered superconductors was carried out. The main conclusions of the thesis work are as follows.

1. Studies on $Bi_4O_4S_3$ layered superconductor

Bismuth Oxy Sulphide samples with T_c=4.4K were synthesized through solid state reaction method. The effect of excess Bi_2O_3 and Bi, S on the phase formation of the $Bi_4O_4S_3$ were studied. $Bi_4O_4S_3$ with 5% and 10% of excess Bi_2O_3 over the required quantity as per stoichiometric composition were prepared. The polycrystalline $Bi_4O_4S_3$ phase along with Bi and Bi_2S_3 impurity phases were identified from the X-ray diffraction pattern. The refined lattice parameters of tetragonal structured $Bi_4O_4S_3$ with space group I4/mmm are, a=3.9703A^0, and c=41.3984A^0. From XRD and TEM analysis of the samples concluded that no significant change is observed in crystal structure with excess Bi_2O_3. The Transmission Electron Microscopy (TEM) analysis illustrates that the $Bi_4O_4S_3$ samples are multiphase materials and clearly show layer structure of $Bi_4O_4S_3$ without having any stacking faults. Morphology of the samples observed through FESEM images clearly showed increase in grain size of the samples synthesized with excess Bi_2O_3. The excess Bi_2O_3 does not affect significantly the superconducting transition onset (T_c^{onset}) and zero resistivity temperature (T_c^{zero}). The excess Bi_2O_3 acted as flux for the $Bi_4O_4S_3$ phase formation and resulted in increase in the superconducting volume fraction, grain size and critical current density (J_c) compared to the stoichiometric sample. However, the sample with 5% of excess Bi_2O_3 exhibits highest grain size and J_c value of 4.7x10^3A/cm^2 among the samples. The J_c varied according to collective pinning model and pinning force follows scaling law of combination of Kramer surface and point pinning. In $Bi_4O_4S_3$, the grain boundaries and impurity phases acts as surface and point pinning centers respectively. The maximum value of reduced field increases from 0.22 to 0.28, which indicates the dominating pinning mechanism change from surface pinning to point pinning as the Bi_2O_3 content increases.

$Bi_4O_4S_3$ samples with 10% of excess Bi and S over stoichiometric composition were prepared through solid state reaction method. The XRD pattern projects $Bi_4O_4S_3$ phase formation along with Bi and Bi_2S_3 impurity phases. The EDS analysis predicts most of the

grains with Bi rich and S deficiency phase along with superconducting grains. The DSC thermograms also showed increase in impurity phase contribution in $Bi_4O_4S_3$ synthesized with excess Bi and S. Transport studies reveal that there is no impact of excess Bi and S, on the normal state properties of $Bi_4O_4S_3$. Low superconducting volume fraction is observed in $Bi_4O_4S_3$ samples synthesized with 10% excess Bi and S from both the transport and dc magnetization studies.

The effect of Ca doping at Bi site in $Bi_4O_4S_3$ superconductor was studied. $Bi_{4-x}Ca_xO_4S_3$ ($0<x<1$) samples were synthesized by solid state reaction method. The superconducting transition temperature T_c^{zero} increases with Ca doping of x=0.25. The sample with $x \geq 0.5$ exhibits metal to semiconductor transition at ~150K. These changes are ascribed to the disintegration of superconducting phase into other non-superconducting phases like Bi_2S_3. The XRD and TEM analysis of the samples concluded that Ca dopant is going into the interstitial positions of Bi_2S_3. The disintegration of superconducting phase with the increase in Ca doping, is observed clearly from FESEM images. The sample with x=0.25 shows increase in grain size and homogeneity and grain connectivity as well as increase in the impurity phases. In case of samples with $1 \leq x \geq 0.5$, superconducting $Bi_4O_4S_3$ grains were observed through TEM images. Disappearance of superconductivity in these samples is due to loss of grain connectivity and increase in the impurity phases.

2. The Composite system of Bi-2212 and MgB2 high T_c layered superconductors

The composite system of the glass ceramic Bi-2212 and MgB_2 superconductors in 1:2 and 2:1 weight ratios were synthesized. The d.c. magnetization studies showed superconducting transitions at two temperatures, one at 80K corresponding to Bi-2212 phase and the second transition at 39K corresponding to MgB_2 phase suggesting that the two superconducting phases were separated with clear boundaries. Critical current density and pinning force are increased in composite systems. Glass ceramic inclusions are observed in bulk MgB_2 through high resolution TEM images of the composite samples. Pinning mechanism in glass ceramic Bi-2212, powder ceramic Bi-2212 and MgB_2 is analyzed in detail. In case of Bi-2212 glass ceramic, normal core point pinning is more dominating, whereas in powder ceramic of Bi-2212, superconducting core volume pinning is more dominating. In MgB_2, pinning mechanism is well explained by considering both surface and point pinning centers. The pinning mechanism in composite samples is same as in its matrix phase. In 1:2 composite sample the normalized pinning force data is well

fitted with combination of Kramer surface and point pinning centers. Glass ceramic Bi-2212 Nano particles inclusions, in MgB_2 matrix, act as point pinning centers and grain boundaries act as surface pinning centers. In case of 2:1 composite sample Kramer fit of the normalized pinning force data confirmed the presence of surface, point and volume pinning centers. The core volume pinning due to low T_c phase (Bi-2201-observed from TEM), point pinning due to MgB_2 Nano inclusions in Bi-2212 matrix and surface pinning due to grain boundaries are observed in 2:1 composite sample. Reduced field maxima are observed at 0.15 for composite samples. Low value of h_{max} for this composite samples indicates the random orientation of grain boundaries and repulsive pinning force.

3. Hetero Structures of Bi-2212 and MgB_2 high T_c layered superconductors:

The Bi-2212 and MgB2 superconductors were arranged in the form of bulk multilayer using hydraulic pressure system at ambient conditions. Four samples (2-bilayer, 2-trilayer) were prepared with variation of the MgB_2 layer thickness. The X-ray diffraction pattern and dc magnetization studies confirms the presence of both superconducting phases in the hetero structured samples. Critical current density (J_c) is calculated from the hysteresis loop of the sample for both, in-plane field and out of plane field, configurations. Inverted anisotropy in J_c is observed due to enhancement of ab-plane properties because of multilayer growth process. Morphology of the samples at surface and interface of two superconducting layers showed well crystallized spherical grains corresponding to MgB_2 and platelet like structures corresponding to Bi-2212. The proximity effect and interfacial effects were dominated by bulk nature of the layers. The J_c has increased in hetero structured samples with increase in number of layers and also with decrease in MgB_2 layer thickness. The pinning mechanism of the samples is analysed using Kramer scaling method. The Normalized pinning force data of the samples was well fitted with combination of surface, point and volume pinning centers. Here, the grain boundaries act as surface pinning centers, lattice defects and impurity phases act as volume pinning centers. The Reduced field maxima (h_{max}) varied from 0.5 to 0.35 for bi-layer samples, indicates the dominating pinning mechanism changes from volume pinning to point pinning with decrease in MgB_2 layer thickness. In case of tri-layers samples h_{max} varied from 0.34 to 0.2 which suggests the dominating pinning mechanism shifts from point pinning to surface pinning with decrease in MgB_2 layer thickness.

The present work has provided an insight into the vortex pinning mechanisms in three different layered superconductors and their composites and hetro-structures. This study can pave the way in tuning the properties of these materials for applications.

4. Future Aspects

- To prepare multilayer thinfilms of Bi-2212 and MgB_2 superconductors.
- To study the interfacial effects and proximity effect between multilayer thinfilms of Bi-2212 and MgB_2 superconductors.
- To study the microwave sintering effects on MgB_2.

Publications

Journal Publications

[1] M. Padmavathi, and R. Singh, "*Effect of excess Bi_2O_3 on the Transport and Magnetic properties of Bismuth Oxy- Sulphide Superconductors*", *Journal of Superconductivity and Novel Magnetism*, ***28***, 1461-69, (2015).

[2] M. Padmavathi, and R. Singh, "*Effect of Density on the Electrical Properties of MgB_2 Superconductor*", *Indian journal of Cryogenics*, Vol. **40**, 2015".

[3] M. Padmavathi, and R. Singh, "*Structure and Properties of Ca doped Bismuth Oxy Sulphide Superconductor*", *Journal of Superconductivity and Novel Magnetism, **28**, 3255-3265, (2015).*

[4] Research Paper entitled "Structural and *Magnetization Studies on Composite System of Glass Ceramic Bi-2212 and MgB_2 Superconductors*". (To be communicated).

[5] Research Paper entitled "Structural and *Magnetization Studies on Hetero structures of Glass Ceramic Bi-2212 and MgB_2 Superconductors*". (To be communicated).

Conference proceedings

[6] M. Padmavathi, and R. Singh, "*Effect of Ca Doping on Superconducting Properties of $Bi_4O_4S_3$*" AIP Conf. Proc. 1665, 130024-1–130024-3, (2015).

[7] M. Padmavathi, and R. Singh, "Hetero structures of Bi-2212 and MgB_2 Superconductors", accepted for publication in *AIP Conf. Proc.* (2016).

[8] M. Padmavathi, and R. Singh, "Pinning mechanism in Bi-2212 and MgB_2 Superconductors", accepted for publication in *IOP conference series: Materials Science and Engineering* (2016).

[9] M. Padmavathi, and R. Singh, "Systematic studies on Hetero structures of Bi-4334 and MgB_2 Superconductors", accepted for publication in *IOP conference series: Materials Science and Engineering* (2016).

STUDIES ON SOME LAYER STRUCTURED SUPERCONDUCTORS: Bi4O4S3, Bi-2212 AND MgB2

ORIGINALITY REPORT

22%	12%	17%	%
SIMILARITY INDEX	INTERNET SOURCES	PUBLICATIONS	STUDENT PAPERS

PRIMARY SOURCES

1	dyuthi.cusat.ac.in Internet Source	2%
2	Ivan A. Parinov. "Superconductors and Superconductivity: General Issues", Microstructure and Properties of High-Temperature Superconductors, 2007 Publication	1%
3	Advances in Superconductivity X, 1998. Publication	1%
4	www.qucosa.de Internet Source	1%
5	David B. Williams. "Scattering and Diffraction", Transmission Electron Microscopy, 2009 Publication	1%
6	K Vinod. "Prospects for MgB_2 superconductors for magnet application", Superconductor Science and Technology, 01/01/2007 Publication	1%

7	www.arscryo.com Internet Source	1%
8	www.substech.com Internet Source	1%
9	Advances in Superconductivity V, 1993. Publication	1%
10	Transmission Electron Microscopy, 1996. Publication	1%
11	Undergraduate Lecture Notes in Physics, 2016. Publication	1%
12	David B. Williams. "The Instrument", Transmission Electron Microscopy, 2009 Publication	1%
13	mcff.mtu.edu Internet Source	1%
14	Zacharias, E.. "Crystallization and resistivity studies on Bi"4Sr"3Ca"3Cu"yO"x glasses", Physica C: Superconductivity and its applications, 19950601 Publication	1%
15	www.esrf.eu Internet Source	<1%
16	D. Dew-Hughes. "Flux pinning mechanisms in type II superconductors", Philosophical Magazine, 8/1/1974 Publication	<1%

17	Advances in Superconductivity XI, 1999. Publication	<1%
18	www.vcbio.science.ru.nl Internet Source	<1%
19	Advances in Superconductivity VI, 1994. Publication	<1%
20	electronmicroscopy.org Internet Source	<1%
21	valmap.dfis.ull.es Internet Source	<1%
22	Durrani, Shahid-Khan, Muhammad-Ashraf Hussain, Khalid Saeed, Syed-Zahid Hussain, Muhammad Arif, and Ather Saee. "Synthesis and Sintering Studies of Magnesium Aluminum Silicate Glass Ceramic", Sintering of Ceramics - New Emerging Techniques, 2012. Publication	<1%
23	etheses.saurashtrauniversity.edu Internet Source	<1%
24	Larkin, A. I., and Yu. N. Ovchinnikov. "Pinning in Type II Superconductors", World Scientific Series in 20th Century Physics, 1996. Publication	<1%
25	Hari Babu, N.. "Effect of a systematic variation of Nd"4Ba"2Cu"2O"1"0 content on the magnetic properties of melt processed	<1%